Nonlinear Dynamics in $\mathscr{PT}$ - Symmetric Optical Systems

by

Jyoti Prasad Deka

A thesis submitted
in Partial Fulfillment of the Requirements
for the Degree of
DOCTOR OF PHILOSOPHY.

Department of Physics
Indian Institute of Technology Guwahati
Guwahati 781039, India.

July 2019

Nonlinear Dynamics in $\mathscr{PT}$ - Symmetric Optical Systems

by

Jyoti Prasad Deka
Roll No. 146121031

A thesis submitted
in Partial Fulfillment of the Requirements
for the Degree of

DOCTOR OF PHILOSOPHY.

Supervisor
Prof. Amarendra Kumar Sarma

Department of Physics
Indian Institute of Technology Guwahati
Guwahati 781039, India.

July 2019

DECLARATION

The work in this thesis entitled "*Nonlinear Dynamics in $\mathcal{PT}$-Symmetric Optical Systems*" has been carried out by me under the supervision of Prof. Amarendra K. Sarma, Department of Physics, Indian Institute of Technology Guwahati. No part of this thesis has been submitted elsewhere for award of any other degree or qualification. The research works have been carried out in the period from January, 2015 to December, 2018.

In keeping with general practice of reporting scientific observations, due acknowledgments have been made wherever the work described is based on the findings of other investigations.

Jyoti Prasad Deka,
Roll no. 146121031,
Department of Physics, IIT Guwahati,
Guwahati-781039, Assam, India.
DATE: .....

CERTIFICATE

It is certified that the work contained in the thesis entitled "*Nonlinear Dynamics in $\mathcal{PT}$-Symmetric Optical Systems*" by Mr. Jyoti Prasad Deka, a student of the Department of Physics, IIT Guwahati was carried out under my supervision and has not been submitted elsewhere for award of any degree.

Prof. Amarendra Kumar Sarma,
Department of Physics, IIT Guwahati,
Guwahati-781039, Assam, India.
DATE: .....

To my Family,

To the Inseparable Four,

and

To Sha*N*traa.

ACKNOWLEDGMENTS

Firstly, I would like to express my sincere gratitude towards my Ph.D. advisor, Prof. Amarendra Kumar Sarma for his consistent support, guidance, patience and motivation during my Ph.D. years. His deep understanding of the field helped me understand the field better and his faith on me always inspired me to work hard and to do better. In one instance, I attended his Electrodynamics lectures and the ease with which he explained the '*Kramers-Kronig Relations*' was something I still remember today. And another time, I was having difficulty in the mathematical modelling of one of my problems and I visited him in his office and asked if he has Pochi Yeh's '*Optical Waves in Layered Media*' and he lent me his copy and the difficulty was resolved instantly. And once again, I would like to thank him for all the guidance he offered me in my PhD years and someday I hope I can do the same to my students.

I would like to thank my doctoral committee members Prof. Girish S. Setlur, Dr. Sayon Chakrabarti and Prof. Rakhesh Singh Kshetrimayum for their encouragement and insightful comments which helped me to improve my presentation skills and also my understanding of my work. I would also like to express my sincere gratitude to Girish Sir, for I had enjoyed answering his questions in my PhD admission interview and comprehensive exam and his questions have always motivated me to enjoy the beauty of physics from a much more enriching and interesting perspective.

My sincere gratitude goes to the current and former Heads of the Department of Physics, Prof. Subhradip Ghosh, Prof. P. Poulose and Prof. Saurabh Basu for providing me with all the facilities for my research and also to all the faculty members of the department and the non-teaching staff. I would like to thank Prof. Subhradip Ghosh for his Statistical Mechanics lectures in my PhD coursework. His lectures helped me immensely in improving my presentation skills and his numerous assignments helped me inculcate the belief that problems are not something to be feared, but rather enjoyed and relished.

I would like to thank my PhD group-mates Samit, Bijita, Koushik, Monika, Subhadeep and Dipti for all the fruitful discussions we have had. Special thanks goes to Samit for his assistance in the formative years of my PhD and to Dipti for the interesting cultural exchange of the Assamese and Bengali culture that we have had several times in the evenings. I would also like to thank my PhD batchmates Sunayana and Monika for all the moments of enjoyment, fun and intermittent serious discussions that we have had. And special mention must be made of my friend Joy Prakash Das, who shares the same initials with me and with whom the long walks in the academic complex of IIT Guwahati has always been filled with meaningful discussions about philosophy and of my batchmates Sasmita Behera, S. Jagan Mohan Rao and Jhulan Garai, with whom I had a great and memorable time during the PhD coursework months.

I would like to thank the most special friends of my life in the University of Delhi - 'Inseparable Four', Aparna Bisht, Abhishek Santra, Ishan Bhatkoti and Kshitij Saigal. From the group 'Inseparable Four', I would like to thank my best friend from college Mahati Srinivasan, for she gave me the confidence that a subject of my interest given to me and I can create magic teaching it to my students. My heartfelt gratitude and thanks goes to my other best friend Sheetal Dewan who once told me that I give her a lot of inspiration to take up academics as a career and through this thesis, I want to return back the same to her and she has always been a guiding star that showed me the way when life became gloomy and dark. To Aparna Bisht, who gave me the inspiration that I could indeed guide people to do well in their life and as such, she is my favourite student since 2008. To Adwitiya Singh with whom I spent many memorable moments during my college years. To Kshitij Saigal who introduced me to the delicious Nawabi cuisine of Lucknow, the taste of which still lingers in my tongue. To Ishan Bhatkoti, for all those nights watch animation movies late into the night. And finally to Abhishek Santra, who introduced me to the Bengali culture, all those late night discussions that never ended in anything meaningful and the poem of my life that has not yet been completed. Those were the days I lived in, the memories of which could never be erased.

I would like to thank the oldest friends of my life Dristirupa Patgiri and Jubaraj Jnanbikash Baruah, with whom I shared a friendship of more than twenty five years. They gave me all the support to maintain a balanced life between work and leisure life and without whom I never could have reached the moment I am in today. And to Tridib, who was my friend since my 11th standard and with whom I spent majority of my time in the first two years of my life discussing the visual aesthetics of the designs that we

see in this world.

I would like to express my humble gratitude towards my father Prof. Rudra Kanta Deka, my mother Mrs. Mina Deka and my brother Mridupawan Deka. My father inculcated in me the belief that sometimes in life, we have to burn in the fires of hell to enjoy the fruits of heaven and this belief helped me pass through the various moments of pain and anguish in my PhD life with flying colors. He also once told me "Help and guide others for your own satisfaction and not because you want something from them." and this is something that has always guided me in my life. My mother showered me with love, care and patience and these, I feel, played a very important role in helping me steer through the last five years. And lastly, a special mention of my brother, with whom discussions of gaming and technology never ended and these are something that will continue no matter how old I become.

ABSTRACT

Carl Bender and Boettcher in 1998, showed that Hamiltonians which are invariant under the joint operation of the parity and the time-reversal operator could yield a real eigenspectra, which marked a new milestone in the foundational aspects of quantum mechanics. Not so long after, D. N. Christodoulides and his group put forward the proposition that optics could facilitate the experimental realizations of such systems. In 2010, Rüter *et al.* reported the first experimental observation of $\mathscr{PT}$-symmetry in optics. And since then, numerous novel phenomena such as unidirectional invisibility, route to chaos in optomechanical cavities, rogue wave dynamics, wireless power transfer, stable dark solitons in dual-core waveguides, modulation instability in nonlinear complex $\mathscr{PT}$-symmetric periodic structures, etc. have been reported. In this thesis, we report on the features that arise in a $\mathscr{PT}$-symmetric optical system when it is subjected to analysis from a dynamical perspective. We analyzed the nonlinear $\mathscr{PT}$-symmetric dimer using the linearization Jacobian approach and found that it exhibits sensitiveness to initial conditions. Also, we have studied two configurations of the Ikeda map and found that judiciously choosing the system parameters could enable the control of chaotic dynamics as well as the generation of chaotic spiking in the system. Furthermore, we have studied the transmission of normally incident electromagnetic waves on a multilayered structure and we found that highly amplified in the infrared spectrum is achievable via engineered S-matrix singularities. And in the last part of the thesis, we have discussed the $\mathscr{PT}$-symmetric Liénard systems and from our thorough analysis of the stationary states, we discovered the emergence of blow-dynamics, oscillation death and the quasiperiodic route to chaos in our model.

List of Publications and Conferences Attended

Journal Publications

1. **Jyoti Prasad Deka** and Amarendra K. Sarma, "Perturbative dynamics of stationary states in nonlinear parity-time symmetric coupler", Communications in Nonlinear Science and Numerical Simulation 57, 26 (2018).

2. **Jyoti Prasad Deka**, Samit Kumar Gupta and Amarendra K. Sarma, "Controllable chaotic dynamics in a nonlinear fiber ring resonator with balanced gain and loss", Nonlinear Dynamics 87, 1121, (2017).

3. **Jyoti Prasad Deka** and Amarendra K. Sarma, "Chaotic Dynamics and Optical Power Saturation in Parity-Time ($\mathscr{PT}$) Symmetric Double Ring Resonator", Nonlinear Dynamics, DOI: 10.1007/s11071-019-04806-z (2019).

4. **Jyoti Prasad Deka** and Amarendra K. Sarma, "Highly Amplified Light Transmission in Parity-Time Symmetric Multilayered Structure", Applied Optics 57, 1119 (2018).

5. Samit Kumar Gupta, **Jyoti Prasad Deka** and Amarendra K. Sarma, "Nonlinear Parity-Time ($\mathscr{PT}$) symmetric closed-form optical quadrimer waveguides: Attractor perspective", European Physical Journal D 69, 199 (2015).

6. **Jyoti Prasad Deka**, Arjunan Govindarajan, Manas Kulkarni and Amarendra K. Sarma, "Multifaceted Nonlinear Dynamics in $\mathscr{PT}$-Symmetric Liénard Oscillators" (under review in *Chaos*).

Conferences/Schools attended

1. International Conference on Complex Dynamical Systems and Applications 2017, 4th-6th December, IIT Guwahati (**Poster Presentation**).
2. Conference on Nonlinear Systems and Dynamics 2018, 11th-14th October, Jawaharlal Nehru University, Delhi, India (**Poster Presentation**).
3. Research Conclave 2017, IIT Guwahati (**Poster Presentation**).
4. 'Feel the Light – on Optics Outreach' organized by the SPIE IIT Guwahati Student Chapter at the Dept. of Physics, Cotton College, Guwahati (**Participation**).
5. Annual Physics Meet 2017, Dept. of Physics, IIT Guwahati (**Talk Presentation**).
6. South Asian Workshop on Optics and Photonics, 'SAWOP-2015', 17–18 November, 2015, IIT Guwahati, India (**Participation**).

LIST OF FIGURES

- **Figure 4.4:** (a) Bifurcation diagram of P_{res} and (b) λ_{max} vs. γ for $E_{in} = 2.5$.

- **Figure 4.5:** Period doubling point vs. E_{in}.

- **Figure 4.6:** Resonance profile for $E_{in} = 3.0$ and $\gamma = 0.92$. The parameters chosen are: $n_2 = 2.6 * 10^{-20} m^2 W^{-1}$, $A_{eff} = 10^{-14} m^2$ and $L = 0.5m$.

- **Figure 4.7:** Temporal evolution of the resonator optical power for $E_{in} = 2.5$ and $\gamma = 1.19$.

- **Figure 4.8:** Schematic diagram of the double-ring resonator. The black color block represents the 50:50 passive directional couplers (DC) and the brown color region represents the optical fibers. The lossy resonator is colored blue, while the amplifying resonator is colored red. E_in and $E^{'}_{in}$ are the input field amplitudes, and E_{out} and $E^{'}_{out}$ are the output field amplitudes. $E^{'}_{1}$ and $E^{'}_{4}$ are the output field amplitudes of coupler region DC1 and DC3, respectively. They are transferred via the resonators to the coupler region DC2 as E_1 and E_4. Similarly, E_2 and E_3 are the output field amplitudes of coupler region DC2. They are transferred, via the resonators, to the coupler region DC1 and DC3 as $E^{'}_{2}$ and $E^{'}_{3}$.

- **Figure 4.9:** Temporal evolution of optical power in both resonators. The parameters chosen are (a) $\gamma = 0.85$ (Below $\mathscr{PT}$ Threshold) (b) (a) $\gamma = 0.8814$ (At $\mathscr{PT}$ Threshold) (c) $\gamma = 1$ (Above $\mathscr{PT}$ Threshold). The input field amplitudes are $E_{in} = 1$ and $E^{'}_{in} = 1$ in both cases.

- **Figure 4.10:** Radius of the Hypersphere R vs. Gain/Loss Coefficient γ.

- **Figure 4.11:** Parameter Basin for Period-1 Cycle when (a) $\beta = 0$ (Linear Regime) (b) $\beta = 0.01$ (Weakly Nonlinear) (c) $\beta = 1$ (Strongly Nonlinear). $E^{'}_{in} = 1$ for all cases. The blue-colored region is the convergent region, i.e. the region where optical power saturation occurs. The red-colored region is the non-convergent region, signifying the presence of periodic as well as chaotic oscillations. And the black-colored region is the divergent region, and in this region, the optical power in both resonators diverges to infinity.

- **Figure 4.12:** (a) Bifurcation Diagram and (b) Largest Lyapunov Exponent (λ_{max}) vs. Gain/Loss Coefficient (γ). The other parameters are $E_{in} = 1$, $E^{'}_{in} = 1$ and $\beta = 1$

- **Figure 6.2:** Temporal evolution of the two oscillators for $\gamma = 0.4$. Other parameters: $\delta = 1$, $\omega_0^2 = 0.25$, $\kappa = 0.5$, $\eta = 0.1$ and $\beta = 1$.

- **Figure 6.3:** Temporal evolution of the gain oscillator for $\gamma = 0.4$. Other parameters: $\delta = 1$, $\omega_0^2 = 0.25$, $\kappa = 0.5$, $\eta = 0.1$ and $\beta = 1$.

- **Figure 6.4:** Temporal evolution of the gain oscillator for (a) $\psi = 10^{-3}$, (b) $\psi = 10^{-5}$, and (c) $\psi = 10^{-7}$. Other oscillator parameters: $\gamma = 0.4$, $\delta = 1$, $\omega_0^2 = 0.25$, $\kappa = 0.5$, $\eta = 0.1$ and $\beta = 1$. Drive parameters: $A_0 = 0.0001$ and $\omega = 2\pi/500$.

- **Figure 6.5:** Real components of the Jacobian eigenvalues of the $\mathscr{PT}$-Symmetric Liénard oscillator for (a) $\omega_0^2 = 0.25$, (b) $\omega_0^2 = 0.5$ and (c) $\omega_0^2 = 0.75$. Other parameters: $\delta = 2$, $\kappa = 0.5$, $\eta = 0.1$ and $\beta = 1$.

- **Figure 6.6:** Phase plane trajectory of the gain oscillator for (a) $\omega_0^2 = 0.75$, (b) $\omega_0^2 = 0.5$ and (c) $\omega_0^2 = 0.25$. Other parameters: $\delta = 2$ and $\gamma = 0.1$, $\gamma = 0.1$, $\delta = 2$, $\kappa = 0.5$, $\eta = 0.1$ and $\beta = 1$.

- **Figure 6.7:** Power spectra of the gain oscillator for (a) $\omega_0^2 = 0.75$, (b) $\omega_0^2 = 0.5$ and (c) $\omega_0^2 = 0.25$. $\delta = 2$ and $\gamma = 0.1$. Other parameters: $\gamma = 0.1$, $\delta = 2$, $\kappa = 0.5$, $\eta = 0.1$ and $\beta = 1$.

- **Figure 6.8:** Schematic representation of the electronic circuit. Here, **L**, **C** and **R** are the inductor, capacitor and the resistor respectively. $\mathbf{R}'$ is the non-ohmic resistor and **M** is the current multiplier.

TABLE OF CONTENTS

CHAPTER 1

INTRODUCTION

"Life is never boring or stagnant when one studies nonlinear dynamical systems that are constantly changing, evolving and reinventing themselves."

- Rajarshi Roy, Perspective in Nonlinear Dynamics 2016.

1.1 Introduction

Carl M. Bender and his graduate student Stefan Boettcher's path-breaking discovery of non-hermitian Hamiltonians with real eigen spectra marked a major milestone in the foundational studies of quantum mechanics towards the end of the 20th century [1]. Hermiticity of Hamiltonians is a concept in quantum mechanics that could never be disregarded if one is studying real physical systems. And this is because only such Hamiltonians could yield a real eigen spectra and as such, they deal with real physical observables. This very notion was challenged by the findings of Bender and Boettcher. They discovered that Hamiltonians that are invariant under the joint operation of the parity and the time-reversal operator could yield a real eigen spectra as well. In mathematical language, it could be said that such Hamiltonians commute with the $\mathscr{PT}$-operator ($[H, \mathscr{PT}] = 0$).

Parity ($\mathscr{P}$) and Time-reversal ($\mathscr{P}$) are two fundamental symmetries in theoretical physics. In quantum physics, they are represented as the transformation of the two

quantum mechanical operators, the position operator $\hat{x}$ and the momentum operator $\hat{p}$. The parity operator is a linear operator and it is defined as $\hat{x} \to -\hat{x}$ and $\hat{p} \to -\hat{p}$ and the time-reversal operator is an antilinear operator and it is defined as $\hat{x} \to -\hat{x}$, $\hat{p} \to -\hat{p}$ and $i \to -i$. In their seminal work [1], Bender and Boettcher considered the Hamiltonian given below.

$$H = p^2 + m^2x^2 - (ix)^N \tag{1.1}$$

They discovered that the eigen spectrum of H exhibits three distinct forms of behavior as a function of N and mass m^2. For $N \geq 2$, the spectrum is infinite, discrete and entirely real and positive. At the lower bound, i.e. at $N = 2$ lies the quantum harmonic oscillator. One of the major highlight of this work was the region $1 < N < 2$. In this region, the spectrum consists of a finite number of real eigenvalues and an infinite number of complex conjugate pairs of eigenvalues and $\mathscr{PT}$-symmetry is said to be spontaneously broken. The phase transition from a real and positive to complex eigen spectra occurs at $N = 2$, which is termed as the $\mathscr{PT}$ threshold. And the regime where the eigenvalues are entirely real and positive is termed as the unbroken $\mathscr{PT}$ regime and that where the eigenvalues are complex is termed as the broken $\mathscr{PT}$ regime. We would now explore $\mathscr{PT}$-symmetry in the time dependent Schrödinger equation given below.

$$i\hbar\frac{\partial\psi(x,t)}{\partial t} = H\psi(x,t) \tag{1.2}$$

where $H = -\hbar^2\nabla^2/2m + V(x)$ is the Hamiltonian and $V(x)$ is the potential function of this system. Now consider a case where $V(x)$ is an imaginary function, i.e. $V(x)$ has a real component $V_R(x)$ and an imaginary component $V_I(x)$. On operating the $\mathscr{PT}$-operator on this potential function, $V(x)$ would transform as $V_R(x) \to V_R^*(-x)$ and $V_I(x) \to V_I^*(-x)$. Now, if the $V_R(x)$ is an even function in x and $V_I(x)$ is an odd function in x, then $V(x)$ would remain invariant, i.e. the Hamiltonian would then be $\mathscr{PT}$-symmetric.

In the years that followed, $\mathscr{PT}$-symmetry had been investigated in quantum mechanics [2-5], quantum field theory [6-8], non-Hermitian Anderson models [9], open quantum systems [10], etc. But these were all mathematical models and till then, there was no experimental observation of $\mathscr{PT}$-symmetry. It was not until the proposition by Ramy El-Ganainy *et al.* that optical systems could facilitate the experimental realization of $\mathscr{PT}$-symmetry that such endeavors were seemed possible. Ramy El-Ganainy *et al.* proposed that coupled optical waveguide configuration with balanced gain and loss profile could facilitate the experimental realization of $\mathscr{PT}$-symmetry in optical systems [11]. Such a proposition was conceivable due to the shared isomorphism between the paraxial

equation of diffraction and the time dependent Schrödinger equation. The refractive index potential $n(\vec{r})$ in the former and the potential function $V(x)$ in the latter serve as the connection for this shared isomorphism. In addition to this, the refractive index potential must satisfy the condition $n(\vec{r}) = n^*(-\vec{r})$. This means that the real part of $n(\vec{r})$ must be an even function of $\vec{r}$ while the imaginary part an odd function of $\vec{r}$. Not so long after, Rüter *et al.* demonstrated the first experimental realization of $\mathscr{PT}$-symmetry in optical systems [12]. Rüter *et al.* studied a coupled optical waveguide configuration on $LiNbO_3$ substrate. One of the channel was optically pumped to provide gain and the other channel exhibits an equal amount of loss. And the mathematical model for the configuration (also known as the $\mathscr{PT}$-symmetric Dimer) could be expressed below.

$$i\frac{d}{dz}\begin{pmatrix}\psi_1\\ \psi_2\end{pmatrix} = \begin{pmatrix}i\gamma & C\\ C & -i\gamma\end{pmatrix}\begin{pmatrix}\psi_1\\ \psi_2\end{pmatrix} \tag{1.3}$$

where γ is the gain/loss coefficient and C is the coupling coefficient. The Hamiltonian of this system is $H_{\mathscr{PT}} = \begin{pmatrix}i\gamma & C\\ C & -i\gamma\end{pmatrix}$ and it could be easily seen that this Hamiltonian satisfies the criteria $[H_{\mathscr{PT}}, \mathscr{PT}] = 0$, where $\mathscr{P} = \sigma_x$ (x-Pauli matrix) is the parity operator and $\mathscr{T} = *$ (complex conjugation) is the time-reversal operator. In such a $\mathscr{PT}$-symmetric optical waveguide configuration, the $\mathscr{PT}$ phase transition is characterized by a transition from periodically evolving optical power to exponential growth and decay of optical power in the two waveguides. Since then, $\mathscr{PT}$-symmetry has been studied extensively in both theoretical as well as experimental domains. To name a few, some of them are unidirectional invisibility in periodic media [13], wireless power transfer [14], plasmonics [15-16], multilayered structures [17-18], optical oligomers [19-27], solitons [28-37], optomechanical systems [38-39], active LRC circuits [40] and so on.

We would now like to discuss the three formalism that has been used to investigate $\mathscr{PT}$-symmetric systems. They are the Hamiltonian, the Transfer Matrix and the Harmonic Oscillator approach. In the next sub-sections, we will discuss these three approaches in details.

1.2 Hamiltonian Approach

As we have discussed previously that the Hamiltonian for the $\mathscr{PT}$-symmetric Dimer is given by $H_{\mathscr{PT}} = \begin{pmatrix}i\gamma & C\\ C & -i\gamma\end{pmatrix}$, the eigen values of this Hamiltonian are $\lambda_H = \pm\sqrt{C^2 - \gamma^2}$. It

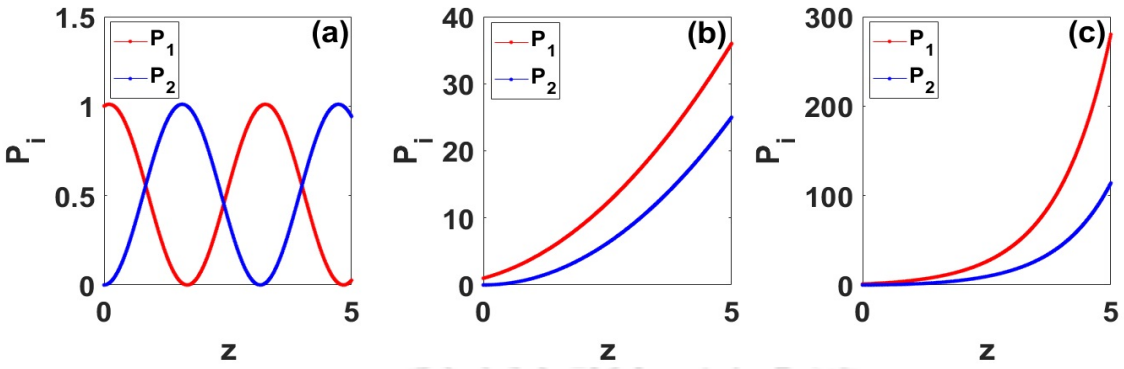

Figure 1.1: Spatial Evolution of Optical Power of the two waveguides for (a) $\gamma = 0.1$ (unbroken $\mathscr{PT}$ regime) (b) $\gamma = 1$ (at the $\mathscr{PT}$ threshold) and (c) $\gamma = 1.1$ (broken $\mathscr{PT}$ regime).

could be easily seen that the eigenvalues are purely imaginary for $\gamma > C$ and purely real for $\gamma < C$. The real as well as the imaginary component of the two eigenvalues coalesce at the $\mathscr{PT}$ threshold (or the Exceptional Point). For the $\mathscr{PT}$-symmetric dimer, the Hamiltonian has the $\mathscr{PT}$ threshold at $\gamma = C$. Below we would show the spatial evolution of optical power in the two waveguides in the unbroken and the broken $\mathscr{PT}$ regime as well as at the $\mathscr{PT}$ threshold. We have considered the coupling constant $C = 1$. From the spatial evolution of optical power of the two waveguides, it could be easily seen that the growth rate of optical power in the broken $\mathscr{PT}$ regime and at the $\mathscr{PT}$ threshold is exponential (Fig. 1.1(b) and 1.1(c)), whereas in the unbroken $\mathscr{PT}$ regime, optical power of the two waveguides oscillate out of phase with some phase lag. The reason for this could be found in the analysis of the supermodes of the system. In the unbroken $\mathscr{PT}$ regime, the supermodes are $|1\rangle = \begin{pmatrix} e^{i\theta/2} \\ e^{-i\theta/2} \end{pmatrix}$ and $|2\rangle = \begin{pmatrix} ie^{i\theta/2} \\ -ie^{-i\theta/2} \end{pmatrix}$, where $\theta = sin^{-1}(\gamma/C)$. From the supermodes, it could be seen that neither of them experience amplification or attenuation as it propagates. On the other hand, in the broken $\mathscr{PT}$ regime, the supermodes are $|1\rangle = \begin{pmatrix} e^{-\theta/2} \\ -ie^{\theta/2} \end{pmatrix}$ and $|2\rangle = \begin{pmatrix} e^{\theta/2} \\ -ie^{-\theta/2} \end{pmatrix}$, where $\theta = cosh^{-1}(\gamma/C)$. On operating the $\mathscr{PT}$-operator, it could be seen that these eigenvectors are no longer $\mathscr{PT}$-invariant and hence, not eigenfunctions of the $\mathscr{PT}$-operator. Moreover, the supermodes could be seen to undergo amplification as well as attenuation. It could also be seen that the supermodes coalesce at the $\mathscr{PT}$ threshold, i.e. $\gamma = C$. Hence, in the unbroken $\mathscr{PT}$ regime, we have oscillatory spatial evolution of optical power in the two channels and exponential growth in the broken $\mathscr{PT}$ regime.

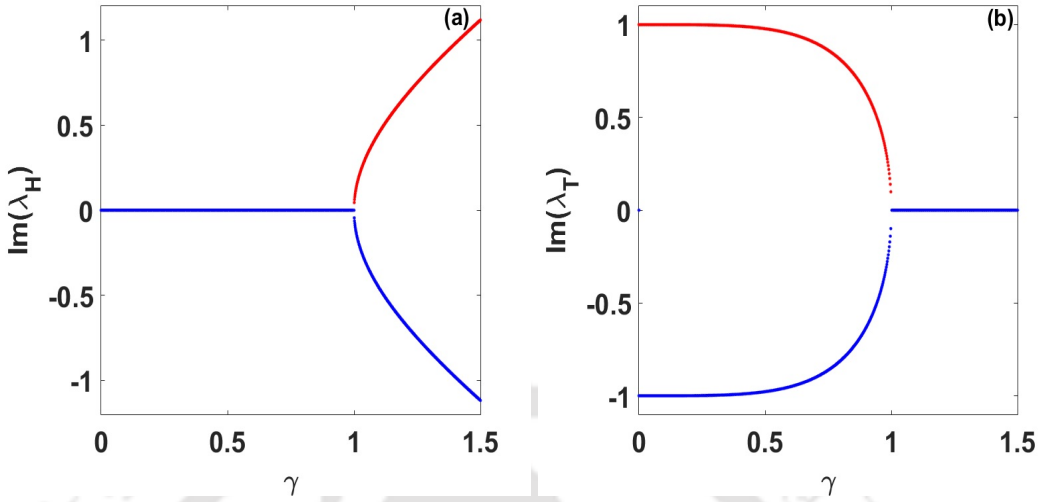

Figure 1.2: Eigen spectra of the (a) Hamiltonian $H_{\mathscr{PT}}$ and (b) Transfer Matrix T for $C = 1$.

1.3 Transfer Matrix Approach

In the transfer matrix approach, Eq. (1.3) are needed to be solved first. This is followed by the construction of the transfer matrix describing the evolution of optical power. Suppose, we launch electric field amplitudes $\psi_1(0)$ and $\psi_2(0)$ at the input ports of the waveguides. Then after propagating a distance $z = L_c$, the field amplitudes in the unbroken regime will be given by

$$\begin{pmatrix} \psi_1(L_C) \\ \psi_2(L_C) \end{pmatrix} = T \begin{pmatrix} \psi_1(0) \\ \psi_2(0) \end{pmatrix} \tag{1.4}$$

where T is the transfer matrix of the configuration. In the unbroken $\mathscr{PT}$ regime, the matrix elements are given by: $T_{11} = cos(pL_C) + \gamma sin(pL_C)/p$, $T_{12} = T_{21} = -iCsin(pL_C)/p$ and $T_{22} = cos(pL_C) - \gamma sin(pL_C)/p$, where $p = \sqrt{C^2 - \gamma^2}$. The parameter L_C, termed as the coupling length, is given by $L_C = \pi/2C$. Similarly, in the broken $\mathscr{PT}$ regime, we have $p = \sqrt{\gamma^2 - C^2}$ and all the sinusoidal terms in the transfer matrix will be replaced by their hyperbolic counterparts. Let us denote the eigenvalues of the transfer matrix as λ_T. In Fig. 1.2, we present the imaginary component of the eigen-spectra of the Hamiltonian and the Transfer Matrix approach. Fig. 1.2 depicts the imaginary component of the eigen-spectra for both the approaches. The $\mathscr{PT}$ threshold of the system, regardless of whether we use the Hamiltonian or the Transfer matrix formalism, remains unchanged, i.e. at $\gamma_{PT} = C$. The two approaches can only be distinguished in their eigen-spectra. In the Hamiltonian formalism, the eigen-spectra is entirely real in the unbroken regime

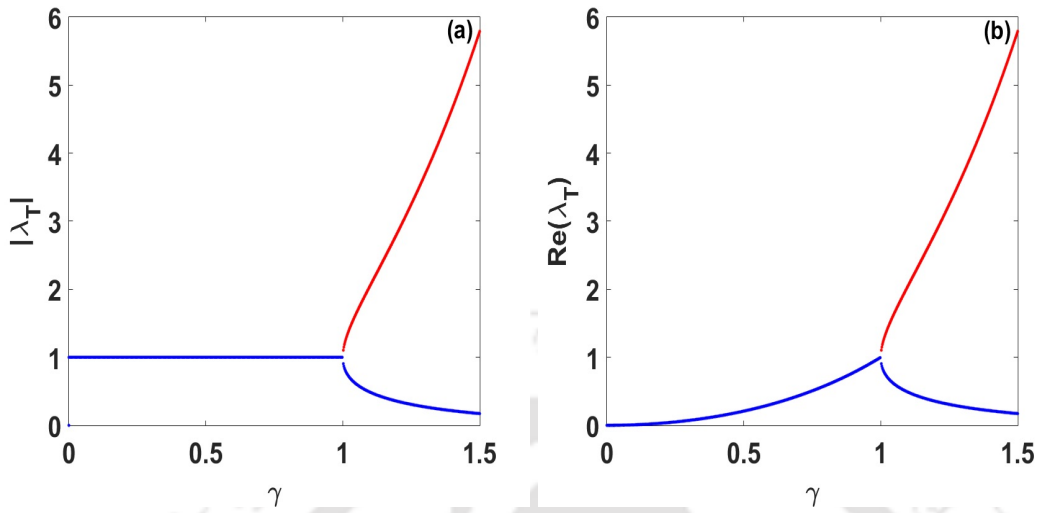

Figure 1.3: (a) $|\lambda_T|$ and (b) $Re(\lambda_T)$, as a function of γ.

and purely imaginary in the broken symmetry regime. On the other hand, in the transfer matrix formalism, the eigen-spectra are complex in the unbroken regime and real in the broken regime. To clarify this issue further, in Fig. 1.3, we plot the magnitude of the eigenvalues and the real part of the complex eigenvalues as a function of the loss/gain parameter. It could be seen from Fig. 1.3(a) that the magnitude of the eigenvalues is equal in the unbroken regime and beyond the $\mathscr{PT}$ threshold, they are no longer equal. This happens owing to the bifurcation of the real component of the eigenvalues at the $\mathscr{PT}$ threshold as could be seen in Fig. 1.3(b).

So far, we have discussed the relation between the Hamiltonian and the Transfer Matrix approach. We would now like to discuss the Transfer Matrix approach that has also been utilized to study discrete $\mathscr{PT}$-symmetric systems such as the optical mesh lattice [41]. The $\mathscr{PT}$ synthetic coupler as introduced in [41] comprises a passive coupling region and two channels of waveguides, one of which provides amplification and the other provides an equal amount of attenuation. The two channels are connected to the passive coupling region as shown in the schematic (Fig. 1.4). This configuration served as the building block of $\mathscr{PT}$ symmetric optical mesh lattices in the aforementioned work. The transfer matrix of this coupler is given by

$$M = \begin{pmatrix} e^{\gamma/2} & 0 \\ 0 & e^{-\gamma/2} \end{pmatrix} \frac{1}{\sqrt{2}} \begin{pmatrix} e^{\gamma/2} & 0 \\ 0 & e^{-\gamma/2} \end{pmatrix} = \frac{1}{\sqrt{2}} \begin{pmatrix} e^{\gamma} & i \\ i & e^{-\gamma} \end{pmatrix} \tag{1.5}$$

Analytically, it could be shown that the $\mathscr{PT}$ threshold of the transfer matrix is at $\gamma_{th} = cosh^{-1}(\sqrt{2})$. For $\gamma < \gamma th$, the supermodes of the transfer matrix are given by

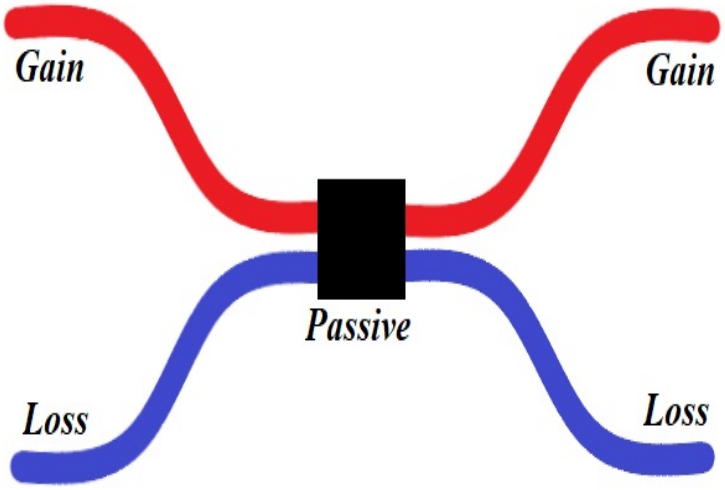

Figure 1.4: Schematic of a $\mathscr{PT}$-synthetic coupler. The blue-colored waveguide and the red-colored waveguide are the loss and gain channel respectively. They are coupled together in the black-colored region which is a passive 50:50 directional coupler.

$|\phi\rangle = \begin{pmatrix} 1 \\ e^{\pm i\eta} \end{pmatrix} e^{\pm i\omega}$, where $cos(\omega) = cos(\gamma)/\sqrt{2}$ and $sin(\omega) = cos(\eta)/\sqrt{2}$. Thus, it could be seen that in the unbroken $\mathscr{PT}$ regime, the modes repeat themselves as it propagates through the discrete system with a phase shift $e^{\pm i\omega}$. On the other hand, in the broken $\mathscr{PT}$ regime (i.e. $\gamma > \gamma_{th}$), the supermodes are $|\psi\rangle = \begin{pmatrix} 1 \\ ie^{\pm\eta} \end{pmatrix} e^{\pm\omega}$, where $cosh(\omega) = cosh(\gamma)/\sqrt{2}$ and $sinh(\omega) = sin(\eta)/\sqrt{2}$.

1.4 Harmonic Oscillator Approach

Before we begin our discussion on the harmonic oscillator approach, it would be prudent to take a look at this intuitive picture of two coupled harmonic oscillators with balanced gain and loss. In Fig. 1.5, if we operate the parity operator on this configuration of an absorber and an emitter using the border separating the two systems as an axis of symmetry, then the absorber will occupy the position of the emitter and the emitter will occupy the position of the emitter. And then on operating the time-reversal operator, the arrows that are depicting the flow of energy in Fig. 1.5 will be reversed. Essentially speaking, the absorber will be transformed to an emitter and the emitter will be transformed to an emitter. In a nutshell, it could be said that a damped harmonic oscillator coupled with an amplified harmonic oscillator will be a $\mathscr{PT}$-symmetric coupled oscillator

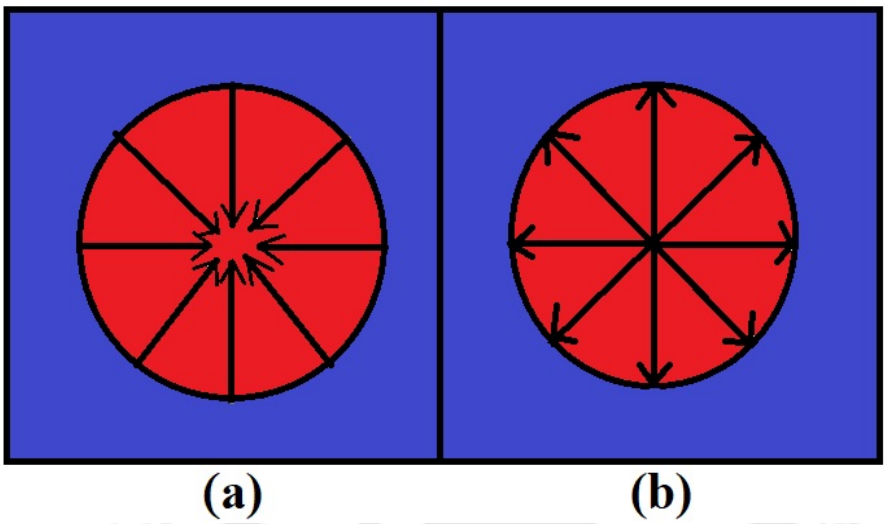

Figure 1.5: Schematic of (a) an absorber and (b) an emitter. The arrows depict the direction of flow of energy.

configuration. Now let us consider the damped harmonic oscillator given below.

$$\frac{d^2x}{dt^2} + \gamma\frac{dx}{dt} + x = 0 \tag{1.6}$$

where γ is the damping coefficient of the oscillator. Now, in such a classical oscillator system, the parity transformation is defined as $x \to -x$ and the time-reversal transformation is defined as $t \to -t$. It could be clearly seen that on joint operation of both these transformations on Eq. (1.6), the model would be transformed to $\ddot{x} - \gamma\dot{x} + x = 0$. This is the mathematical model of an amplified harmonic oscillator. So, the joint operation of the $\mathscr{PT}$-operator on a damped harmonic oscillator transforms it to its amplified counterpart. Now suppose both the oscillators are coupled as given below.

$$\frac{d^2x_1}{dt^2} + \gamma\frac{dx_1}{dt} + x_1 + \kappa x_2 = 0 \tag{1.7a}$$

$$\frac{d^2x_2}{dt^2} - \gamma\frac{dx_2}{dt} + x_2 + \kappa x_1 = 0 \tag{1.7b}$$

Here, κ is the coupling coefficient. Now, the damping coefficient, γ, of the oscillator plays the dual role of damping in the first oscillator and amplification in the second oscillator and is therefore termed as the gain/loss coefficient of the configuration. It could also be seen that this system satisfies the criteria laid down by Carl Bender, i.e. $x_1 \to x_2$, $x_2 \to x_1$ and $t \to -t$. C. M. Bender *et al.* studied such a $\mathscr{PT}$-symmetric harmonic oscillator configuration in one of his works [43]. Taking $\frac{dx_i}{dt} = y_i$, Eq. (1.7a) and (1.7b)

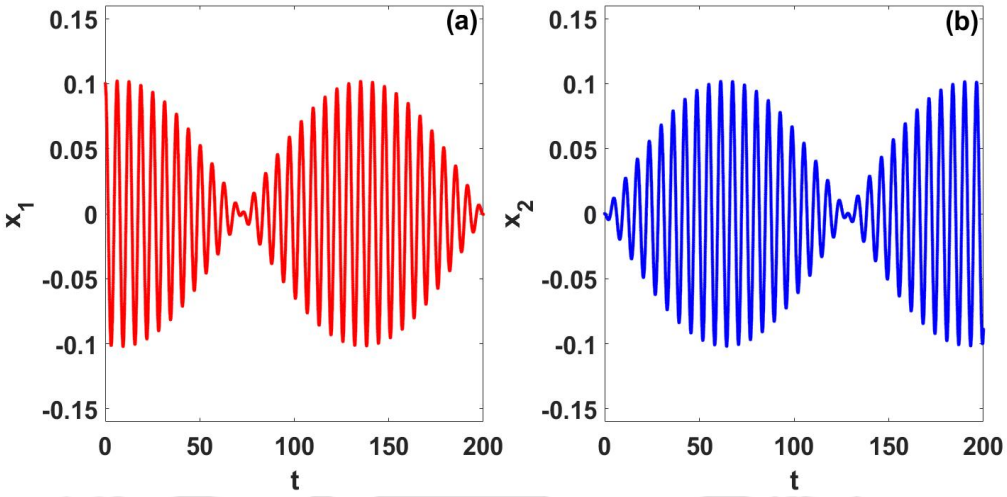

Figure 1.6: Temporal evolution of (a) x_1 and (b) x_2 for $\gamma = 0.01$ and $\kappa = 0.05$.

could be expressed compactly in the matrix form $\frac{dP(t)}{dt} = DQ(t)$, where the matrix D and vector $Q(t)$ are given by

$$D = \begin{pmatrix} 0 & 1 & 0 & 0 \\ -1 & -\gamma & -\kappa & 0 \\ 0 & 0 & 0 & 1 \\ -\kappa & 0 & -1 & \gamma \end{pmatrix} \text{ and } Q(t) = \begin{pmatrix} x_1(t) \\ y_1(t) \\ x_2(t) \\ y_2(t) \end{pmatrix}.$$

The stability of the system could be ascertained by calculating the eigenvalues of the matrix D. Setting the determinant of the matrix $D - EI$ equal to zero, we have

$$E^4 - (\gamma^2 - 2)E^2 - \kappa^2 + 1 = 0 \tag{1.8}$$

And the roots of this equation are given by

$$E^2 = (\gamma^2 - 2 \pm \sqrt{\gamma^4 - 4\gamma^2 + 4\kappa^2})/2 \tag{1.9}$$

The system will exhibit oscillatory temporal dynamics only when $\gamma^4 - 4\gamma^2 + 4\kappa^2 > 0$ and $\gamma^2 - 2 \pm \sqrt{\gamma^4 - 4\gamma^2 + 4\kappa^2} < 0$. From the second condition, we have $\kappa < 1$ and for small γ, from the first condition, we have $\gamma^2 < \gamma_{crit}^2 = 2(1 - \sqrt{1 - \kappa^2})$. γ_{crit} is the $\mathscr{PT}$ threshold of the system. We would now study the temporal evolution of the two oscillators in the broken and unbroken $\mathscr{PT}$ regimes. We have chosen the coupling constant of the oscillators as $\kappa = 0.05$ and we then have $\gamma_{crit} = 0.05$. As seen in Fig. 1.6, when the gain/loss coefficient of the oscillator is chosen below the coupling constant of the oscillator, we observe the temporal evolution to depict Rabi-like oscillations. This is the temporal

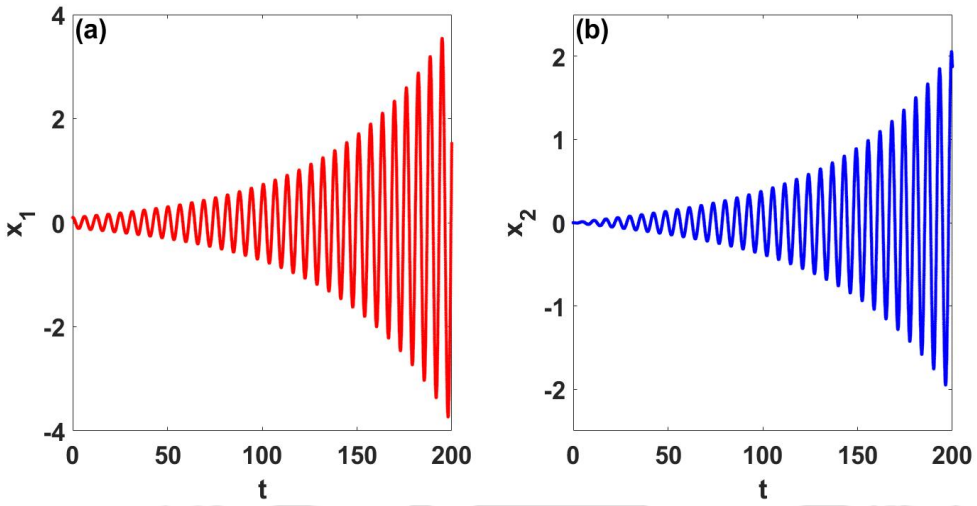

Figure 1.7: Temporal evolution of (a) x_1 and (b) x_2 for $\gamma = 0.06$ and $\kappa = 0.05$.

dynamics in the unbroken $\mathscr{PT}$ regime, i.e. $\gamma < \gamma_{crit}$. But when the gain/loss coefficient of the oscillator exceeds the coupling constant (i.e. in the broken $\mathscr{PT}$ regime), there is monotonically growing dynamics of $x_1(t)$ and $x_2(t)$ as seen in Fig. 1.7. This happens as a result of the balanced gain and loss in the two oscillators.

1.5 Organization of the Thesis

In this section, we give a brief overview of the various problems that have been tackled in the form of different chapters of the thesis.

Chapter 2 discusses the linearization Jacobian approach to study the stability of fixed points in a nonlinear system of ordinary differential equations. In addition to this, we explore the mathematical methods that are employed in the quantification of chaos in continuous-time as well as discrete-time nonlinear systems. First, we discuss the Lyapunov exponent method and its use in quantifying chaos in discrete-time nonlinear systems such as the logistic map and also use bifurcation analysis to validate the Lyapunov exponent method. After that, we concentrate on continuous-time nonlinear systems such as the forced Duffing oscillator and discuss in detail the power spectra method and how it could be used to analyze the emergence of chaotic dynamics in such systems.

In Chapter 3, we discuss our investigation of the nonlinear $\mathscr{PT}$-symmetric coupler from a dynamical perspective. As opposed to linear $\mathscr{PT}$-coupler where the $\mathscr{PT}$ threshold

dictates the evolutionary characteristics of optical power in the two waveguides, we find that, in a nonlinear coupler, the $\mathscr{PT}$ threshold governs the existence of fixed points. We have found that the stability of the ground state undergoes a phase transition when the gain/loss coefficient is increased from zero to beyond the $\mathscr{PT}$ threshold. Moreover, we find that instabilities in initial conditions could lead to aperiodic oscillations as well as exponential growth and decay of optical power. At the $\mathscr{PT}$ threshold, we observe the existence of a stable attractor under the influence of fluctuating gain/loss coefficient. Phase plane analysis has further shown us the presence of a toroidal attractor. Such dynamics could be controlled by a judicious choice of the waveguide parameters.

In Chapter 4, we discuss the implications of parity-time symmetry in discrete-time nonlinear systems known as the Ikeda Map. Ikeda Map is a mathematical model employed to study the temporal evolution of light going around in optical fiber ring resonators. We make use of the transfer matrix formalism of $\mathscr{PT}$-symmetry to model our problems. First, we show the possibility of controlling the dynamical behavior of a single fiber ring resonator system with the fiber being an amplified (gain) channel and the ring being attenuated (loss) nonlinear dielectric medium. We show that our model results in a dynamically controllable algorithm for the chaotic dynamics inherent in the system. We would then show the dependence of the period doubling point on the input amplitude, emphasizing on the dynamical aspects. Moreover, the fact that the resonator essentially plays the role of a damped harmonic oscillator has been elucidated with the non-zero intensity inside the resonator due to constant influx of input light. In the next major subsection, we introduce our work on the 'Chaotic Dynamics and Optical Power Saturation in $\mathscr{PT}$-Symmetric Double Ring Resonator'. In the linear regime of our reconfigured system, evolution of optical power in the system shows power saturation behavior below the EP and exponential blow-up above the EP. We find that in the unbroken $\mathscr{PT}$ regime, optical power saturation occurs owing to the existence of stable fixed point, which lies on the surface of 4-dimensional hypersphere. Inclusion of Kerr nonlinearity into our model leads to the emergence of a stable, chaotic and divergent region in the parameter basin for period-1 cycle. A closer inspection into the system shows us that the largest Lyapunov exponent blows up in the divergent region. Furthermore, we show that the existence of high non-negative largest Lyapunov exponent causes the emergence of chaotic spiking in the resonators.

Chapter 5 presents our study on the $\mathscr{PT}$-Symmetric dielectric-nanofilm-dielectric multilayered structure that could facilitate highly amplified transmission of optical

power in the infrared spectrum. We show how the transmission and reflection coefficient of the S-matrix is affected in the unbroken as well the broken $\mathscr{PT}$ regime. We then validate our theoretical findings using FDTD numerical simulation. After this, we show how the thickness of the layers and the gain/loss coefficient of the active layers could generate spectral singularities in the S-matrix and how these singularities could be exploited to achieve amplified transmission of a single wavelength through the structure.

In Chapter 6, we propose a $\mathscr{PT}$-Symmetric Liénard oscillator for two different configurations of nonlinear position dependent damping. The stability of fixed points has been analyzed using the linearization Jacobian approach. From the spectral analysis of the Jacobian eigen spectra, it was found that the system has a stable, an unstable and a saddle fixed point. It has been observed that when the initial conditions are chosen nearer to the stable fixed point, the time series instantly propagates towards the stable fixed point. But when the initial conditions are chosen far away from the stable fixed point, we observe that the temporal evolution of the gain oscillator exhibits blow-up dynamics. Using an external chirped drive on the loss oscillator, it has been found that such dynamics in our model could be controlled and oscillation death is achievable. On the other hand, in the second case, the phase plane trajectory exhibits the quasiperiodic route to chaos as the gain/loss coefficient is increased. Moreover, we validated this by a thorough analysis of the power spectra analysis of the temporal evolution of the gain oscillator. An experimental scheme to realize the proposed model has also been discussed.

And finally in Chapter 7, we would conclude our thesis with an emphasis on the findings and the future work that could be done based on the findings in this thesis.

CHAPTER 2

METHODOLOGY

2.1 Introduction

Nonlinear dynamics [44, 45] involves the study of nonlinear systems from a dynamical perspective. In general, nonlinear dynamics deals with study of systems whose governing equations could not be solved analytically. It provides us with a predictive ability of the nature of solution if we solve them on the computer. This predictive ability may not always conform to the system's exact dynamics. But nevertheless, it serves to reveal many interesting details within the system. Such systems often require advanced mathematical methods for analytical solution. The prime reason is that linear systems could be broken down into fragments. Most of them obey the laws of superposition and we have a wide range of mathematical tools like integral transforms, normal mode theory, etc. to solve such systems. But this is not the case for nonlinear systems. For instance, the differential equation governing the dynamics of the simple pendulum requires elliptic integrals of the first kind for analytical solutions. But an analysis of the stability of the fixed points (or stationary states) of the system using the linearization Jacobian approach reveals interesting temporal dynamics. Such systems fall under two distinct categories: nonlinear differential equations and iterative maps. The former falls under the domain of continuous-time systems, whereas the later falls under discrete-time systems. Mathematical models such as the Lorenz equation [46], Rössler equation [47], Duffing equation [48], etc. all belong to the former and as for the latter, we have the

Logistic map [49], the Hénon map [50], Ikeda map [51] and so on. This field of science has encompassed almost all other areas, e.g. chemistry [52-54], electronics [55], fluid dynamics [46], nonlinear optics [56-58], etc.

On the other hand, one important characteristic of most nonlinear systems is that they are sensitively dependent on the initial conditions. In continuous-time dynamical systems, such systems must be of at least 3 dimension to exhibit this characteristic. Take for instance, the driven Duffing oscillator. This is a nonlinear damped harmonic oscillator model, which is a second order nonlinear differential equation. But when it is driven by a sinusoidal force, the model becomes a non-autonomous system and the explicit time-dependence makes the entire system a 3 dimensional system of nonlinear differential equations and hence, it exhibits sensitiveness on initial conditions [46,48]. On the other hand, discrete-time systems such as the Logistic map need not be three dimensional to exhibit such features. And this characteristics of nonlinear systems, in the common tongue, is known as '*Chaos Theory*' and this idea was quite brilliantly summarized by Edward Lorenz in his saying: '*Chaos: When the present determines the future, but the approximate present does not approximately determine the future.*'

Most systems in optics exhibit some form of nonlinearity. We could take the example of Kerr nonlinearity in nonlinear optical waveguides. In a dispersive nonlinear optical waveguide, nonlinearity and dispersion counteract each other resulting in the formation of solitons [59]. Moreover, in ring cavity structure [51], the nonlinear phase shift imparted by the ring structure plays a very important role in the chaotic dynamics of the system. Even laser instability could be regarded as an outcome of some form of nonlinearity. Moreover, phenomena such as synchronization of chaos [60-61], stochastic resonance [62-63], chimera states [64], crowd synchrony [65], etc. have been observed in optical systems. The study of nonlinear dynamics in optical devices and systems is relevant to very practical technological applications such as compact disk players, fiber optic communications and the development of optical switching devices and laser arrays. And in fact, PT-symmetry breaking induced chaotic dynamics has also been investigated in optomechanical systems [39].

So, in this chapter, we aim to give the readers an exposition to the basic mathematical methods that are used in studying the stability of fixed points and quantification of chaos in nonlinear systems. This chapter has been divided into two main subsections. In section 2.2, we present the linearization Jacobian approach that is used in the analysis of fixed points in nonlinear systems. And in section 2.3, we present a brief discussion

on the quantification of chaos using Lyapunov exponent and Power Spectra analysis. Moreover, it must be noted that the terms stationary state and fixed point shall be used interchangeably in this thesis.

2.2 Stability Analysis of Nonlinear Systems

Consider the system of differential equations given below.

$$\dot{x} = f(x,y) \tag{2.1a}$$

$$\dot{y} = g(x,y) \tag{2.1b}$$

Here, $f(x,y)$ and $g(x,y)$ are nonlinear functions and this system has a fixed point at (x_0,y_0), i.e. at $x = x_0$ and $y = y_0$, $f(x_0,y_0) = g(x_0,y_0) = 0$. Now suppose we add an infinitesimal perturbation to the fixed point. Then Eq. (2.1a) would be transformed to $\dot{\delta x} = f(x_0+\delta x, y_0+\delta y)$, where δx and δy are the perturbation applied. Then, on using the Taylor Series expansion in two variables to expand $f(x_0+\delta x, y_0+\delta y)$, we have

$$\dot{\delta x} = f(x_0,y_0) + \delta x\left(\frac{\partial f}{\partial x}\right)_{(x_0,y_0)} + \delta y\left(\frac{\partial f}{\partial y}\right)_{(x_0,y_0)} + O((\delta x)^2,(\delta y)^2,\delta x\delta y) \tag{2.2}$$

Or we have

$$\frac{d}{dt}\delta x = a\delta x + b\delta y \tag{2.3}$$

where $f(x_0,y_0) = 0$, $a = \partial f/\partial x|_{(x_0,y_0)}$, $b = \partial f/\partial y|_{(x_0,y_0)}$ and we have neglected the higher order perturbation terms. Using the same method as described above, we could transform Eq. (2.1b) as follows.

$$\frac{d}{dt}\delta y + c\delta x + d\delta y \tag{2.4}$$

where $c = \partial g/\partial x|_{(x_0,y_0)}$ and $d = \partial g/\partial y|_{(x_0,y_0)}$. Hence, we could see that Eq. (2.3) and Eq. (2.4) could be written compactly in matrix form as follows.

$$\frac{d}{dt}\begin{pmatrix}\delta x\\ \delta y\end{pmatrix} = \begin{pmatrix}a & b\\ c & d\end{pmatrix}\begin{pmatrix}\delta x\\ \delta y\end{pmatrix} \tag{2.5}$$

Eq. (2.5) describes how the perturbation applied to the system would evolve with time and the matrix $J = \begin{pmatrix}a & b\\ c & d\end{pmatrix}$ is known as the linearization Jacobian. From the eigen spectra of this matrix, the stability of the fixed point could be ascertained from the eigenvalues, λ_i, of the Jacobian matrix and classified into four broad categories given below.

Fixed Point	Jacobian	Eigenvalues	Conclusion
(0,0)	$\begin{pmatrix} 3 & 0 \\ 0 & 2 \end{pmatrix}$	2, 3	Unstable
(0,2)	$\begin{pmatrix} -1 & 0 \\ -2 & -2 \end{pmatrix}$	-1, -2	Stable
(3,0)	$\begin{pmatrix} -3 & -6 \\ 0 & -1 \end{pmatrix}$	-3, -1	Stable
(1,1)	$\begin{pmatrix} -1 & -2 \\ -1 & -1 \end{pmatrix}$	$-1 \pm \sqrt{2}$	Saddle

Figure 2.1: Table showing the classification of the fixed points of the Lotka-Volterra Model.

1. Stable $\longrightarrow Re(\lambda_1) < 0$ and $Re(\lambda_2) < 0$
2. Unstable $\longrightarrow Re(\lambda_1) > 0$ and $Re(\lambda_2) > 0$
3. Saddle $\longrightarrow Re(\lambda_1) * Re(\lambda_2) < 0$
4. Neutral $\longrightarrow Re(\lambda_1) = Re(\lambda_2) = 0$

In literature, the stable fixed point is also known as the attractor and the unstable fixed point as the repeller [45]. On the other hand, the neutrally stable fixed point is also known as the center. The stability of such fixed points are termed as neutral because they are neither attracting nor repelling. We would now like to illustrate the application of this method by discussing the stability of the fixed points of the *Lotka-Volterra model* model, which is also known as the Predator-Prey model [45]. This model describes the interactions between two species and how these interactions affect the population of the two species in an ecosystem. These interactions could be mutualism, competition and so on. The mathematical equations of this model when the two species are subjected to competitive interactions in an ecosystem are given below.

$$\dot{x} = x(3 - x - 2y) \tag{2.6a}$$

$$\dot{y} = y(2 - x - y) \tag{2.6b}$$

It could be seen from Eq. (2.6) that in the absence of one of the species, the other would grow exponentially in an ecosystem where resources are available in abundance. But the nonlinear interactions between the two species give rise to very interesting dynamics in this *Lotka-Volterra model* of competition. The fixed points of this model are $(0,0)$, $(0,2)$,

$(3,0)$ and $(1,1)$ and the linearization Jacobian is $\begin{pmatrix} 3-2x-y & -2x \\ -y & 2-x-2y \end{pmatrix}$. From the eigen spectra of J, the stability of the fixed points are summarized in the table given in Fig. 2.1.

On the other hand, consider the discrete-time nonlinear system known as the *Logistic Map* given below.

$$x_{n+1} = f(x_n) \tag{2.7}$$

where $f(x_n) = \alpha x_n(1-x_n)$, α is a positive parameter and $0 \leq x \leq 1$. This is a highly celebrated model in nonlinear dynamics as it played a very important role in the development of the theory of chaos. It was first formulated by Pierre Francois Verhulst and later popularized by Robert M. May as a discrete-time iterative system to model the population dynamics in an ecosystem. Here, the variable x is the ratio of the existing population to the maximum possible population in the ecosystem. To evaluate the fixed points of this model, we take $x_n = x_{n+1} = x_0$ and then Eq. (2.7) could be written as follows.

$$x_0(1-\alpha-\alpha x_0) = 0 \tag{2.8}$$

The fixed points of the system are $x_{0,1} = 0$ and $x_{0,2} = (\alpha-1)/\alpha$. The fixed point $x_{0,1}$ is valid for all values of α. But the fixed point $x_{0,2}$ is valid only for $\alpha \geq 1$, since $0 \leq x \leq 1$. We would now like to study the stability of these fixed points. Suppose we add an infinitesimal perturbation to the fixed point x_0 given by $|\delta_n| = |x_n - x_0|$ and study whether x_n will asymptotically approach x_0 or not for large n. We then have

$$|\delta_{n+1}| = |x_{n+1} - x_0| \tag{2.9}$$

By substituting $f(x_n) = f(x_0+\delta_n)$ in place of x_{n+1} and carrying out a Taylor series expansion of $f(x_0+\delta_n)$ and neglecting the higher order terms, we have

$$|\delta_{n+1}| = |f^{'}(x)_{x=x_0}||\delta_n| \tag{2.10}$$

Thus, in the vicinity of a stable fixed point, the perturbation δ_n must asymptotically decrease with each successive time-step, i.e. $|\delta_{n+1}| < |\delta_n|$ or $|\delta_{n+1}|/|\delta_n| < 1$. Hence, from Eq. (2.10), the condition for the stability of the fixed point x_0 is given by

$$|f^{'}(x)_{x=x_0}| < 1 \tag{2.11}$$

For the Logistic Map, the fixed point $x_0 = 0$ is stable for $0 \leq \alpha < 1$ and unstable for $\alpha > 1$. On the other hand, the fixed point $x_0 = (\alpha-1)/\alpha$ is stable is stable for $1 < \alpha < 3$ and

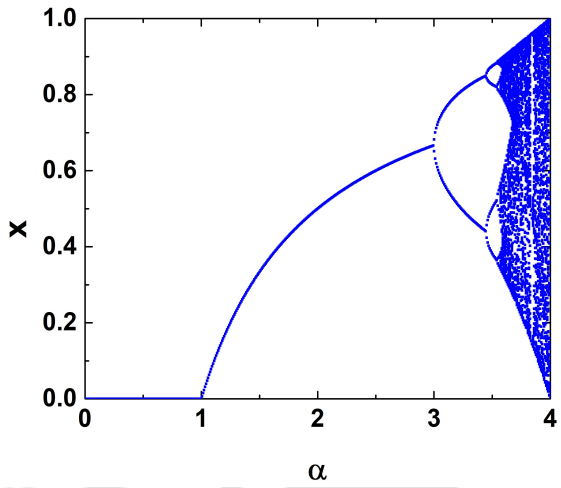

Figure 2.2: Bifurcation diagram of the Logistic Map.

unstable for $\alpha > 3$. This could easily be seen from the bifurcation diagram of the Logistic Map in Fig. 2.2. To plot the bifurcation diagram, we have considered 1000 as the total number of iterations, out of which we have discarded 900 iterations as transients and plotted the remaining 100 iterations. We could see from the bifurcation diagram (Fig. 2.2), that for $0 < \alpha < 1$, the stable fixed point is $x = 0$ as pointed out above. Similarly, in the regime $1 < \alpha < 3$, the expected behavior is seen. But beyond $\alpha = 3$, it could be seen that the population ratio now oscillates between two values. This form of bifurcation is known as period doubling phenomenon. On further increasing α, the population ratio begins oscillating between four values. It could be seen that, beyond a critical value of the parameter α, there is onset of chaotic dynamics in the system and this route to chaos is known as the period-doubling cascade to chaos.

2.3 Quantification of Chaos

Chaos could be quantified in nonlinear systems using different methods. In this section, we would be discussing the Lyapunov exponent method and the Power Spectra method. The Lyapunov exponent method is a very useful in quantifying chaos in systems such as the Logistic map, which shows the period-doubling cascade to chaos. On the other hand, the power spectra method is quite useful in studying the emergence of chaos in systems that exhibit the quasiperiodic route to chaos. To illustrate these two methods, we would make use of the Logistic Map and the driven Duffing oscillator as examples.

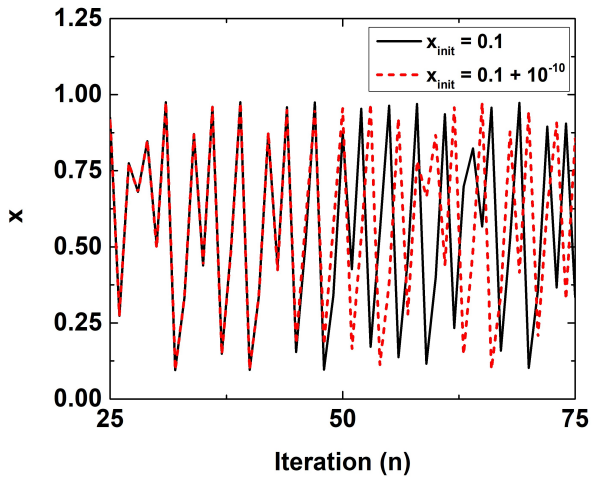

Figure 2.3: Time series of the Logistic Map for $\alpha = 3.9$ and initial conditions: $x_{init} = 0.1$ (black line) and $x_{init} = 0.1 + 10^{-10}$ (red dash).

Before we begin discussing the Lyapunov exponent method, we would like to talk about the topic called 'Sensitiveness on Initial Conditions'. The credit for discovering this characteristic of nonlinear systems goes to the MIT mathematician Edward Lorenz [46]. It so happened that Lorenz was attempting to solve a set of nonlinear ordinary differential equations on an old computer. At first, he was using initial conditions correct up to sixth decimal places. But due to his computations taking too much time, he decided to use initial conditions correct up to third decimal places and he ended up getting results that really got him surprised. It is quite logical to think that if you change a little at the beginning, it is going to change a little at the end. But these systems don't behave that way. This characteristic in nonlinear systems could be easily seen in the Logistic Map as well. To illustrate this characteristic of nonlinear systems, we would like to discuss the time series of the Logistic Map taking into account the initial conditions - $x_{init} = 0.1$ for the first case and $x_{init} = 0.1 + 10^{-10}$ for the second case and $\alpha = 3.9$. The largest Lyapunov exponent for this chosen parameter in Fig. 2.3 is $\lambda_{max} = 0.51343$, which means that the system is in the chaotic regime and this is what we observe in the time-series we have plotted in Fig. 2.3. It could be seen that as we impart an infinitesimal perturbation of the order of 10^{-10} to the initial condition in the second case, the time-series shows completely different behavior. This characteristic in nonlinear systems is known as '*Sensitiveness on Initial Conditions*'. We would now like to begin our discussion on the quantification of chaos in nonlinear systems using the Lyapunov exponent method. The Lyapunov

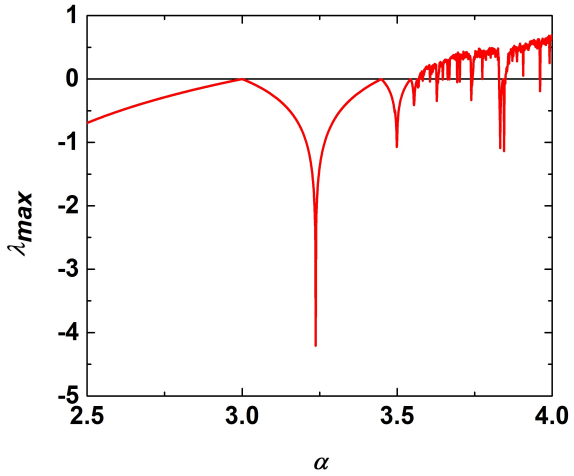

Figure 2.4: Maximal Lyapunov exponent (λ_{max}) of the Logistic Map.

exponent of any dynamical system measures the rate at which two infinitesimally close trajectories would evolve with time [66]. It is named after the Russian mathematician A. M. Lyapunov. Mathematically, it is defined as

$$\lambda = \lim_{x\to\infty} \frac{1}{n} \sum_{i=0}^{n-1} ln \left| \frac{df(x_i)}{dx} \right| \tag{2.12}$$

In Fig. 2.4, we have plotted the maximal or largest Lyapunov exponent (λ_{max}) vs. the parameter α for the Logistic Map. It could be seen that when $\alpha < 3$, λ_{max} is negative. This means that the stationary state $x_0 = (\alpha - 1)/\alpha$, as evaluated in the previous section, is stable. But at $\alpha = 3$, λ_{max} is zero. This means that $\alpha = 3$ is the period-doubling point and for $\alpha > 3$, the system will oscillate between two states. Period doubling takes place once again at $\alpha = 3.4486$ and as α is increased further, the largest Lyapunov exponent become positive, thereby indicating the emergence of chaotic dynamics in the system.

So far, we have been discussing the period doubling to chaos in discrete-time nonlinear system and now we would like to discuss chaotic dynamics in continuous-time nonlinear systems such as the driven Duffing oscillator given below.

$$\ddot{x} + \gamma\dot{x} + \eta x + \beta x^3 = f_0 cos(\omega t) \tag{2.13}$$

Here, γ, η, β, ω and f_0 are all given real constants. It could be shown that the potential function of the Hamiltonian of this model is given by $V(x) = \eta x^2/2 + \beta x^4/4$ and this potential function has three extremas at $x = 0$ and $x = \pm\sqrt{-\eta/\beta}$. For $\eta > 0$ and $\beta > 0$, $V(x)$ has one single equilibrium point at $x = 0$, which is a minima. On the other hand, for $\eta < 0$

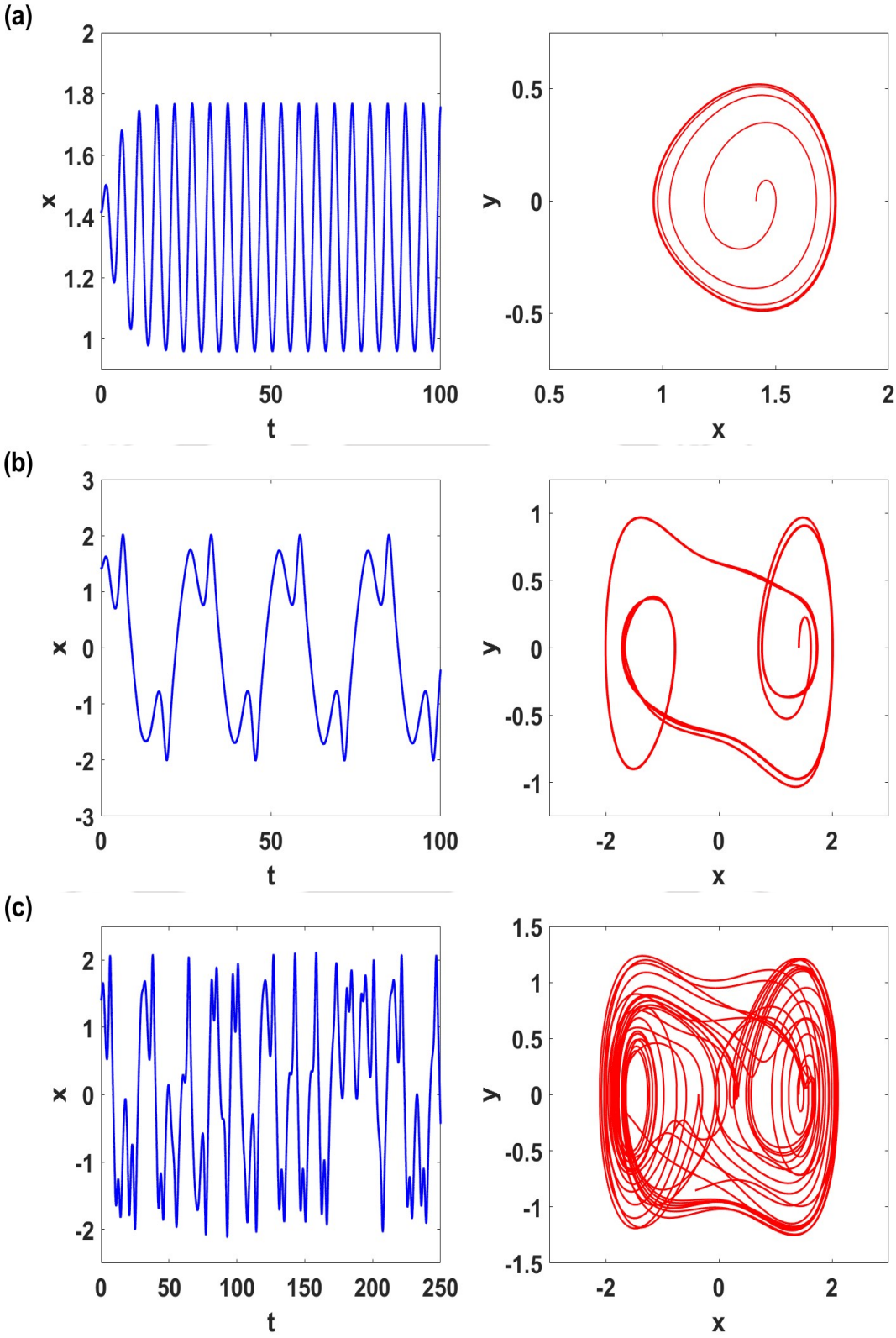

Figure 2.5: Temporal Evolution and Phase Plane of the driven Duffing oscillator (Eq. (2.13)) for $\gamma = 0.3$, $\beta = 0.5$, $\eta = -1$ and $\omega = 1.2$ in all the cases: (a) $f_0 = 0.20$, (b) $f_0 = 0.5$ and (c) $f_0 = 0.575$.

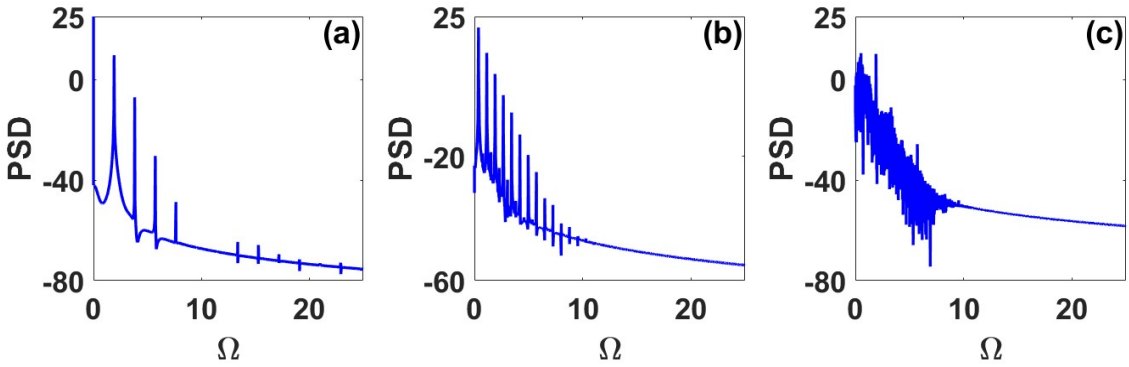

Figure 2.6: Power Spectral Density ($P(\Omega)$) of the driven Duffing oscillator (Eq. (2.13)) (a) $f_0 = 0.2$, (b) $f_0 = 0.5$ and (c) $f_0 = 0.575$. Other parameters: $\gamma = 0.3$, $\beta = 0.5$, $\eta = -1$ and $\omega = 1.2$.

and $\beta > 0$, we have two minimas at $x = \pm\sqrt{-\eta/\beta}$ and a maxima at $x = 0$. And finally for $\eta > 0$ and $\beta < 0$, we have a minima at $x = 0$ and two maxima at $x = \pm\sqrt{-\eta/\beta}$. The stability analysis of the extremas of the potential gives us a physical picture as to why we have chaotic dynamics in the driven Duffing oscillator. Choosing the initial condition of the system chosen to be $(\sqrt{-\eta/\beta}, 0, 0)$, we have presented in Fig. 2.5 the temporal evolution and the phase plane for three cases of the amplitude of the driving signal (f_0). It must be noted here that the initial condition $(\sqrt{-\eta/\beta}, 0, 0)$ is one of the stable stationary state of the system. In Fig. 2.5, we have plotted the temporal evolution and the phase plane of the driven Duffing oscillator for three cases of the driving signal amplitude. It could be seen that for low amplitude, the temporal evolution shows a period-1 oscillation response and the same could be observed from the phase plane diagram which is a limit cycle. But as we increase the amplitude of the driving signal to $f_0 = 0.5$, the temporal evolution shows a period-3 oscillation response and on further increasing to $f_0 = 0.575$, the temporal evolution shows the emergence of a chaotic time-series and a strange attractor (Fig. 2.5(c)). Moreover, for our chosen parameters ($\eta < 0$ and $\beta > 0$), the system has two stable stationary states at $x = \pm\sqrt{-\eta/\beta}$ and it could be seen from the phase plane of the chaotic attractor that the system is now oscillating erratically between these two states. This could be further analyzed from the power spectral density of the temporal evolution [44] which is given by:

$$P(\Omega) = |x(\Omega)|^2 \tag{2.14}$$

where $x(\Omega)$ is the Fourier transform of the time series. From Fig. 2.6(a), it could be seen that the entire lower frequency region is populated for $f_0 = 0.20$ in the power spectrum with sharp peaks that are all subharmonics of the fundamental mode at $\Omega = 1.908$ and

this is why we have a limit cycle oscillator as shown in Fig. 2.5(a). The power spectral density plot shows the same characteristics for $f_0 = 0.50$ in Fig. 2.6(b). But for $f_0 = 0.575$, the entire lower frequency could be seen to be populated in the lower frequency domain and then, the power spectral density exponentially decays in the higher frequency domain. This leads us to the inference that increasing the amplitude of the driving signal causes the emergence of a chaotic attractor in the driven Duffing oscillator. Moreover, from our calculation of the largest Lyapunov exponents for the three cases of the driving signal amplitude, we have found that $\lambda_{max} = -0.0586168$ for $f_0 = 0.2$, $\lambda_{max} = -0.102276$ for $f_0 = 0.5$ and $\lambda_{max} = 0.0499292$ for $f_0 = 0.575$. Due to the presence of negative λ_{max} in the first two cases and the external drive, the temporal dynamics in Fig. 2.5(a) and Fig. 2.5(b) depicts the convergence into a limit cycle attractor. On the other hand, in the third case, we have $\lambda_{max} > 0$ for $f_0 = 0.575$ and as a result, we have the emergence of a chaotic attractor in the phase plane. Hence, in conclusion, we could say that quantification of chaos in discrete-time as well as continuous-time nonlinear system could be done by the application of power spectral analysis as well as Lyapunov exponent.

CHAPTER 3

PERTURBATIVE DYNAMICS OF STATIONARY STATES IN A NONLINEAR $\mathscr{PT}$-SYMMETRIC COUPLER

3.1 Introduction

The parity-time symmetric coupler is a coupled waveguide configuration consisting of two evanescently coupled gain-loss waveguide pair. The mathematical model governing the spatial evolution of optical power in the two waveguides could be analytically solved if the system is devoid of any form of nonlinearity. But in the presence of nonlinearity, analytical solution is not possible and prior assumptions are required. Moreover, it may be noted here that, in the linear regime, the spatial evolution of optical power in the waveguides undergoes a phase transition from oscillatory to exponential growth as the gain/loss coefficient of the waveguides is increased beyond the $\mathscr{PT}$ threshold. But in the presence of Kerr nonlinearity, mathematical evaluation of the $\mathscr{PT}$ threshold is not possible and further analysis is required. K. Li and P. G. Kevrekidis studied this system by taking stationary waves into consideration [67], whereas H. Ramezani *et al.* used Stokes' parameters to study the conserved quantities in the system [68]. Moreover, I. V. Barashenkov devoted considerable time to the study and analysis of the $\mathscr{PT}$-symmetric dimer. Some of his work include the analysis of blow-up regimes [69], Hamiltonian

Part of the results of this Chapter have been published in the following papers: J. P. Deka and A. K. Sarma, "Perturbative dynamics of stationary states in nonlinear parity-time symmetric coupler," Communications in Nonlinear Science and Numerical Simulation 57, 26 (2017).

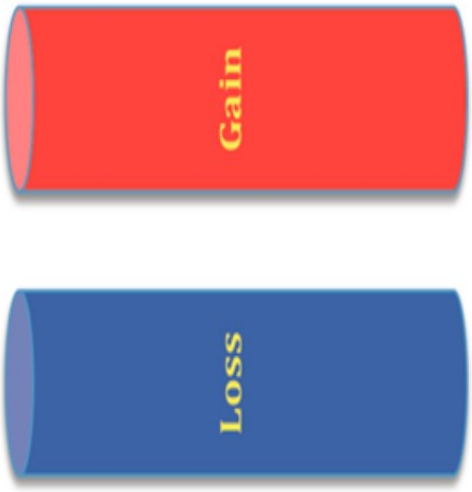

Figure 3.1: Schematic of the $\mathscr{PT}$-symmetric coupler with gain (top waveguide) and loss (bottom waveguide).

formulation [70], integrability, symmetry restoration and so on in the $\mathscr{PT}$-symmetric coupler [71]. Furthermore, there has also been numerous investigations of such coupled optical waveguide structures, which are also known as '*Oligomer*'. Some of them include $\mathscr{PT}$-symmetry breaking in a necklace of waveguides [72], bifurcations and ghost states in the $\mathscr{PT}$-symmetric trimer [73], attractor perspective in the $\mathscr{PT}$-symmetric quadrimer [74] and so on.

In the same line of research, this chapter aims to study the nonlinear $\mathscr{PT}$-symmetric coupler from a dynamical point of view. A thorough stability analysis of the stationary states of the system is carried out using the linearization Jacobian approach. This gives us a clearer and detailed interpretation of the dynamics when it is subjected to the presence of Kerr nonlinearity. We have further studied the effect of fluctuations in the gain/loss coefficient of the waveguides as well.

3.2 Modelling

The $\mathscr{PT}$-symmetric nonlinear coupler is a configuration consisting of two waveguides in close proximity so as to facilitate the transfer of optical power from one waveguide to the other via evanescent coupling. One waveguide can amplify the input optical signal and the other can attenuate the signal by the same proportion. Schematic of the coupler is shown in Fig. 3.1. The equations [68] governing the spatial evolution of optical power in

the two waveguides are given by

$$i\frac{da_1}{dz} = i\gamma a_1 + Ca_2 + |a_1|^2 a_1 \tag{3.1a}$$

$$i\frac{da_2}{dz} = -i\gamma a_2 + Ca_1 + |a_2|^2 a_2 \tag{3.1b}$$

Here, a_1 and a_2 are the field amplitudes and γ characterizes the gain/loss in the two channels and C is the coupling constant. Both waveguides portray Kerr nonlinearity of equal strength. In the absence of Kerr nonlinearity, the $\mathscr{PT}$ threshold is given by $\gamma_{th} = C$. But adding the nonlinearity alters the entire dynamics of the system. The reason is that once the system is modified with the inclusion of nonlinear terms, the initial conditions will play a major role in the dynamics of optical power evolution. It must be noted here that the $\mathscr{PT}$ threshold of the linear coupler will be used as a reference point to study the stability analysis.

3.3 Stability Analysis and Discussion

We shall first consider the ground state of the coupler defined by: $a_1 = a_2 = 0$. This set of initial condition corresponds to unexcited waveguides. To ascertain the stability of the ground state, we will expand the differential equations using the prescription $a_1 = x_1 + iy_1$ and $a_2 = x_2 + iy_2$. Eq. (3.1) could then be rewritten as follows:

$$\frac{dx_1}{dz} = \gamma x_1 + Cy_2 + (x_1^2 + y_1^2)y_1 \tag{3.2a}$$

$$\frac{dy_1}{dz} = \gamma y_1 - Cx_2 - (x_1^2 + y_1^2)x_1 \tag{3.2b}$$

$$\frac{dx_2}{dz} = -\gamma x_2 + Cy_1 + (x_2^2 + y_2^2)y_2 \tag{3.2c}$$

$$\frac{dy_2}{dz} = -\gamma y_2 - Cx_1 - (x_2^2 + y_2^2)x_2 \tag{3.2d}$$

The linearization Jacobian is given by

$$J = \begin{pmatrix} \gamma + 2x_1y_1 & x_1^2 + 3y_1^2 & 0 & C \\ -(3x_1^2 + y_1^2) & \gamma - 2x_1y_1 & -C & 0 \\ 0 & C & -\gamma + 2x_2y_2 & x_2^2 + 3y_2^2 \\ -C & 0 & -(3x_2^2 + y_2^2) & \gamma - 2x_2y_2 \end{pmatrix} \tag{3.3}$$

The Jacobian eigenvalues are calculated to be $\lambda = \pm\sqrt{\gamma^2 - C^2}$. For $\gamma < C$, all eigenvalues of the Jacobian are purely imaginary indicating that the ground state is a non-hyperbolic

stationary state. Linear stability analysis fails if the stationary state under consideration is non-hyperbolic [75]. In mathematical terms, if all the eigenvalues are purely imaginary (i.e. $Re(\lambda_i) = 0$), the stationary state is classified as non-hyperbolic. In such a case, numerical solution of the system, under a suitably chosen perturbation, reveals the exact nature of the stationary state [76]. On the other hand, if one or some of the eigenvalues contain non-zero real part the stationary state is categorized as hyperbolic. In such cases, linear stability analysis is sufficient. Above the $\mathscr{PT}$ threshold, the Jacobian has two positive and two negative eigenvalues. This means that the ground state is an unstable saddle stationary state and even the slightest excitation imparted to one of the waveguide will lead to an exponential growth and decay of the optical power in the two waveguides. But within the unbroken $\mathscr{PT}$ regime, an in-depth analysis of the system reveals that our model admits non-zero stationary states and in order to evaluate them, we resort to a polar form of Eq. (3.2) which would provide us with much more interesting picture of the non-zero stationary states and the dynamics therein. Using $r_i = (x_i\dot{x}_i + y_i\dot{y}_i)/r_i$ and $\theta_i = (x_i\dot{y}_i - y_i\dot{x}_i)/r_i^2$, Eq. (3.2) could be rewritten as follows:

$$\frac{dr_1}{dz} = \gamma r_1 + Cr_2 sin(\theta_2 - \theta_1) \tag{3.4a}$$

$$\frac{dr_2}{dz} = -\gamma r_2 - Cr_1 sin(\theta_2 - \theta_1) \tag{3.4b}$$

$$\frac{d\theta_1}{dz} = -\frac{Cr_2 cos(\theta_2 - \theta_1)}{r_1} - r_1^2 \tag{3.4c}$$

$$\frac{d\theta_2}{dz} = -\frac{Cr_1 cos(\theta_2 - \theta_1)}{r_2} - r_2^2 \tag{3.4d}$$

Eq. (3.4c) and (3.4d) corresponding to the phases θ_1 and θ_2 can be coupled using $\theta = \theta_2 - \theta_1$ as follows:

$$\frac{d\theta}{dz} = C\left(\frac{r_2}{r_1} - \frac{r_1}{r_2}\right) cos(\theta_2 - \theta_1) + (r_1^2 - r_2^2) \tag{3.5}$$

We define θ as the relative phase lag parameter. The non-zero stationary states of our configuration are found to be:

$$r_1 = r_1 = r^* \tag{3.6a}$$

$$\theta = 2\pi - sin^{-1}\left(\frac{\gamma}{C}\right) \tag{3.6b}$$

Physically, this means that the stationary states correspond to light inputs of equal optical power and the field in one waveguide lags behind by θ in phase with respect to the other. It can be clearly seen from Eq. (3.6b) that the nonlinear dimer admits no

stationary states for $\gamma > C$. This suggests that even in the presence of nonlinearity, the threshold point remains unchanged. In a linear coupler, the $\mathscr{PT}$ threshold dictates the evolutionary characteristics of optical power in the two waveguides. On the other hand, in a nonlinear coupler, the $\mathscr{PT}$ threshold governs the existence of stationary states. To analyze the dynamics and stability of the non-zero stationary states, we will need to use the linearization Jacobian J^* corresponding to Eq. (3.4a), (3.4b) and (3.5), given below

$$J^* = \begin{pmatrix} \gamma & Csin(\theta) & Cr_2cos(\theta) \\ -Csin(\theta) & -\gamma & -Cr_1cos(\theta) \\ \alpha & \beta & \gamma \end{pmatrix} \tag{3.7}$$

Here, $\alpha = -C(r_1^2 + r_2^2)cos(\theta)/r_2r_1^2 + 2r_1$, $\beta = C(r_1^2 + r_2^2)cos(\theta)/r_1r_2^2 - 2r_2$ and $\delta = C(r_1^2 - r_2^2)sin(\theta)/r_1r_2$. The eigenvalues of J^* are found to be

$$\lambda_1 = 0 \tag{3.8a}$$

$$\lambda_2 = \sqrt{\gamma^2 - C^2sin^2(\theta) - 2ACr^*cos(\theta)} \tag{3.8b}$$

$$\lambda_3 = -\sqrt{\gamma^2 - C^2sin^2(\theta) - 2ACr^*cos(\theta)} \tag{3.8c}$$

where $A = 2Ccos(\theta)/r^* - 2r^*$. The stability analysis will be now studied in two domains. We will study the stability of the non-zero stationary states (Eq. (3.6a) and (3.6b)) for $\gamma < C$ followed by our analysis of the same at the threshold point $\gamma = C$. For $\gamma < C$, the non-zero eigenvalues of J^* could be further simplified to $\pm\sqrt{4C((r^*)^2 - Ccos(\theta))cos(\theta)}$. From these eigenvalues, we can see that the initial launch conditions present another threshold on the stability of the system. This newfound threshold could be evaluated to be $r^*_{th} = \sqrt{Ccos(\theta)}$ which on further simplification gives

$$r^*_{th} = (C^2 - \gamma^2)^{\frac{1}{4}} \tag{3.9}$$

If $r* > r^*_{th}$, one of the Jacobian is a positive real quantity, which means that the stationary state is an unstable saddle stationary state. For instance, when $\gamma = 0.9$ and $C = 1$, we have $r^*_{th} = 0.6602$. Numerical solution of our configuration shows that if the initial conditions are chosen such that $r^* < r^*_{th}$, the optical power in both waveguides ($P_1 = r_1^2$ and $P_2 = r_2^2$) exhibits aperiodic oscillations provided one of the launch conditions is subjected to some order of perturbation. This has been clearly illustrated in the plots shown below. In Fig. 3.2, the initial launch conditions for both waveguides have been chosen below the threshold (Eq. (3.9)) and one of them have been subjected to a perturbation of the order of

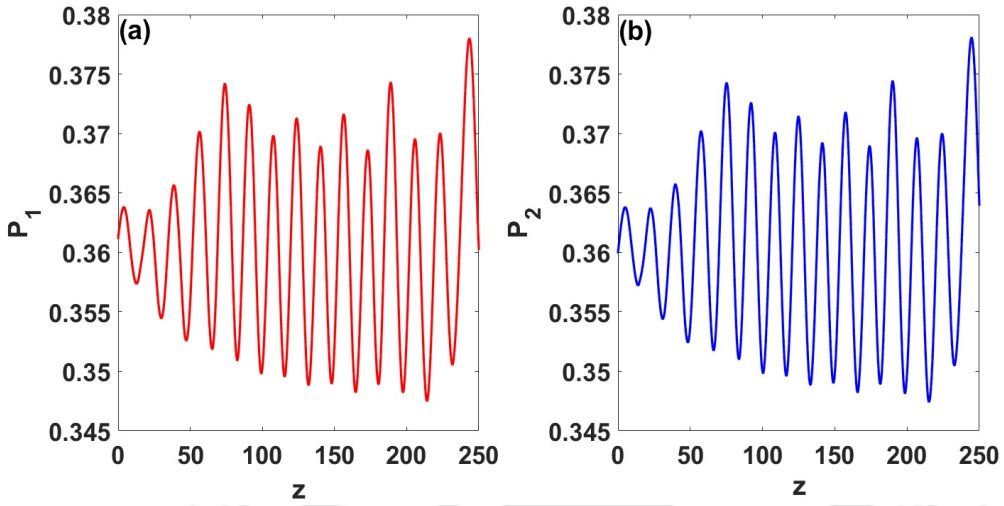

Figure 3.2: Spatial evolution of optical power in (a) waveguide '**1**' and (b) waveguide '**2**' for $\gamma = 0.9$. Initial conditions: $r_1 = 0.6 + 10^{-4}$, $r_2 = 0.6$ and $\theta = 5.1634$.

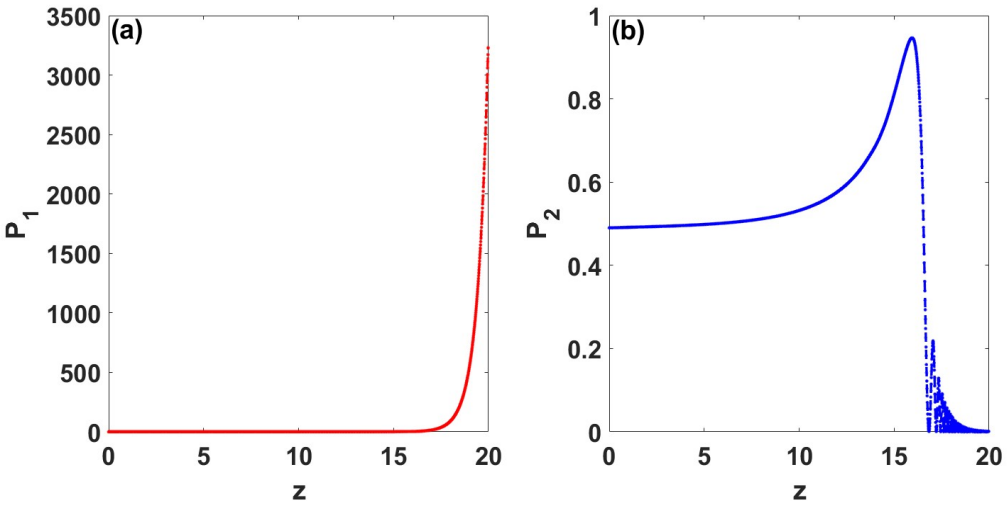

Figure 3.3: Spatial evolution of optical power in (a) waveguide '**1**' and (b) waveguide '**2**' for $\gamma = 0.9$. Initial conditions: $r_1 = 0.7 + 10^{-4}$, $r_2 = 0.7$ and $\theta = 5.1634$.

10^{-4}. This has been done in order to visualize the stability of the initial launch conditions under the influence of fluctuations. The gain/loss coefficient has been set at $\gamma = 0.9$ and accordingly, the threshold is evaluated to be: $r^*_{th} = 0.6602$. So, in order to satisfy $r^* < r^*_{th}$, we chose $r_1 = 0.6 + 10^{-4}$ and $r_2 = 0.6$. And the relative phase lag, θ, has been decided in accordance with Eq. (3.6b). This gives rise to aperiodic oscillations in the spatial propagation of optical power in their respective waveguides. On a closer inspection, we could clearly see that optical power fluctuates on the order of 10^{-2} in both waveguides.

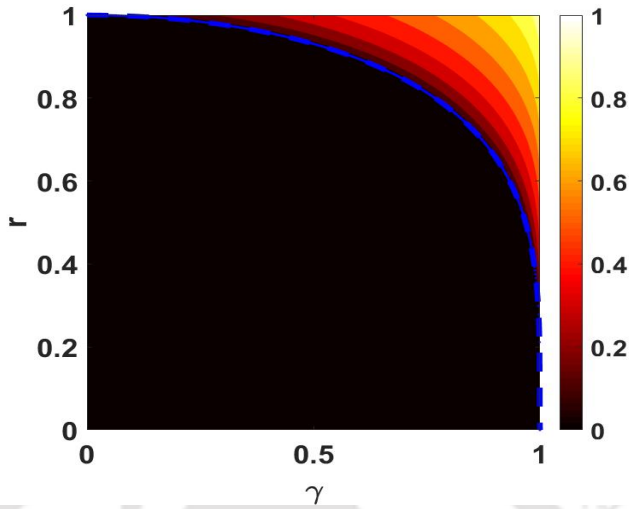

Figure 3.4: Contour plot of the real component of the Jacobian eigenvalues vs. r and γ. The blue colored dashed line is the plot of Eq. (3.9).

On the other hand, if $r^* > r^*_{th}$, power evolution in both waveguides will exhibit characteristics similar to that of a linear coupler in the broken $\mathscr{PT}$ regime. This has been shown in Fig. 3.3. The initial launch conditions are chosen in a similar manner as considered for the case $r^* < r^*_{th}$. Fig. 3.3 depicts the exponential growth and decay of optical power in the two channels. As it has been pointed out before, this happens because one of the eigenvalue of J^* is real positive and our stability analysis clearly shows that the stationary state is unstable. Similar dynamics in spatial evolution of optical power has been observed in the linear coupler when the gain/loss coefficient is taken above the $\mathscr{PT}$ threshold. But in our analysis, we have seen that even the choice of initial conditions matters a lot and this could be attributed to the presence of Kerr nonlinearity in our model. To present this aspect of our system in a clearer manner, Fig. 3.4 depicts the contour plot of the real part of the Jacobian eigenvalues. Moreover, we have also included the plot of Eq. (3.9) (blue colored dashed line). This has been done in order to dwell on the lower bound of r above which the Jacobian has real eigenvalues. Above this line, the system is in an unstable state for any given initial launch conditions.

For the analysis with regard to the dynamics of the system at the $\mathscr{PT}$ threshold, we choose $C = 1$. At the $\mathscr{PT}$ threshold, the relative phase lag given by Eq. (3.6b) is $\theta = 3\pi/2$. It is very interesting to note here that under these circumstances, all eigenvalues of the linearization Jacobian J^* are zero. A study of the numerical solution and the corresponding phase plane analysis has been done by choosing a set of initial conditions

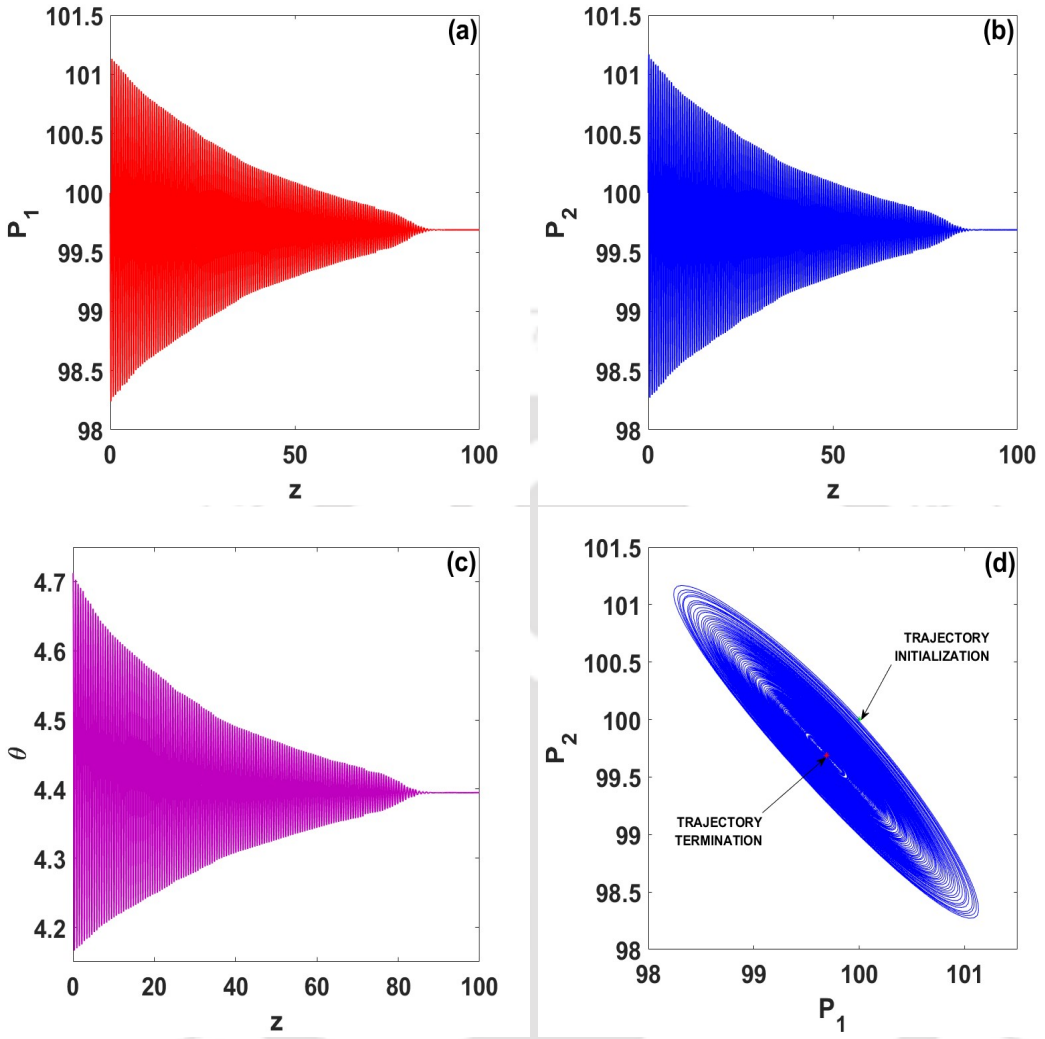

Figure 3.5: (a) Spatial evolution of optical power in waveguide '**1**' and (b) waveguide '**2**' (c) Spatial evolution of relative phase lag θ and (d) Phase plane of optical power in both waveguides. Initial Conditions: $r_1 = r_2 = 10$ and $\theta = 4.7124$.

corresponding to the stationary states at the $\mathscr{PT}$ threshold. Since, all the Jacobian eigenvalues are zero at the $\mathscr{PT}$ threshold, we have the freedom to choose r^* at any arbitrary value, whereas the relative phase lag is set at $\theta = 3\pi/2$. We present two aspects of our configuration, one of which is the attractor aspect and the other is chaotic behavior in the real and imaginary component of the field amplitudes. The gain/loss coefficient is set at $\gamma = 0.95$. This is done to see as to how fluctuations in γ affect the dynamics of optical power in a nonlinear $\mathscr{PT}$-symmetric coupler, provided the initial launch conditions conform to the stationary states corresponding to the $\mathscr{PT}$ threshold. Fig. 3.5 (a-c) depicts decay in oscillations of the evolution of optical power and the relative

phase lag along the propagation distance. It must be noted here that this happens when the initial conditions are chosen for $\gamma = C$ using Eq. (3.6a)-(3.6b) and a slight change in the gain/loss coefficient is introduced. We could see that the oscillations decay in the initial stage and slowly approaches a constant value. Moreover, phase plane analysis (Fig. 3.4d) of the optical power in both waveguides shows a spiral trajectory that is spiraling inwards and this is sufficient for us to ascertain the existence of an attractor in our configuration. Numerical computation shows that the attractor state is located at $r_1 = r_2 = 9.9844$ and $\theta = 4.394852$. From Eq. (3.6b), the attractor stationary state concerning the relative phase lag θ corresponds to $\gamma = 0.95$. This is in exact agreement with our altered value of gain/loss coefficient. We could say that if our initial conditions are chosen such that they correspond with the stationary states at the $\mathscr{PT}$ threshold, any disturbance in γ will redirect the trajectory to an attractor state which coincides with the stationary state of the altered gain/loss coefficient. Moreover, we could see that there is some loss in the initial optical power after an initial run of decaying oscillations. From this we could infer that the loss in optical power is compensated by a change in the relative phase lag between the two optical fields.

On the other hand, it must be noted here that even though the relative phase lag θ becomes constant after the field amplitudes has propagated some distance, the individual phases of the field amplitudes θ_1 and θ_2 do not become constant. The reason behind this could be attributed to the fact that the stationary states we have been dealing with so far are those of Eq. (3.4a), (3.4b) and (3.5). So to extract the information on the evolution of θ_1 and θ_2, we need to proceed with the numerical solution of Eq. (3.4a)-(3.4d). This way, we could demonstrate the dynamics of the real and imaginary component of the field amplitudes.

Phase plane analysis of the real and imaginary component of the field amplitude (Fig. 3.6) in waveguide '1' shows a toroidal trajectory, which vanishes as γ approaches the $\mathscr{PT}$ threshold. In Fig. 3.6(a-c), we could see the presence of two circular orbits within which the real and imaginary components oscillate. On a closer look, we could see that in Fig. 3.6(a), there is a third circular orbit, which lies very close to the inner orbit. But it vanishes in Fig. 3.6(b). As γ increases, the outer orbit could be seen to approach the blue-colored dashed circular orbit, which is the limit cycle. In Fig. 3.6(c), radius of the outer orbit vanishes and that radius of the outer circular orbit also decreases significantly and finally in Fig. 3.6(d), the two orbits merges with each other into the limit cycle attractor when $\gamma = C$. This is similar to *Sil'nikov orbits* [77,78]. The presence

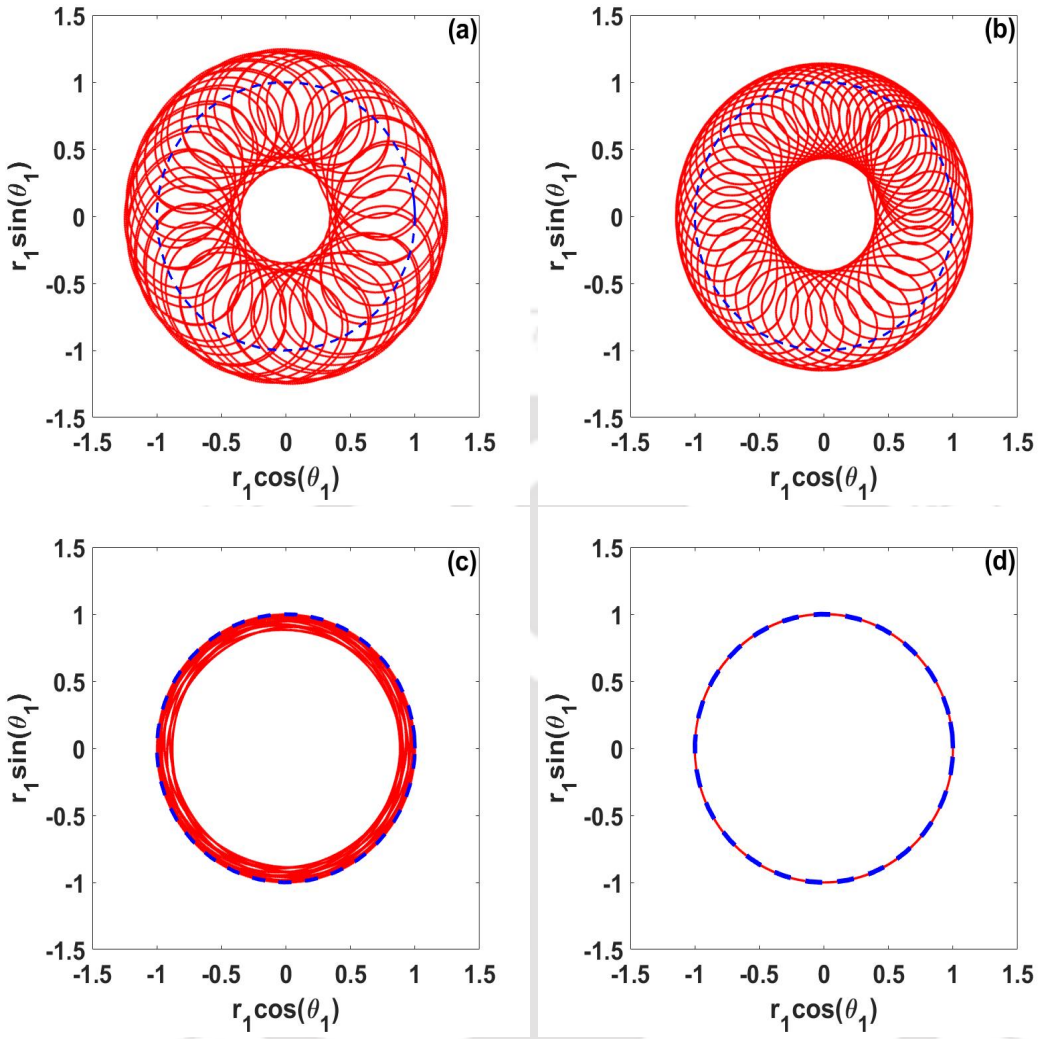

Figure 3.6: Phase Plane trajectory of the real and imaginary component of the field amplitude in waveguide '**1**' for (a) $\gamma = 0.25$, (b) $\gamma = 0.5$, (c) $\gamma = 0.99$ and (d) $\gamma = 1$. Initial Conditions: $r_1 = r_2 = 1$, $\theta_1 = 0$ and $\theta_2 = 4.7124$.

of such orbits implies a chaotic trajectory, which vanishes under the influence of some parametric changes. In our case, we have a toroidal trajectory which disappears at the $\mathscr{PT}$ threshold and it takes the form of a limit cycle.

3.4 Summary

In conclusion, we have investigated several aspects of the nonlinear $\mathscr{PT}$-symmetric coupler from a dynamical perspective. As opposed to linear $\mathscr{PT}$-coupler where the $\mathscr{PT}$ threshold dictates the evolutionary characteristics of optical power in the two waveguides,

in a nonlinear coupler, the $\mathscr{PT}$ threshold governs the existence of stationary states. We have found that the stability of the ground state undergoes a phase transition when the gain/loss coefficient is increased from zero to beyond the $\mathscr{PT}$ threshold. Moreover, in the unbroken $\mathscr{PT}$ regime, we find that the instabilities in the initial launch conditions could trigger an exponential growth and decay of optical power in the waveguides. Also, it could redirect the spatial power evolution into aperiodic oscillations. The attractor behavior of the system has also been studied under fluctuations in the gain/loss coefficient. From our phase plane analysis, we could ascertain that such a system exhibits self-stabilizing characteristics. And finally, we have shown that the phase plane trajectory of the real and imaginary component of the field amplitudes is a toroidal phase plane trajectory. Such chaotic trajectory could be controlled with judicious choice of waveguide parameters.

CHAPTER 4

CHAOTIC DYNAMICS IN FIBER RING RESONATORS WITH BALANCED GAIN AND LOSS

4.1 Introduction

Amongst the pioneers who studied the emergence of chaotic dynamics in optical systems, Kensuke Ikeda was the first who studied such phenomena in optical ring cavities [51]. Ikeda's model studied the evolution dynamics of light going around a ring cavity which comprises a passive nonlinear element and a time delayed feedback loop. The time-delayed feedback loop can induce chaotic dynamics in the entire system. The chaotic dynamics in such systems are mathematically governed by either the pulse driven nonlinear differential equation [79] or the discrete-time iterative equation known as the Ikeda Map [51]. In literature, such systems are also referred to as Ikeda-type optical systems. Over the years, period doubling route to chaos [80], modulational instability [81], dynamical pulse shaping [82], temporal instabilities [83], etc. are some of the phenomena that have been studied theoretically as well as experimentally in such systems.

On the other hand, $\mathscr{PT}$-symmetry breaking induced chaotic dynamics [39] has been studied recently in cavity optomechanics. They found that chaos emerges in the system when the driving laser applied to the cavity mode lasts for a period. In this chapter, we discuss the chaotic dynamics that emerges in optical ring cavities with balanced gain and loss. This chapter has been divided into two major subsections. In the first subsection, we

would study the controllability of chaotic dynamics in a single fiber ring resonator system with balanced gain and loss. In this configuration, a lossy nonlinear ring structure is coupled to an amplified input channel by a 50:50 directional coupler. Here, the nonlinear ring structure serves as a feedback loop to induce chaos in the system. On the other hand, in the second subsection, we discuss a double ring resonator system with balanced loss and gain. It is a coupled Ikeda-type optical system in which there are two feedback loops. One of the feedback loop is optically pumped to amplify the field propagating in it and the other feedback loop is doped to provide damping by the same proportion. Both of them exhibit Kerr nonlinearity of equal strength. The feedback loops are allowed to interact via a 50:50 directional coupler. A detailed discussion on the role of the gain/loss coefficient, the strength of Kerr nonlinearity and the input field amplitude has been presented.

4.2 Controllable chaotic dynamics in nonlinear fiber ring resonators with balanced gain and loss*

In this section, in a single fiber resonator (SFR) system with balanced gain and loss modeled by Ikeda map, we intend to study the effects of the balanced gain and loss profile upon the evolution dynamics of the input optical field over a sufficiently large number of round-trips in the ring cavity. Essentially speaking, our model is an alternative version of the Ikeda Map studied using the transfer matrix formalism by Lynch [84]. In Lynch's work, a 50:50 directional coupler splits the input light into an output channel and a looped resonating channel, which suffers a nonlinear phase shift as it passes through the fiber ring. It is then fed back into one input of the directional coupler. On the other hand, our system takes a cue from a recently published work on $\mathscr{PT}$-Symmetric Optical Mesh Lattice [41, 85-87] and uses the mathematical framework of transfer matrix so as to study the system using the Ikeda map.

This section is organized as follows. In section 4.2.1, we discussed the theoretical modelling of our system using the transfer matrix approach. And then in section 4.2.2, we discussed the dynamical aspects of our systems, followed by an analysis of the resonance profile of the system and the temporal dynamics of the system in the stable regime. And

*Part of the results of this section have been published in the following papers: J. P. Deka, S. K. Gupta and A. K. Sarma, "Controllable chaotic dynamics in nonlinear fiber ring resonators with balanced gain and loss," Nonlinear Dynamics 87, 1121 (2017).

finally, we have concluded our discussion with an emphasis on the technological aspects of our model.

4.2.1 Theoretical Modelling

In this section, we would how slight modifications in the $\mathscr{PT}$-synthetic coupler [41,85-87] could result in a dynamically chaos controllable ring resonator system. The system has been modified in such a way that the output port from the loss channel has been fed back into its input. And we consider the loss channel to be a nonlinear dielectric medium. This provides us with a nonlinear lossy resonator channel. Using the transfer matrix of the $\mathscr{PT}$-synthetic coupler given in Eq. (1.5), we could write the output amplitudes in terms of the input amplitudes of the schematic shown in Fig. 4.1 as follows:

$$\begin{pmatrix} E_{out} \\ E_1 \end{pmatrix} = \frac{1}{\sqrt{2}} \begin{pmatrix} e^{\gamma} & i \\ i & e^{-\gamma} \end{pmatrix} \begin{pmatrix} E_{in} \\ E_2 \end{pmatrix} \tag{4.1}$$

Here, γ is defined as the gain/loss parameter. And it must be noted that there is no evanescent coupling between the optical fibers. From the transfer matrix, it could be said that our system couples an amplified and an attenuated light input via a 50:50 directional coupler and redirects one output back into directional coupler after it has traversed a lossy nonlinear resonating channel and the other output is sent to a detector to study the evolution dynamics in the system. The field suffers a nonlinear phase shift when it travels one complete loop across the ring. So, we can write $E_2 = E_1 e^{i\phi}$ where $\phi = \phi_L + \phi_{NL}$ is the total phase shift suffered by the field and we have $t_R = nL/c$, where 't_R' is the round-trip time for one complete loop of the electromagnetic wave around the resonator and 'L' is the length of the resonator, 'n' is the effective refractive index in the resonator. The nonlinear phase shift, ϕ_{NL}, is given by:

$$\phi_{NL} = \frac{2Ln_2\pi|E_2|^2}{A_{eff}\lambda_0} \tag{4.2}$$

Here, n_2 is the nonlinear refractive index coefficient, A_{eff} is the effective core area of the fiber and λ_0 is the wavelength of the propagating light in vacuum. Using Eq. (4.1), we can write the discretized field amplitude evolution equation in the resonator taking time steps equal to t_R in the form of an iterative equation:

$$E_{j+1} = A + BE_j e^{i(\phi_L + \phi_{NL})} \tag{4.3}$$

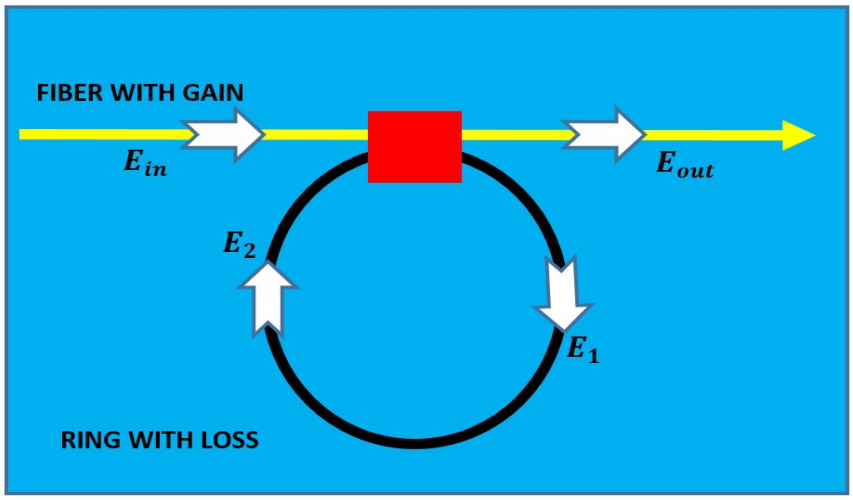

Figure 4.1: Schematic diagram of the SFR resonator structure. The '**yellow-color**' region represents the fiber with gain, the '**black-color**' ring represents the resonator with loss and the '**red-color**' rectangular block is the passive coupling region. E_{in} is the input light, E_{out} the output light and E_1 being the part of input light transferred through coupling region, and E_2 the part of light going to couple back to the input light.

where $A = iE_{in}/\sqrt{2}$ and $B = e^{-\gamma}/\sqrt{2}$. Without loss of generality, taking $\phi_L = 0$, we can Eq. (4.3) as:

$$E_{j+1} = A + BE_j e^{i|E_j|^2} \tag{4.4}$$

In Eq. (4.4), we have considered the coefficient before $|E_j|^2$ as unity since this facilitates us to study the dynamical behavior of the system without a prior choice of the parameters of the ring resonator. And now, for the sake of convenience, we now separate Eq. (4.4) into a two-dimensional form as follows:

$$x_{j+1} = \frac{-y_{in}}{\sqrt{2}} + \frac{e^{-\gamma}\left[x_j cos\left(x_j^2 + y_j^2\right) - y_j sin\left(x_j^2 + y_j^2\right)\right]}{\sqrt{2}} \tag{4.5a}$$

$$y_{j+1} = \frac{x_{in}}{\sqrt{2}} + \frac{e^{-\gamma}\left[x_j sin\left(x_j^2 + y_j^2\right) + y_j cos\left(x_j^2 + y_j^2\right)\right]}{\sqrt{2}} \tag{4.5b}$$

Here, $x_j = Re(E_j)$, $y_j = Im(E_j)$, $x_{in} = Re(E_{in})$ and $y_{in} = Im(E_{in})$. We would now like to derive the resonance profile of the resonator optical power. In fact, it is straightforward to work out the resonator optical power from Eq. (4.4). Taking $E_{j+1} = E_j$, we can rewrite Eq. (4.4) as follows.

$$E_j - e^{-\gamma}E_j e^{i\phi}/\sqrt{2} = iE_{in}/\sqrt{2} \tag{4.6}$$

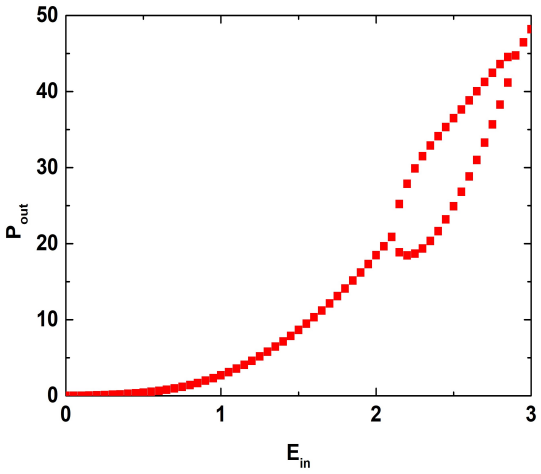

Figure 4.2: P_{out} vs. E_{in} for $\gamma = 1.0$.

It must be noted here that the mathematical expression for the resonance profile could be calculated only when the system is in a stable stationary state and this is why we have taken $E_{j+1} = E_j$. Now multiplying Eq. (4.6) with its complex conjugate, it could be shown that the resonance profile of resonator optical power is given by

$$P_{resonance} = \frac{|E_{in}|^2}{e^{-2\gamma} + 2 - 2\sqrt{2}e^{-\gamma}cos(\phi)} \tag{4.7}$$

At resonance, $\phi = 2\pi m$, where m is an integer. Using Eq. (4.3) and setting $g = n_2/A_{eff}\lambda_0$, the resonance condition is found to be: $m = Lg|E_2|^2$, provided $\phi_L = 0$. Here, g is the nonlinear parameter.

4.2.2 Results and Discussion

The system displays rich behavior in the context of nonlinear dynamics. The number of round trips light takes in the resonator (or iterations) shows how the optical power evolves in the resonator. This evolution is governed by Eq. (4.5). Now because the ring resonator is an lossy medium, optical power flowing in it will be attenuated. As the iteration progresses, the system slowly enters the steady state. Now depending on the value of γ, the ring can either be in a chaotic state or contain a single stable optical power, which are primarily the stationary states of Eq. (4.5). Taking $x_{j+1} = x_j$, it is straightforward to show that the existence of the stationary states of Eq. (4.5) is

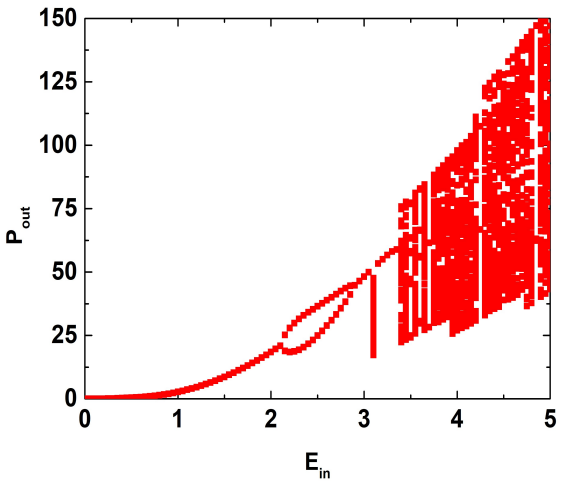

Figure 4.3: P_{out} vs. E_{in} showing the chaotic behavior of the system for E_{in} beyond 3.0 for $\gamma = 1.0$.

governed by the parametric equation given below.

$$\left(x_j + \frac{y_{in}}{\sqrt{2}}\right)^2 + \left(y_j - \frac{x_{in}}{\sqrt{2}}\right)^2 - \frac{e^{-2\gamma}}{\sqrt{2}}\left(x_j^2 + y_j^2\right) = 0 \tag{4.8}$$

Taking a fixed value of γ, we carried out 1000 iterations and discarded 900 out of this 1000 iterations as transients and plot the remaining 100 steady state iterations. Fig. 4.2 clearly shows the highly amplified out optical power $P_{out} = |E_{out}|^2$ that we obtain for a given value of input field amplitude E_{in}. We also observe two different optical power for a certain range of E_{in}. It is worth noting that if we increase γ, the bifurcation behavior will cease to exist beyond a certain limit. On the other hand, if we proceed to increase E_{in} beyond 3.0, as depicted in Fig. 4.3, we encounter a chaotic region beyond a certain point because $\gamma = 1.0$ is not sufficient to counteract the chaotic dynamics of the system. The reason for this can be attributed to the fact that the ring resonator in our configuration is an optical power absorber and chaos could be controlled in our system by increasing the loss parameter γ of the nonlinear ring resonator.

So, up to certain input amplitude, the resonator can attenuate the influx of energy and prevent the system from transcending into chaotic dynamics, but beyond a certain value, it fails in this aspect and we would observe chaotic transmission of optical power in the output port. The role of the loss parameter γ can be illustrated by plotting a bifurcation diagram of optical power in the resonator $P_{res} = |E_2|^2$ vs. the loss parameter γ. In Fig. 4.4(a), the bifurcation behavior in the resonator optical power on varying γ has been depicted. The system exhibits the period doubling route to chaos. As γ decreases,

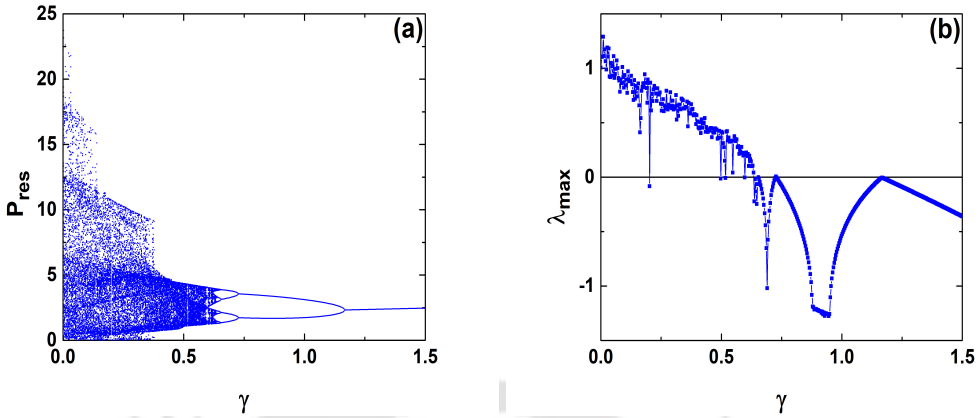

Figure 4.4: (a) Bifurcation diagram of P_{res} and (b) λ_{max} vs. γ for $E_{in} = 2.5$.

the resonator optical power bifurcates into two distinct values, which increases to four on further decreasing γ and eventually we enter into a region of chaotic dynamics. It could be seen that the period doubling point lies close to $\gamma = 1.2$ and that γ plays a crucial role in the transition of the system to a chaotic state or in other words, we could claim that γ plays the role of a chaos control parameter.

A plot of the largest Lyapunov exponent (λ_{max}) vs. loss parameter γ, shown in Fig. 4.4(b), further validates our above-mentioned claim. For γ above 1.2, the system has negative λ_{max} meaning that the resonator contains a single stable optical power, as it is evident from the bifurcation diagram. In the region of γ from 0 to 0.6, λ_{max} is positive indicating that the system is in the chaotic regime. Now, a numerical algorithm could be designed which computes the value of γ at which period doubling takes place for different values of E_{in}. This presents us with a set of γ corresponding to the input amplitude E_{in}, which has been shown in Fig. 4.5.

The period doubling point shifts its value in accordance with E_{in}. Fig. 4.5 tells us as to how the system should be designed so as to observe a single optical power in the output, for a single stable optical power in the resonator will ensure the same in the output. In other words, the period doubling point as calculated numerically for each value of E_{in} corresponds to a maximal limit of γ beyond which fluctuation in the resonator optical power has been observed to be on the order of 10^{-5}.Some of the values of E_{in} and γ used to plot Fig. 4.5 are $(2.0, 0.90)$, $(2.5, 1.19)$, $(3.0, 0.92)$, $(3.5, 1.90)$ and $(4.0, 2.53)$.

Now, we would like to study the resonance profile of our model. Typically, for a Gaussian modal distribution, if the nonlinear refractive index n_2 is chosen to be of order

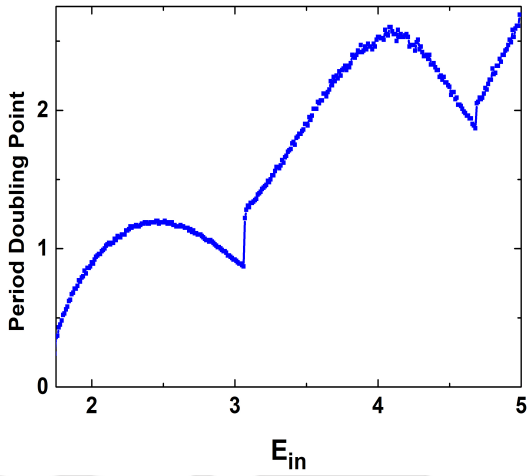

Figure 4.5: Period doubling point vs. E_{in}.

$10^{-20} m^2 W^{-1}$, g takes values in the range of 10^{-3}-$10^{-2} W^{-1}/m$. Moreover, the nonlinear parameter g can be increased by decreasing A_{eff}. Taking these parameter values under consideration, the resonance spectrum can be estimated using Eq. (4.7). Numerically, $\gamma = 0.92$ has been found to restore the resonator optical power dynamics into a steady state when $E = 3.0$. The resonance spectrum for this particular case has been shown below. Fig. 4.6 depicts the resonance profile with wavelength range chosen in the visible spectrum. The resonator optical power is peaked around $550 - 600nm$, which clearly indicates that this configuration, if properly engineered, can be utilized for practical purposes.

To ascertain as to how our system behaves as it is allowed to evolve, we have taken into account one set of parameters and use them to plot, in Fig. 4.7, the optical power in the resonator vs. iteration. Fig. 4.7 shows us that the resonator behaves like a damped harmonic oscillator, but the optical power does not decay down to zero owing to the fact that there is a constant influx of optical power, which is being fed to the resonator. The loss ring plays the role of a damping medium and the input amplitude acts as the driving force in the system. Moreover, we have considered the ring to be a nonlinear dielectric medium. These elements are also a part of the pulse driven nonlinear oscillator equation [79] from which the Ikeda map is derivable and this justifies the behavior shown in Fig. 4.7. Hence, we can infer from the above plots that γ plays the role of a chaos control parameter in our configuration. This work so far, on firm grounds, has validated the fact that the idea of a $\mathscr{PT}$ synthetic coupler can be converted into a simple fiber ring

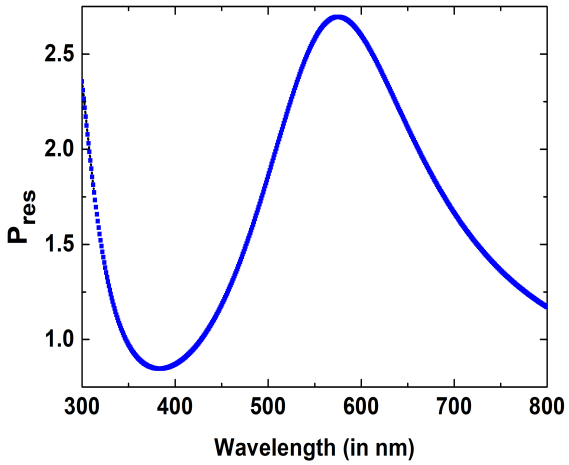

Figure 4.6: Resonance profile for $E_{in} = 3.0$ and $\gamma = 0.92$. The parameters chosen are: $n_2 = 2.6 * 10^{-20} m^2 W^{-1}$, $A_{eff} = 10^{-14} m^2$ and $L = 0.5m$.

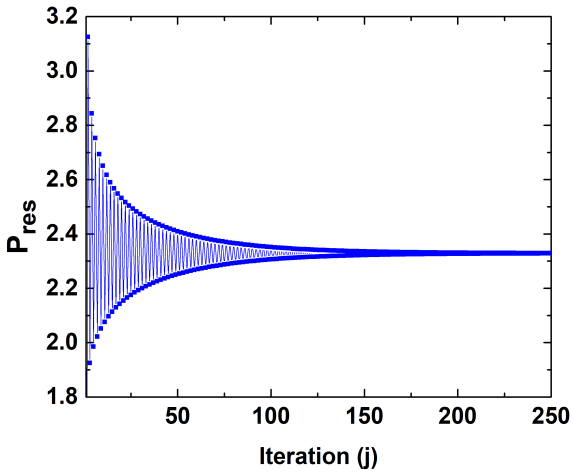

Figure 4.7: Temporal evolution of the resonator optical power for $E_{in} = 2.5$ and $\gamma = 1.19$.

resonator with a control parameter that is solely dependent on the fiber characteristics. In addition to this, the fluctuations in the optical power at the output port could be controlled via altering the value of γ.

4.2.3 Summary

In conclusion, we found that simple alterations in the $\mathscr{PT}$-symmetric synthetic coupler structure could result in a dynamically controllable algorithm for the chaotic dynamics

inherent in the system. We have also shown the dependence of the period doubling point upon the input amplitude, emphasizing on the dynamical aspects of our system. Moreover, the resonance profile of the structure emphasizes the experimental realization of the system for technological aspects. Furthermore, the fact that the resonator essentially plays the role of a damped harmonic oscillator has been elucidated with the non-zero optical power inside the resonator due to constant influx of optical power. Despite the fact that in our system, there is no distinct $\mathscr{PT}$ threshold point enabling us to study the dynamics of the system in both the broken and unbroken $\mathscr{PT}$ regime, our study could be seen as a step forward to further investigations in regard to the control of chaotic dynamics in optical ring resonator systems.

4.3 Optical Power Saturation and Chaotic Dynamics in a $\mathscr{PT}$-Symmetric Double Ring Resonator*

In this sub-section, we would discuss the evolution of optical power in a double ring resonator system with balanced loss and gain. In our previous work (section 4.2), the system is devoid of any $\mathscr{PT}$ threshold and as such, the configuration we studied is not $\mathscr{PT}$-Symmetric. Moreover, it must be noted that a $\mathscr{PT}$-Symmetric coupled oscillator configuration requires the presence of a gain and loss oscillator coupled to each other. In this section, we would discuss a configuration in which one lossy ring resonator is coupled to a gain ring resonator by a 50:50 directional coupler. Even though we have shown the rich chaos control characteristics of lossy nonlinear single ring resonator systems in the previous section, we would now like to study the evolution of optical power in a double ring resonator system. Like before, we have modelled the system using the discrete time iterative equation known as the Ikeda Map.

This section is organized as follows. In section 4.3.1, we worked out the Ikeda Map of the double ring resonator system using the transfer matrix formalism. In section 4.3.2, we have evaluated the $\mathscr{PT}$ threshold in the linear regime and showed the dynamical behavior of the linear system in the unbroken $\mathscr{PT}$ regime, at the $\mathscr{PT}$ threshold and broken $\mathscr{PT}$ regime. Then, we discussed the effects that Kerr nonlinearity brings into the dynamical aspects of our system. Afterwards, we discussed the emergence of chaotic

Part of the results of this section have been published in the following papers: J. P. Deka and A. K. Sarma, "Chaotic dynamics and optical power saturation in parity–time (PT) symmetric double-ring resonator," Nonlinear Dynamics, https://doi.org/10.1007/s11071-019-04806-z (2019).

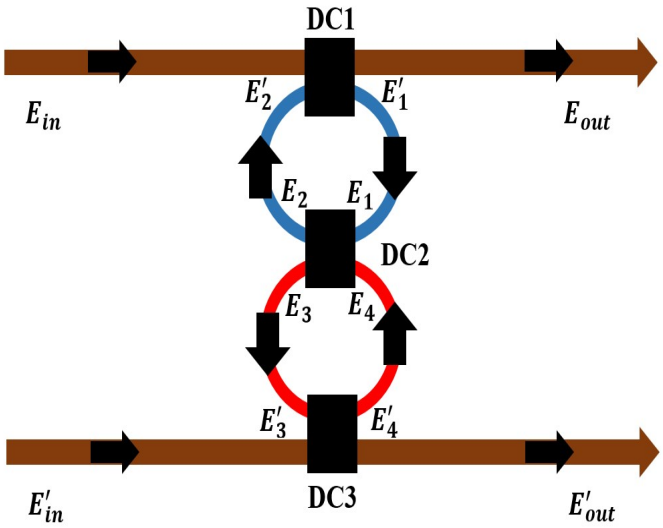

Figure 4.8: Schematic diagram of the double-ring resonator. The '**black colored block**' represents the 50:50 passive directional couplers (DC) and the '**brown colored region**' represents the optical fibers. The lossy resonator is colored '**blue**', while the amplifying resonator is colored '**red**'. E_{in} and $E_{in}^{'}$ are the input field amplitudes, and E_{out} and $E_{out}^{'}$ are the output field amplitudes. $E_1^{'}$ and $E_4^{'}$ are the output field amplitudes of coupler region DC1 and DC3, respectively. They are transferred via the resonators to the coupler region DC2 as E_1 and E_4. Similarly, E_2 and E_3 are the output field amplitudes of coupler region DC2. They are transferred, via the resonators, to the coupler region DC1 and DC3 as $E_2^{'}$ and $E_3^{'}$.

dynamics and chaotic spiking of optical power in the nonlinear regime. And finally, in section 4.3.3, we have concluded our work.

4.3.1 Theoretical Modelling

The model consists of three 50:50 directional couplers and two optical fiber based ring resonators with equal amount of gain and loss (schematic shown in Fig. 4.8). The two ring resonators exhibit Kerr nonlinearity of equal strength as well. Moreover, the directional couplers are passive medium. Now, as the field amplitude $E_1^{'}$ propagates through the lossy ring resonator from the output port of coupler region '**1**' to the input port of coupler region '**2**', it suffers loss as well as nonlinear phase shift. This could be then expressed in terms of the field amplitude E_1 as follows.

$$E_1 = e^{i(\phi_{NL,1}+\phi_L)} e^{-\gamma/2} E_1^{'} \tag{4.9}$$

where $\phi_{NL,1} = \beta|E_1|^2$ is the nonlinear phase shift imparted to the field as it propagates through the optical fiber of the ring resonators. In addition to this, the field amplitude

also suffers loss by a factor of $e^{-\gamma/2}$. Here, 'γ' is the gain/loss parameter, 'β' is the strength of the Kerr nonlinear phase shift and 'ϕ_L' is the linear phase shift. In addition, we know

$$E_1^{'} = \frac{iE_{in} + E_2^{'}}{\sqrt{2}} \tag{4.10}$$

where $E_2^{'} = e^{i(\beta e^{-\gamma}|E_2|^2 + \phi_L)} e^{-\gamma/2} E_2$. Using the transfer matrix of coupler region '**2**', E_2 and E_3 could be expressed in terms of E_1 and E_4 as follows.

$$\begin{pmatrix} E_2 \\ E_3 \end{pmatrix} = M \begin{pmatrix} E_1 \\ E_4 \end{pmatrix} \tag{4.11}$$

where M is the transfer matrix of the coupler region '**2**' and it is given by $M = \frac{1}{\sqrt{2}} \begin{pmatrix} 1 & i \\ i & 1 \end{pmatrix}$. Using Eq. (4.10) and (4.11) in Eq. (4.9), we have

$$E_1 = e^{i(\beta|E_1|^2 + \phi_L)} e^{-\gamma/2} \left(\frac{iE_{in}}{\sqrt{2}} + e^{i(\beta e^{-\gamma}|E_2|^2 + \phi_L)} e^{-\gamma/2} \frac{E_1 + iE_4}{2} \right) \tag{4.12}$$

Without loss of generality, we can set $\phi_L = 0$. To express Eq. (4.12) in the form of a discrete-time iterative equation, we need to declare the parameter 't_R' which characterizes the total time the electromagnetic field takes to complete one complete round trip across the resonator. Taking time steps equal to t_R, we can rewrite the evolution of field amplitude E_1 described by Eq. (4.12) in the form of an iterative equation as given below.

$$E_{1,j+1} = e^{i\beta|E_{1,j}|^2} e^{-\gamma/2} \left(\frac{iE_{in}}{\sqrt{2}} + e^{i\beta e^{-\gamma}|E_{2,j}|^2} e^{-\gamma/2} \frac{E_{1,j} + iE_{4,j}}{2} \right) \tag{4.13}$$

This equation relates the electric field amplitude E_1 in the $(j+1)$-th iteration with that in the j-th iteration. Similarly, we can express the field amplitude E_4 in the form of a discrete-time iterative equation as follows

$$E_{4,j+1} = e^{i\beta|E_{4,j}|^2} e^{\gamma/2} \left(\frac{iE_{in}^{'}}{\sqrt{2}} + e^{i\beta e^{\gamma}|E_{3,j}|^2} e^{\gamma/2} \frac{iE_{1,j} + E_{4,j}}{2} \right) \tag{4.14}$$

One important point that must be noted here is that the ring resonators are driven periodically by the field amplitudes E_{in} and $E_{in}^{'}$. The time period between each drive is the time taken by the field amplitudes to complete one round trip across the resonator t_R. Hence, we can say that the field amplitudes E_{in} and $E_2^{'}$ must reach the coupler region '**1**' at the same instance. Similarly, $E_{in}^{'}$ and $E_3^{'}$ must reach the coupler region '**3**' at the same instance.

4.3.2 Results and Discussion

4.3.2.1 Linear Regime ($\beta = 0$)

In the linear regime, we set $\beta = 0$ and Eq. (4.13) and (4.14) could be expressed as

$$E_{1,j+1} = e^{-\gamma/2}\left(\frac{iE_{in}}{\sqrt{2}} + e^{-\gamma/2}\frac{E_{1,j} + iE_{4,j}}{2}\right) \tag{4.15a}$$

$$E_{4,j+1} = e^{\gamma/2}\left(\frac{iE'_{in}}{\sqrt{2}} + e^{\gamma/2}\frac{iE_{1,j} + E_{4,j}}{2}\right) \tag{4.15b}$$

In matrix notation, Eq. (4.15a) and (4.15b) could be expressed as

$$\begin{pmatrix} E_{1,j+1} \\ E_{4,j+1} \end{pmatrix} = T\begin{pmatrix} E_{1,j} \\ E_{4,j} \end{pmatrix} + \frac{1}{\sqrt{2}}\begin{pmatrix} A_1 \\ A_2 \end{pmatrix} \tag{4.16}$$

where $T = \begin{pmatrix} e^{-\gamma}/2 & ie^{-\gamma}/2 \\ e^{\gamma}/2 & ie^{\gamma}/2 \end{pmatrix}$ is the transfer matrix. The driving terms are given by $A_1 = ie^{-\gamma/2}E_{in}$ and $A_2 = ie^{\gamma/2}E'_{in}$. To evaluate the $\mathscr{PT}$ threshold of the system, we solve for the eigenvalues of the matrix T and we find that the eigenvalues are given by $\lambda = \left(cosh(\gamma) \pm \sqrt{(cosh(\gamma))^2 - 2}\right)/2$ and the $\mathscr{PT}$ threshold is found to be $\gamma_{th} \approx 0.8814$.

On solving for the evolution of the optical power $P_1 = |E_1|^2$ and $P_4 = |E_4|^2$ using Eq. (4.16), we observe optical power saturation when $\gamma < \gamma_{th}$ and $\gamma = \gamma_{th}$. On the other hand, when $\gamma > \gamma_{th}$, we find that P_1 and P_4 increases at an exponential rate as the system evolves. These findings are presented in Fig. 4.9, wherein we observe that $P_4 > P_1$ for both below and above the $\mathscr{PT}$ threshold. This can be attributed to the fact that the field amplitude E_4 propagates in the amplifying resonator, whereas E_1 propagates in the lossy resonator.

A suitable discussion that explains the onset of optical power saturation in the linear regime could be given by constructing the hypersphere on whose surface lies the stable stationary states of Eq. (4.15a) and (4.15b). Existence of stationary states could be explained by measuring the radius of the hypersphere. This will lead us to an indirect inference for the cause of optical power saturation in the system. By separating the field amplitudes $E_{1,j}$ and $E_{4,j}$ in Eq. (4.15a) and (4.15b) into its real and imaginary

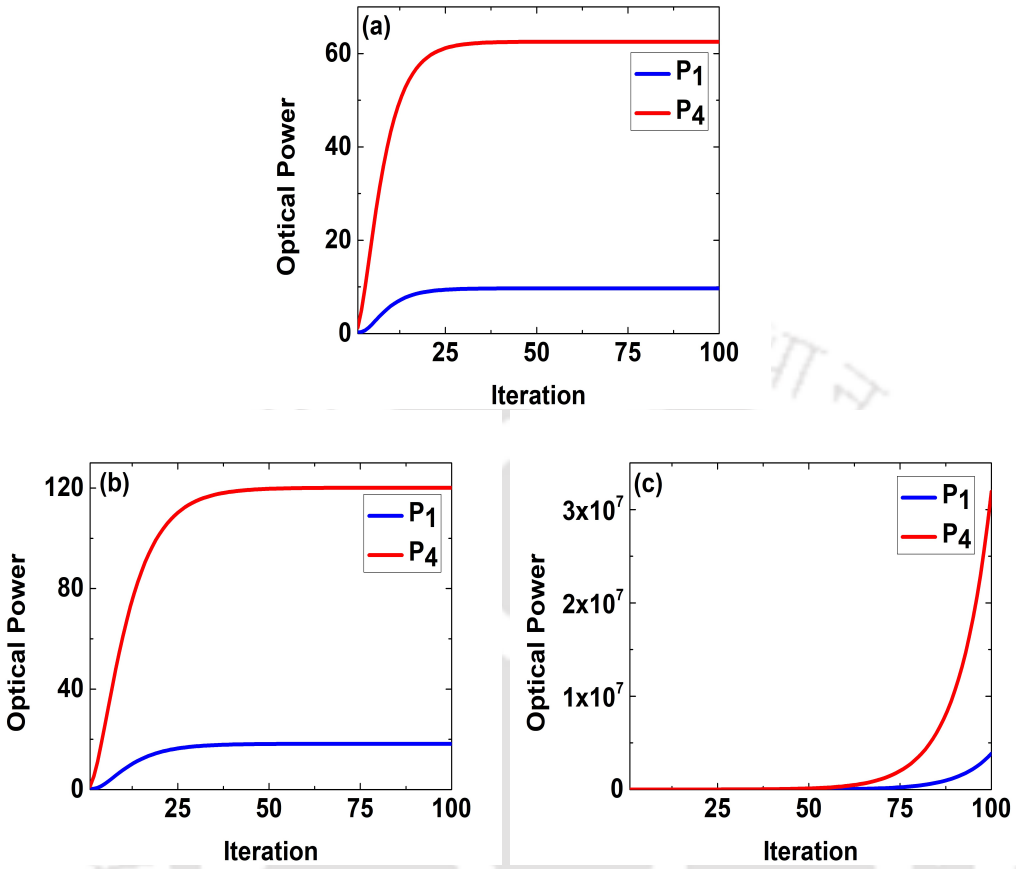

Figure 4.9: Temporal evolution of optical power in both resonators. The parameters chosen are (a) $\gamma = 0.85$ (Below $\mathscr{PT}$ Threshold) (b) (a) $\gamma = 0.8814$ (At $\mathscr{PT}$ Threshold) (c) $\gamma = 1$ (Above $\mathscr{PT}$ Threshold). The input field amplitudes are $E_{in} = 1$ and $E^{'}_{in} = 1$ in both cases.

components, we have

$$x_{1,j+1} = -A_1 y_{in} + B_1 \left(x_{1,j} - y_{4,j}\right) \tag{4.17a}$$

$$y_{1,j+1} = A_1 x_{in} + B_1 \left(x_{4,j} + y_{1,j}\right) \tag{4.17b}$$

$$x_{4,j+1} = -A_2 y^{'}_{in} + B_2 \left(x_{4,j} - y_{1,j}\right) \tag{4.17c}$$

$$y_{4,j+1} = A_2 x^{'}_{in} + B_2 \left(x_{1,j} + y_{4,j}\right) \tag{4.17d}$$

where $A_1 = e^{-\gamma/2}/\sqrt{2}$, $B_1 = e^{-\gamma}/2$, $A_2 = e^{\gamma/2}/\sqrt{2}$, $B_2 = e^{\gamma}/2$. $x_{i,j} = Re(E_{i,j})$, $y_{i,j} = Im(E_{i,j})$, $x_{in} = Re(E_{in})$, $y_{in} = Im(E_{in})$, $x^{'}_{in} = Re(E^{'}_{in})$ and $y^{'}_{in} = Im(E^{'}_{in})$ are the real and imaginary components of the field amplitudes. To evaluate the period-1 stationary states of Eq. (4.17a)-(4.17d), we need to set $x_{i,j+1} = x_{i,j}$ and $y_{i,j+1} = y_{i,j}$, where $i = 1, 4$. Mathematical simplification leads us to 4-dimensional hypersphere given as follows.

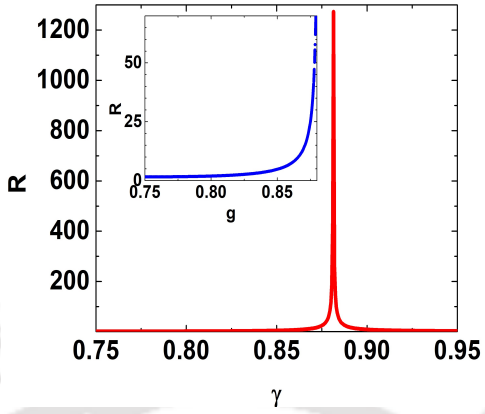

Figure 4.10: Radius of the Hypersphere R vs. Gain/Loss Coefficient γ.

$$(x_1+A_1C_1y_{in})^2+(y_1-A_1C_1x_{in})^2+(x_4+A_2C_2y_{in}^{'})^2+(y_4-A_2C_2x_{in}^{'})^2=A_1^2D_1P_{in}+A_2^2D_2P_{in}^{'} \tag{4.18}$$

Here, $C_1=(1-B_1)/((1-B_1)^2-B_2^2)$, $C_2=(1-B_2)/((1-B_2)^2-B_1^2)$, $D_1=B_2^2/((1-B_1)^2-B_2^2)$, $D_2=B_1^2/((1-B_2)^2-B_1^2)$. $P_{in}=x_{in}^2+y_{in}^2$ and $P_{in}^{'}=x_{in}^{'\,2}+y_{in}^{'\,2}$ are the input optical power. The radius of the hypersphere is given by $R=\sqrt{A_1^2D_1P_{in}+A_1^2D_2P_{in}^{'}}$. The hypersphere can exist only if R is of finite magnitude and a real quantity. The existence of the hypersphere would thereby prove why optical power saturation occurs below the $\mathscr{PT}$ threshold.

In Fig. 4.10, we can see that at $\gamma=\gamma_{th}$, R increases to very high magnitude and beyond the $\mathscr{PT}$ threshold, it decreases slowly. However, in the unbroken $\mathscr{PT}$ regime, it could be seen that the radius of the hypersphere is of finite magnitude. This means that the hypersphere exists only in the unbroken $\mathscr{PT}$ regime and as such, it validates our reasoning as to why power saturation occurs.

4.3.2.2 Nonlinear Regime ($\beta \neq 0$)

With the inclusion of Kerr nonlinearity, the optical power evolution dynamics will exhibit sensitiveness to initial conditions. In our system, the initial conditions are the excitation field amplitudes E_{in} and $E_{in}^{'}$. In Fig. 4.11, we have presented the parameter basin for period-1 cycle for three different cases of nonlinearity. In all cases, we have taken the excitation field amplitude $E_{in}^{'}$ as constant. The parameter basin consists of three regions - the convergent ('Blue' region), the non-convergent ('Red' region) and the divergent ('Black' region) region. In the convergent region, the optical power of the resonator

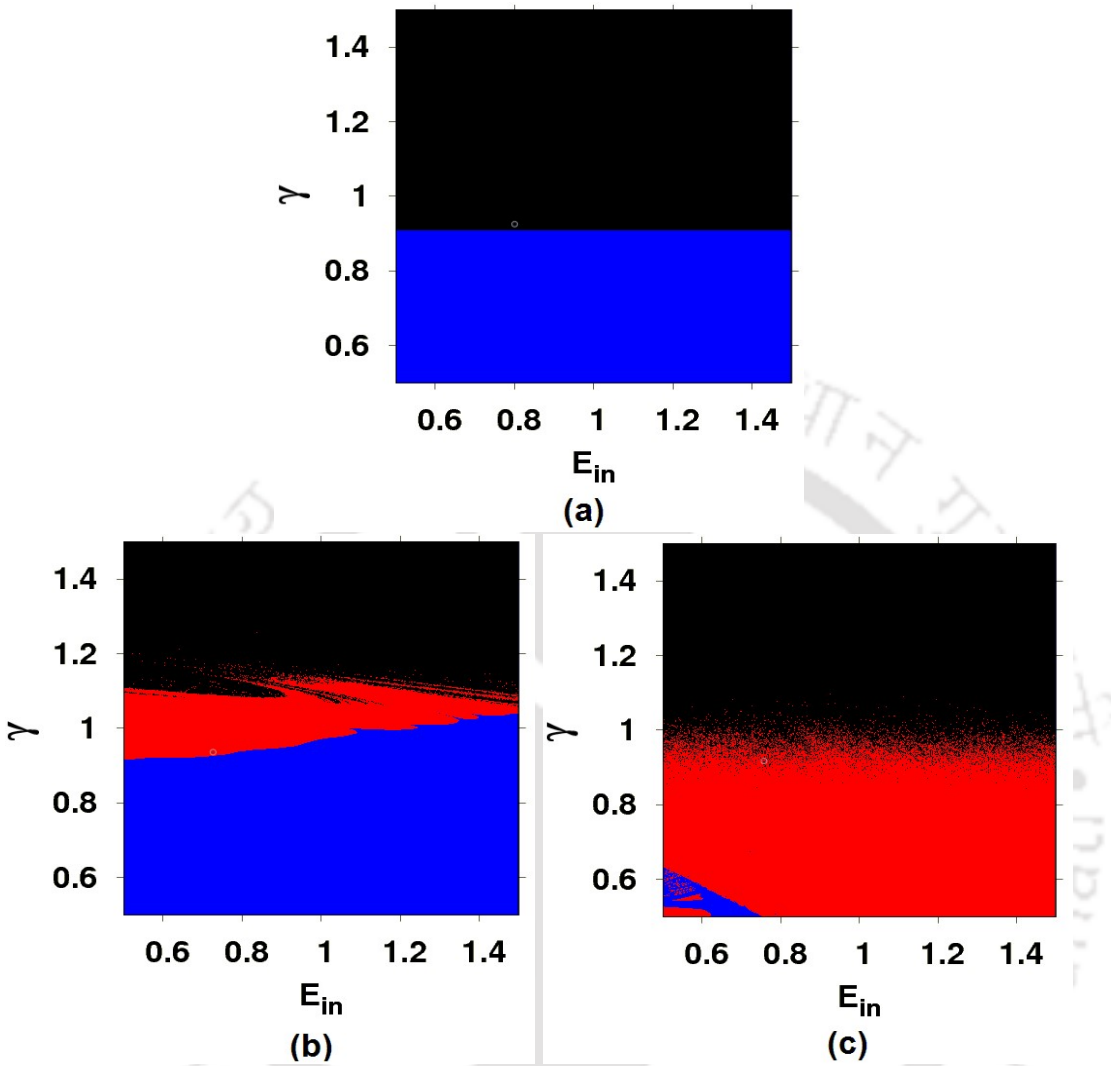

Figure 4.11: Parameter Basin for Period-1 Cycle when (a) $\beta = 0$ (Linear Regime) (b) $\beta = 0.01$ (Weakly Nonlinear) (c) $\beta = 1$ (Strongly Nonlinear). $E'_{in} = 1$ for all cases. The blue-colored region is the convergent region, i.e. the region where optical power saturation occurs. The red-colored region is the non-convergent region, signifying the presence of periodic as well as chaotic oscillations. And the black-colored region is the divergent region, and in this region, the optical power in both resonators diverges to infinity.

will eventually converge to a stable stationary state, i.e. optical power saturation will occur. On the other hand, in the non-convergent region, it will oscillate in a period-N cycles (where $N > 1$). However, in the divergent region, it will increase in an exponential manner. This means that the optical power in both resonators will blow up as the system evolves.

In the absence of nonlinearity (Fig. 4.11(a)), we can see that the convergent and divergent region are easily discernible and there is absence of non-convergent region.

This means that for $\beta = 0$, the system does not exhibit oscillatory behavior. However, this is not the case when we include nonlinearity into the system. In Fig. 4.11(b), we can see the emergence of non-convergent region in the parameter basin. This implies the existence of period-N cycles. In other words, it means that the optical power in both resonators will oscillate with every time-step. Moreover, when we consider the case of strong nonlinearity (Fig. 4.11(c)), the convergent region occupies a very small region in the parameter basin. One inference that we can have from this analysis is that stable stationary states cease to exist in the system as we increase the strength of nonlinearity. Nevertheless, optical power in both resonators will blow-up as we increase the gain/loss coefficient beyond the $\mathscr{PT}$ threshold irrespective of the strength of nonlinearity.

In the parameter basin for period-1 cycle, we saw that the convergent region substantially diminishes when β is increased. We would now like to present the bifurcation diagram of optical power $P_1 = |E_1|^2$ of the lossy resonator and largest Lyapunov exponent λ_{max} vs. γ to analyze into a specific case more deeply. We have chosen the case: $E_{in} = 1$, $E'_{in} = 1$ and $\beta = 1$. In Fig. 4.12(a), we can see that as we increase γ, evolution of P_1 shows period doubling route to chaos. This is evident in Fig. 4.12(b), where we can see λ_{max} increases from negative values to zero. As we increase γ, λ_{max} increases rapidly to very high positive values and beyond a certain critical point, it overflows. An overflowing λ_{max} implies that two infinitesimally close trajectories are infinitely separated as the system evolves. This occurs when γ is chosen in the neighborhood of $\gamma_{th} \approx 0.8814$. Exact calculation of this critical point is not possible. However, we can emphasize on the fact that inclusion of Kerr nonlinearity alters the $\mathscr{PT}$ threshold of the configuration in accordance with the excitation field amplitudes and above this phase transition point, λ_{max} overflows. Another point of interest that we would like to highlight is the significance of high positive Lyapunov exponent as we increase γ. From our evaluation of λ_{max}, we found that for $\gamma = 0.75$, $\lambda_{max} = 19.22$. This is an extremely large Lyapunov exponent. Usually, the order of Lyapunov exponents ranges near around zero. But it would be interesting to investigate the temporal evolution of optical power for $\gamma = 0.75$. The temporal evolution has been depicted in Fig. 13. It could seen that the optical power in both resonators spikes up to extremely large values in a chaotic fashion. In literature, such phenomena are termed as chaos spiking. It may be said here that in our $\mathscr{PT}$-Symmetric double ring resonator structure, we have quantified such phenomena using the largest Lyapunov exponent of the mathematical model.

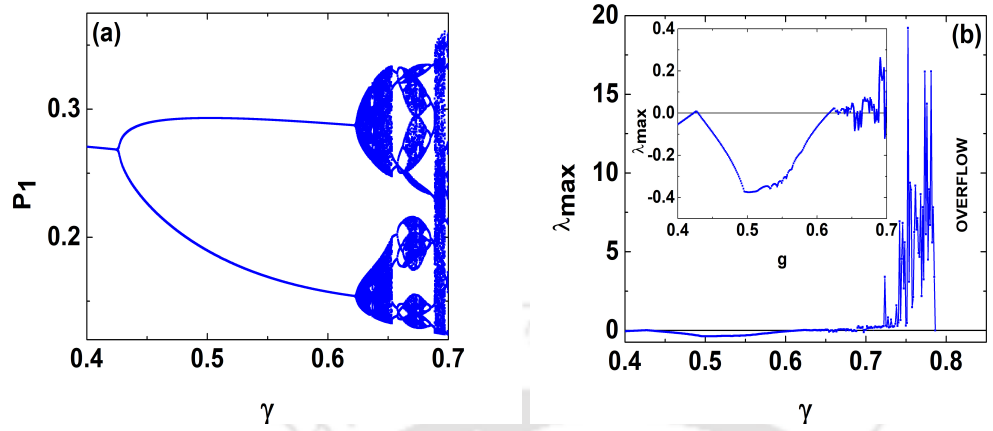

Figure 4.12: (a) Bifurcation Diagram and (b) Largest Lyapunov Exponent (λ_{max}) vs. Gain/Loss Coefficient (γ). The other parameters are $E_{in} = 1$, $E_{in}^{'} = 1$ and $\beta = 1$.

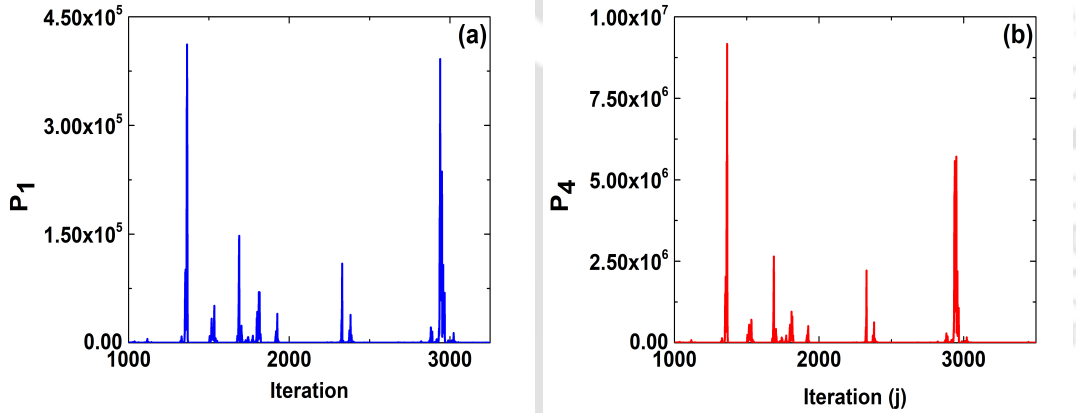

Figure 4.13: Temporal evolution of optical power in the two resonators when $\gamma = 0.75$. Other parameters: $E_{in} = 1$, $E_{in}^{'} = 1$ and $\beta = 1$.

4.3.3 Summary

Thus, in conclusion, we theoretically modelled the $\mathscr{PT}$-Symmetric double ring resonator using the discrete-time iterative equation known as Ikeda Map. In the absence of nonlinearity, we observed optical power saturation below the $\mathscr{PT}$ threshold and blow-up above the $\mathscr{PT}$ threshold. We found that optical power saturation occurs in the unbroken $\mathscr{PT}$ regime because of the existence of stable stationary states on the surface of 4D hypersphere. The hypersphere ceases to exist above the $\mathscr{PT}$ threshold. When we include Kerr nonlinearity into our model, we found the emergence of a non-convergent region in the period-1 parameter basin. The largest Lyapunov exponent in this region is a real

positive quantity, which implies the existence of chaos. Moreover, there exists a divergent region in the parameter basin above the $\mathscr{PT}$ threshold, where the largest Lyapunov exponent blows up. Furthermore, we observed that the existence of high non-negative largest Lyapunov exponent causes the chaotic spiking of optical power in our model.

CHAPTER 5

HIGHLY AMPLIFIED LIGHT TRANSMISSION IN $\mathscr{PT}$-SYMMETRIC MULTILAYERED STRUCTURE

5.1 Introduction

In this chapter, we report our study on a $\mathscr{PT}$-Symmetric multilayered structure that could facilitate highly amplified transmission in the infrared spectrum. In such structures, the transmission and reflection properties could be studied using the so-called the transfer matrix from the structure [88, 125-126]. The transfer matrix could be constructed from the boundary conditions of the incident fields on an interface between two layers. Such media are usually two-port devices and there has been interesting investigations on the optical properties of such structures. Z. Lin *et al.* reported unidirectional invisibility in a $\mathscr{PT}$-Symmetric Braggs grating structure [13]. They considered the refractive index profile of the structure to be $n(z) = n_0 + n_1 cos(2\beta z) + i n_2 sin(2\beta z)$, where n_0 is the refractive index, n_1 is the peak real component of the refractive index, n_2 is the peak gain/loss coefficient of the structure and β is the grating wave number. Using the S-matrix formalism, it was found that optical power, when launched from either of the two ports, showed entirely different behavior in the reflection and transmission properties of the structure. More recently, the transfer matrix formalism has been used

*Part of the results of this section have been published in the following papers: J. P. Deka and A. K. Sarma, "Highly amplified light transmission in parity-time symmetric multilayered structure", Applied Optics 57, 1119 (2018).

by M. Sarisaman to investigate unidirectional reflectionlessness and invisibility in a multilayered structure [17]. Moreover, it could be said that such phenomena in multilayered structures could be attributed to the scattering properties of the structure and these properties could be studied using the transfer matrix formalism.

In the same manner, we discuss how a multilayered structure with balanced gain and loss refractive index profile could facilitate highly amplified transmission of optical power in the infrared spectrum and at the same time, mathematically validate such properties of the structure. We have theoretically studied our model using the transfer matrix formalism. From the transfer matrix, the transmission and reflection of the structure are studied in the broken and unbroken $\mathscr{PT}$ regime. The theoretical results are then validated by FDTD numerical simulation. Afterwards, we have shown how spectral singularities in the S-matrix could be exploited to achieve amplified transmission of a single wavelength through the structure.

The chapter is organized as follows. In section 5.2, starting with the boundary conditions of the incident and reflected fields at the interfaces, the transfer matrix for the proposed structure is worked out [88]. The eigen-spectra of the transfer matrix is numerically evaluated followed by a study on the transmission and the reflection characteristics of the structure numerically as well as by using FDTD simulation in section 5.3. After that, it has been shown how modifying the length of the layers and its gain/loss coefficient could generate a spectral singularity in the S-matrix eigen spectrum and thereby impact the transmission of the radiation at $1550nm$, the so-called telecommunication wavelength.

5.2 Theoretical Modelling

We have considered a dielectric-nanofilm-dielectric multilayered (DND) structure (see schematic in Fig. 5.1). The dielectric layers are active media while the nanofilm is a passive medium. The length of the nanofilm is very small compared to the loss and the gain region. The structure is surrounded by vacuum on all sides. Considering normal incidence of the incoming fields and the x-axis as its propagation direction, boundary conditions at the input port, results:

$$A_i + B_i = A_1^{'} + B_1^{'} \tag{5.1a}$$

$$A_i - B_i = n_L \left(A_1^{'} - B_1^{'} \right) \tag{5.1b}$$

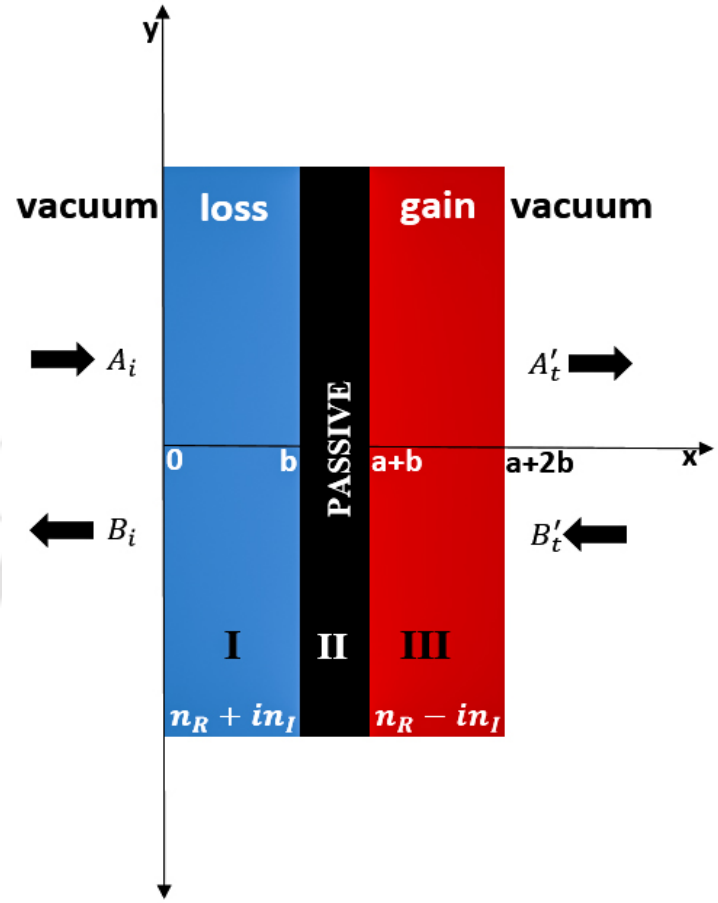

Figure 5.1: Schematic of the dielectric-nanofilm-dielectric multilayered structure. '**b**' is the length of the active regions (colored **red** and **blue**) and '**a**' is the length of the nanofilm region (colored **black**).

In matrix notation, these equations could be rewritten as follows.

$$\begin{pmatrix} 1 & 1 \\ 1 & -1 \end{pmatrix} \begin{pmatrix} A_i \\ B_i \end{pmatrix} = \begin{pmatrix} 1 & 1 \\ n_L & -n_L \end{pmatrix} \begin{pmatrix} A_1' \\ B_1' \end{pmatrix} \tag{5.2}$$

Or, we can write

$$\begin{pmatrix} A_i \\ B_i \end{pmatrix} = D_i^{-1} D_1 \begin{pmatrix} A_1' \\ B_1' \end{pmatrix} \tag{5.3}$$

where $D_i = \begin{pmatrix} 1 & 1 \\ 1 & -1 \end{pmatrix}$ and $D_1 = \begin{pmatrix} 1 & 1 \\ n_L & -n_L \end{pmatrix}$ are called the dynamical matrices of the launch medium and medium '**I**' respectively. n_L is the refractive index of medium '**I**', given by $n_L = n_R + in_I$. Now, as the wave propagates in medium '**I**', we have

$$\begin{pmatrix} A_1' \\ B_1' \end{pmatrix} \rightarrow P_1 \begin{pmatrix} A_1' \\ B_1' \end{pmatrix} = \begin{pmatrix} A_1 \\ B_1 \end{pmatrix} \tag{5.4}$$

where $P_1 = \begin{pmatrix} e^{ik_1 b} & 0 \\ 0 & e^{-ik_1 b} \end{pmatrix}$ is called the propagation matrix and it describes the phase accumulated by the backward and forward propagating wave in medium '**I**' as it traverses the whole length of the medium. $k_1 = n_L \omega/c$ is the wavenumber in medium '**I**'. Hence, we have

$$\begin{pmatrix} A_i \\ B_i \end{pmatrix} = D_i^{-1} D_1 P_1^{-1} \begin{pmatrix} A_1 \\ B_1 \end{pmatrix} \tag{5.5}$$

Similarly, we can write the dynamical and propagation matrices for the other interfaces as follows.

$$\begin{pmatrix} A_1 \\ B_1 \end{pmatrix} = D_1^{-1} D_2 P_2^{-1} \begin{pmatrix} A_2 \\ B_2 \end{pmatrix} \tag{5.6}$$

$$\begin{pmatrix} A_2 \\ B_2 \end{pmatrix} = D_2^{-1} D_3 P_3^{-1} \begin{pmatrix} A_3 \\ B_3 \end{pmatrix} \tag{5.7}$$

$$\begin{pmatrix} A_3 \\ B_3 \end{pmatrix} = D_3^{-1} D_i \begin{pmatrix} A_t' \\ B_t' \end{pmatrix} \tag{5.8}$$

Using Eq. (5.6)-(5.8) in Eq. (5.5), we have

$$\begin{pmatrix} A_i \\ B_i \end{pmatrix} = D_i^{-1} D_1 P_1^{-1} D_1^{-1} D_2 P_2^{-1} D_2^{-1} D_3 P_3^{-1} D_3^{-1} D_i \begin{pmatrix} A_t' \\ B_t' \end{pmatrix} \tag{5.9}$$

which could be rewritten as follows.

$$\begin{pmatrix} A_t' \\ B_t' \end{pmatrix} = T \begin{pmatrix} A_i \\ B_i \end{pmatrix} \tag{5.10}$$

where $T = D_i^{-1} D_3 P_3 D_3^{-1} D_2 P_2 D_2^{-1} D_1 P_1 D_1^{-1} D_i$ is the transfer matrix of the structure. Here, $D_2 = \begin{pmatrix} 1 & 1 \\ n_{film} & -n_{film} \end{pmatrix}$ and $D_3 = \begin{pmatrix} 1 & 1 \\ n_G & -n_G \end{pmatrix}$ are the dynamical matrices of the nanofilm (medium '**II**') and the gain layer (medium '**III**') respectively. n_{film} and n_G are the refractive indices of medium '**II**' and medium '**III**' respectively, with $n_{film} = n_{R,film} + i n_{I,film}$ and $n_G = n_R - i n_I$. On the other hand, $P_2 = \begin{pmatrix} e^{ik_2 a} & 0 \\ 0 & e^{-ik_2 a} \end{pmatrix}$ and $P_3 = \begin{pmatrix} e^{ik_3 b} & 0 \\ 0 & e^{-ik_3 b} \end{pmatrix}$ are the propagation matrices of medium '**II**' and '**III**' respectively. Here, $k_2 = n_{film}\omega/c$ and $k_3 = n_G \omega/c$ are the corresponding wave numbers. Finally, the transfer matrix of the structure could be expressed as follows.

$$T = \frac{T_3 T_2 T_1 T_0}{16} \tag{5.11}$$

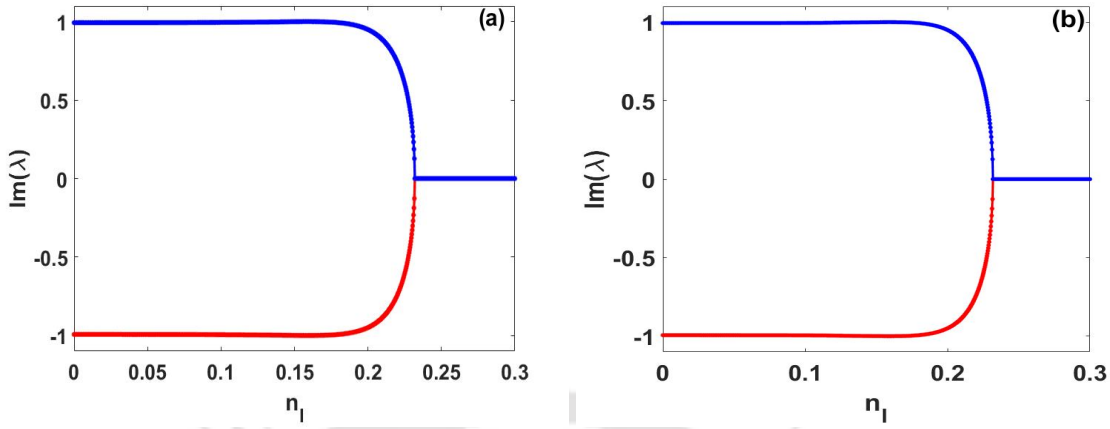

Figure 5.2: Eigen-spectra of the transfer matrix for excitation of (a) loss port and (b) gain port.

where $T_3 = \begin{pmatrix} 1+n_G & 1-n_G \\ 1-n_G & 1+n_G \end{pmatrix}$, $T_2 = \begin{pmatrix} e^{ik_3 b}(1+n/n_G) & e^{ik_3 b}(1-n/n_G) \\ e^{-ik_3 b}(1-n/n_G) & e^{-ik_3 b}(1+n/n_G) \end{pmatrix}$,

$T_1 = \begin{pmatrix} e^{ik_{2a}}(1+n_L/n) & e^{ik_{2a}}(1-n_L/n) \\ e^{-ik_{2a}}(1-n_L/n) & e^{-ik_{2a}}(1+n_L/n) \end{pmatrix}$ and $T_0 = \begin{pmatrix} e^{ik_1 b}(1+1/n_L) & e^{ik_1 b}(1-1/n_L) \\ e^{-ik_1 b}(1-1/n_L) & e^{-ik_1 b}(1+1/n_L) \end{pmatrix}$.

5.3 Results and Discussion

Analytical calculations for the eigenvalues and their corresponding eigenvectors of the transfer matrix T are a rather tedious job. That is why we have numerically evaluated the eigen-spectra of the transfer matrix. We consider the dielectric of the structure to be made of silica ($n_R = 1.4657$) while the nanofilm to be made of sapphire ($n_{film} = 1.7462$). The sapphire nanofilm is considered to be a passive medium. This means $n_{I,film} = 0$. The dielectrics on the two sides of the nanofilm are doped to have equal amount of loss and gain respectively. The length, b, of the silica layers is assumed to be $2.49\mu m$ and that of the nanofilm is, $a = 0.02\mu m$. Fig. 5.2 depicts the eigen-spectra of the structure when it is excited from (a) the loss-port and (b) the gain-port, with a radiation centered at the wavelength $1550nm$.

From Fig. 5.2, we observe that as n_I is increased, the imaginary component of the transfer matrix eigenvalues ceases to be imaginary beyond the $\mathscr{PT}$ threshold. Moreover, the eigen-spectra do not depend on whether optical power is launched from the loss port or the gain port. For our chosen system parameters, the $\mathscr{PT}$ threshold is found to be at $n_I \approx 0.23$.

The transmission and reflection coefficients of the S-matrix could be obtained from the

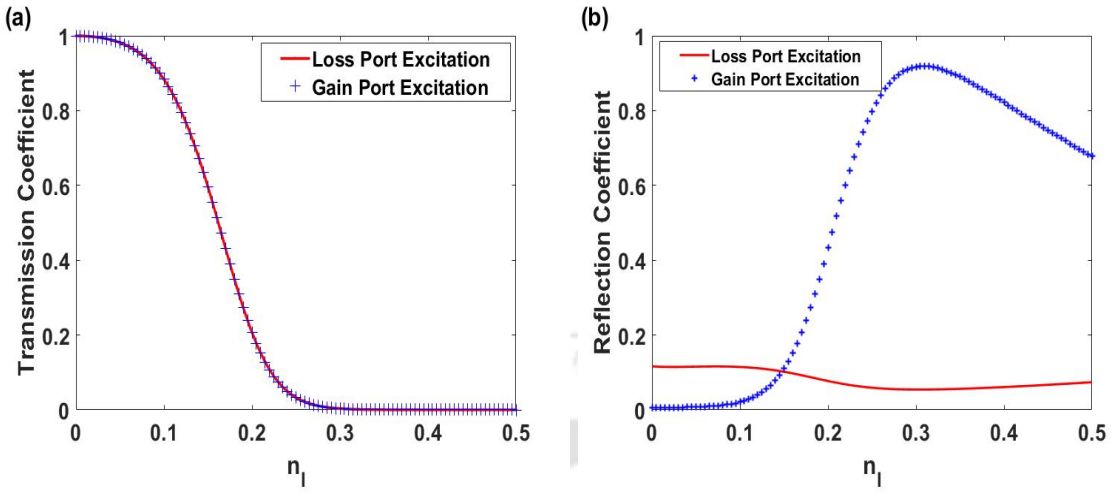

Figure 5.3: (a) Transmission Coefficient ($T^{'}$) and (b) Reflection Coefficient ($R^{'}$) vs. Gain/Loss Coefficient n_I for excitation of loss or gain port.

elements of the transfer matrix T_{ij}. The transmission coefficient is given by $T^{'} = |1/T_{22}|^2$ and the reflection coefficient by $R^{'} = |-T_{21}/T_{22}|^2$ [89]. The normalized transmission and the reflection coefficients as a function of the loss/gain parameters, for both loss and gain port excitation, are plotted in Fig. 5.3(a) and 5.3(b) respectively. The transmission characteristics of the DND structure, as depicted in Fig. 5.3(a), are found to be independent of the launch conditions. There is near complete transmission when one operates below the $\mathscr{PT}$ threshold, while above the $\mathscr{PT}$ threshold, the transmission coefficient decreases exponentially to zero. On the other hand, as shown in Fig. 5.3(b), the reflection characteristics exhibit significantly different behavior. If operated above the $\mathscr{PT}$-threshold, and the radiation is launched from the gain port, the reflection coefficient increases to very high values, implying significant reflection (Fig. 5.3(b)). This is supported by very low value of the transmission coefficient as well. In Fig. 5.4, we have shown how our structure is superior in comparison to a gain-nanofilm-gain structure. We can see that for a gain-nanofilm-gain structure, the transmission coefficient rises sharply initially as we increase n_I. But then it decreases to zero, whereas the transmission coefficient of our structure remains high in the unbroken $\mathscr{PT}$ regime. Only above the $\mathscr{PT}$ threshold, it decays to zero.

FDTD simulations validate these theoretical results. Fig. 5.5 and 5.6 depicts, for below and above the $\mathscr{PT}$ threshold regime respectively, the contour plot for time-averaged power propagation in the DND structure. P_I , P_R and P_O are, respectively, the input, the reflected and the output optical power. In order to understand these plots, it is important

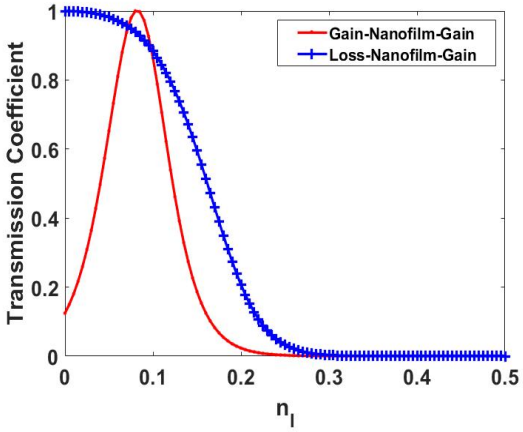

Figure 5.4: Transmission Coefficient ($T^{'}$) vs. Gain/Loss Coefficient n_I.

to note the followings about the color bar. The positive (negative) values in the color bar signify that the optical power is propagating in the positive (negative) x-direction. The plots clearly illustrate the dependence on the initial launch condition of the optical radiation and the $\mathscr{PT}$ threshold. If one operates below the $\mathscr{PT}$ threshold, as shown in Fig. 5.5, near complete transmission of optical radiation could be observed. However, the nature of evolution of optical power is different for both the launch conditions. The structure, as depicted in Fig. 5.6, exhibits completely different behavior if one operates above the $\mathscr{PT}$ threshold. It is possible to achieve near complete transmission when the radiation is launched from the loss port while almost complete reflection of optical radiation is obtained when the structure is excited from the gain port.

Now, we show how, with judicious choice of the structure parameters, it is possible to engineer the spectral singularity of the S-matrix and thereby, achieve amplified transmission at the desired wavelength regime. For our calculations, we have assumed the following parameters: $a = 0.4\mu m$, $b = 2.3\mu m$ and $\lambda_0 = 1550nm$. The structure is excited from the loss port only. Fig. 5.7(a) plots the eigen-spectra of the transfer matrix as a function of the loss/gain parameter n_I. We find that, in the region $n_I = 0.18 - 0.19$, the imaginary component of the eigenvalues flips its sign. We mean to say that the negative imaginary component of the eigenvalues becomes positive and vice-versa. At the same time, in Fig. 5.7(b), we can see that the transmission coefficient of the structure shows a sharp peak in the same region. The reason for this can be found in Fig. 5.8(a), wherein we see that the eigen-spectra of the S-matrix show a sharp dip. This is referred to as a spectral singularity of the S-matrix [90]. Now, if we choose $n_I \approx 0.18$, we obtain highly amplified transmitted radiation at $1550nm$, as illustrated in Fig. 5.8(b). The entire IR

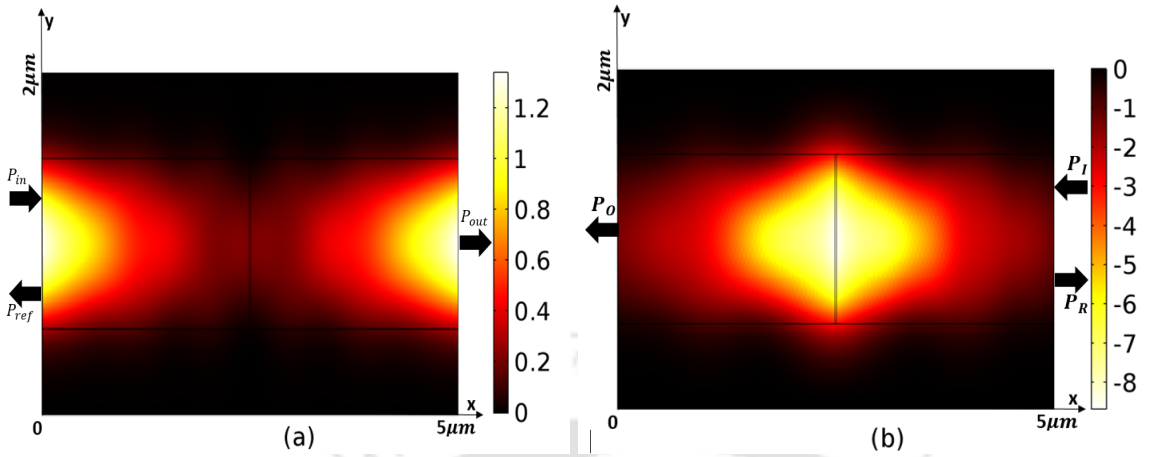

Figure 5.5: Contour plot of 'Time-averaged power flow (in the unit of $10^6 W/m^2$)' for initial excitation of (a) loss port and (b) gain port when $n_I = 0.1$ (below $\mathscr{PT}$ threshold).

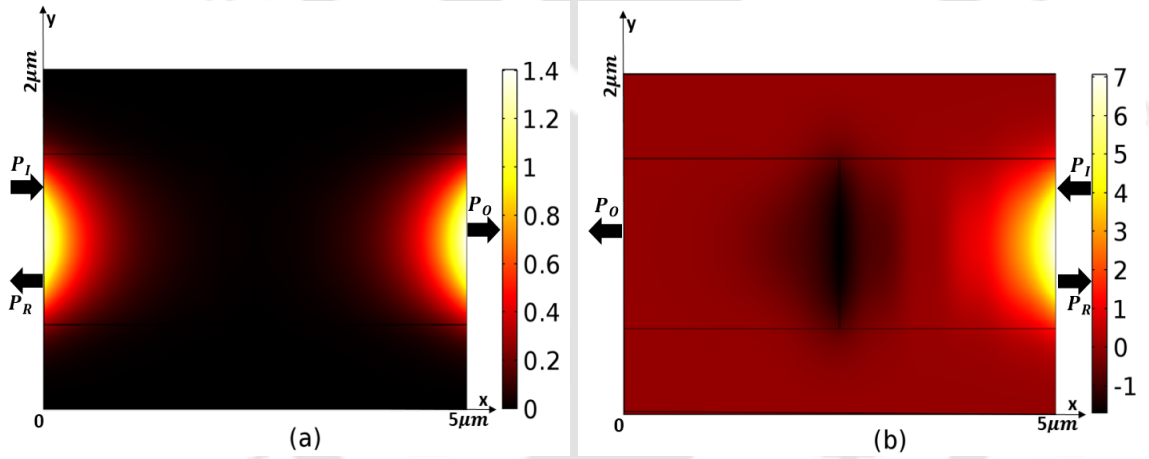

Figure 5.6: Contour plot of 'Time-averaged power flow (in the unit of $10^6 W/m^2$)' for initial excitation of (a) loss port and (b) gain port when $n_I = 0.25$ (below $\mathscr{PT}$ threshold).

spectrum is blocked except the at $1550nm$ wavelength. Thus, we infer that the proposed structure could indeed be used as an IR filter.

To confirm this inference further, we check the transmittance of the structure at the following wavelengths: red ($\lambda_0 = 650nm$), blue ($\lambda_0 = 475nm$) and green ($\lambda_0 = 550nm$) as a function of the gain/loss coefficient , n_I. We observe, as illustrated in Fig. 5.9, that the transmissivity vanishes for all these wavelengths as $n_I \to 0.18$. This clearly indicates that, only the wavelength, for which we observe spectral singularity in the S-matrix eigen-spectra, will be transmitted.

Another interesting feature that we observed from our calculations is the existence of multiple $\mathscr{PT}$ thresholds. We have chosen the following parameter: $a = 0.6\mu m$, $b = 2.2\mu m$

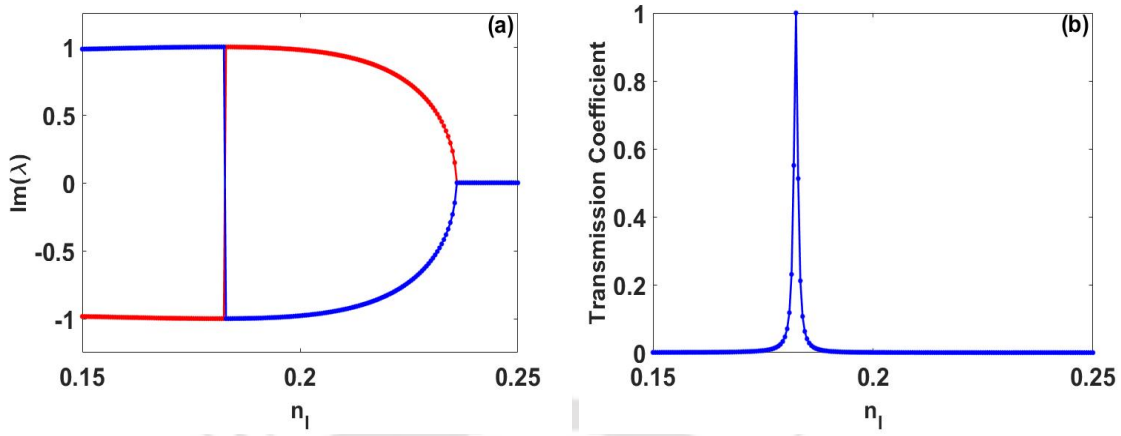

Figure 5.7: (a) Eigen spectra of the transfer matrix ($\lambda_0 = 1550nm$) (b) Transmission Coefficient ($T^{'}$) vs. Gain/Loss Coefficient n_I.

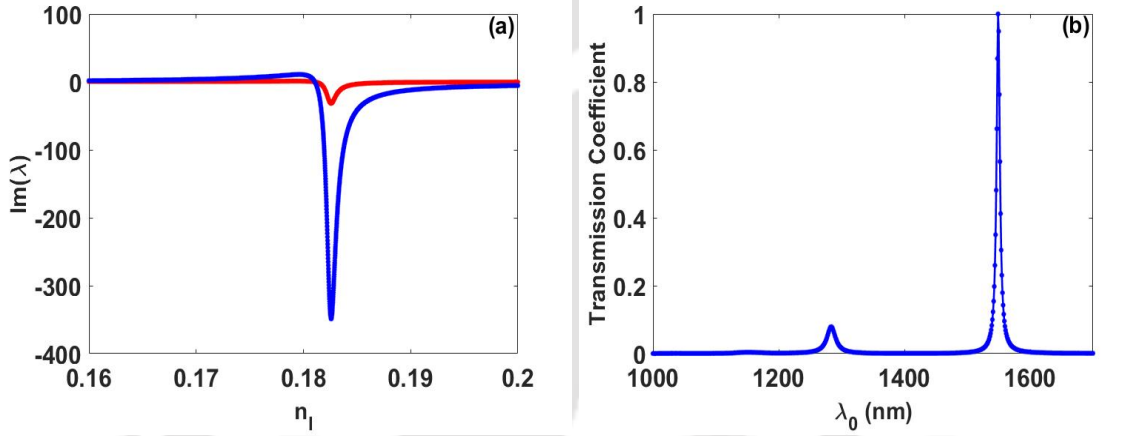

Figure 5.8: (a) Imaginary component of the eigen spectra of the S-matrix ($\lambda_0 = 1550nm$) (b) Transmission Coefficient ($T^{'}$) vs. Wavelength ($n_I = 0.18$).

and $\lambda_0 = 1550nm$. For our choice of parameter values, we find (from Fig. 5.10(a)) that the eigen-spectra consists of three $\mathscr{PT}$ thresholds, viz. $n_I \approx 0.247, 0.4095, 0.4280$. On top of that, we can see that the imaginary component of the eigenvalues flips its sign in the region $n_I = 0.41 - 0.43$. One important inference that we can draw from this is that the length of the nanofilm and the silica layers plays a major role in the existence of the $\mathscr{PT}$ threshold and also in the generation of spectral singularity of the S-matrix (as seen in Fig. 5.8(a)). To further validate our inference, we have shown in Fig. 5.10(b) the transmission coefficient vs. n_I followed by the resonance spectrum in Fig. 5.11.

Our findings have confirmed the fact that our structure could indeed be utilized for perfect transmission of the $1550nm$ wavelength. It could be seen from our results

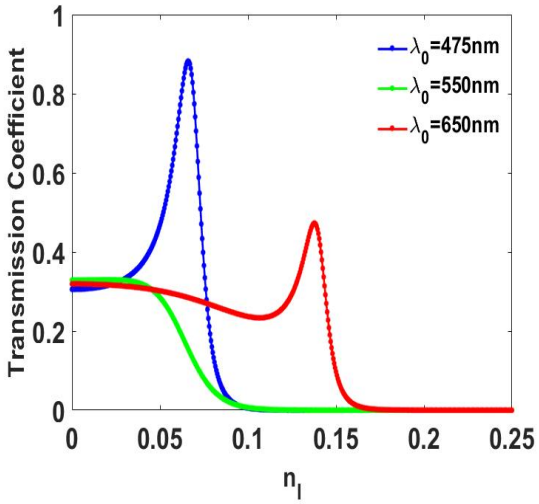

Figure 5.9: Transmission coefficient ($T^{'}$) vs. n_I for red, blue and green wavelength.

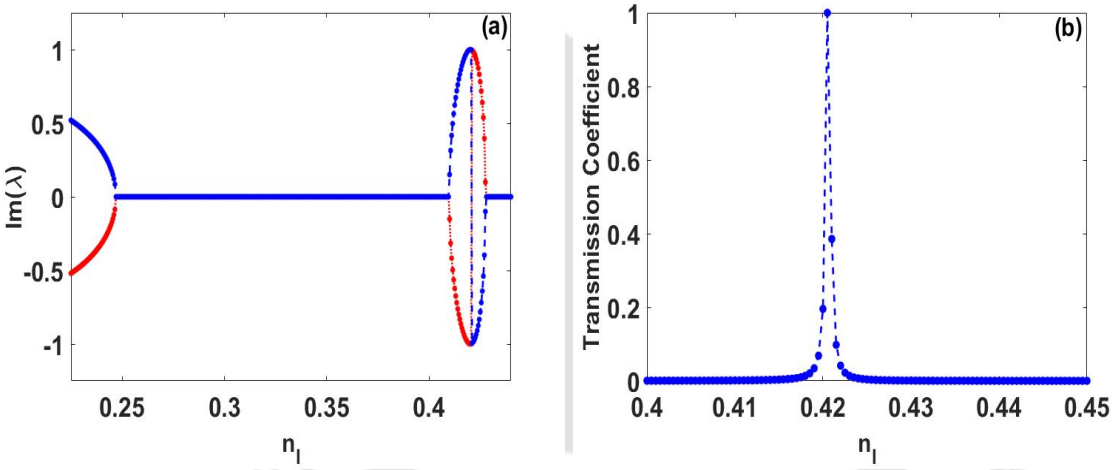

Figure 5.10: (a) Eigen spectra of the transfer matrix ($\lambda_0 = 1550nm$) (b) Transmission Coefficient ($T^{'}$) vs. Gain/Loss Coefficient n_I.

that spectral singularities could be generated in the eigen spectra of the S-matrix with judicious choice of parameters. Furthermore, it has been found that such spectral singularities could facilitate highly amplified transmission for the said wavelength. In our analysis, we paid attention to the $1550nm$ wavelength, for its role in the telecommunication sector. But nevertheless, our analysis has provided with reasons to claim that with judicious choice of parameters, generation of spectral singularities and thereby highly amplified transmission of light could indeed be a possibility in such a multilayered structure for other wavelengths.

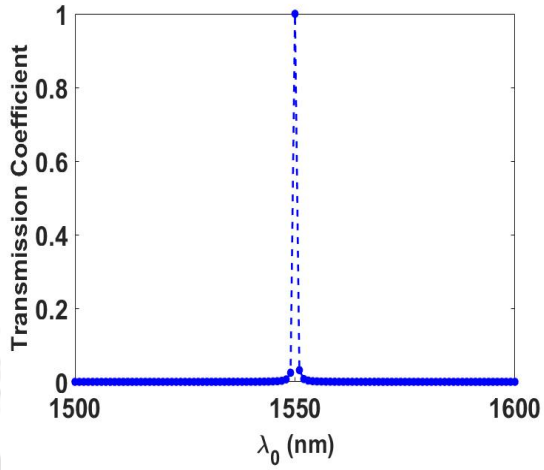

Figure 5.11: Transmission Coefficient ($T^{'}$) v/s Wavelength ($n_I = 0.42$).

5.4 Summary

In conclusion, we propose a $\mathscr{PT}$-Symmetric dielectric-nanofilm-dielectric multilayered structure that could facilitate highly amplified transmission of optical power in the infrared spectrum. The analysis is carried out assuming the dielectric to be made of silica while the nanofilm of sapphire. We have theoretically studied our model using the transfer matrix formalism. The theoretical results are validated by FDTD numerical simulation. Further, we show that, with judicious choice of the structure parameters, such as: length of the dielectric and the film layer and loss-gain parameters, it is possible to achieve highly amplified single wavelength transmission. The proposed structure may be useful for various applications in various light-based photonic and optoelectronics devices.

CHAPTER 6

BLOW-UP AND CHAOTIC DYNAMICS IN $\mathscr{PT}$-SYMMETRIC LIÉNARD SYSTEMS

6.1 Introduction

In this chapter, we concentrate on the analysis of $\mathscr{PT}$-Symmetric Liénard oscillators. It must be noted that Liénard type oscillators/systems are prototype models to study the dynamics of oscillators with nonlinear dissipation in many areas of physics, biology, electronics and so on [91]. The nonlinear damping term in Liénard systems can serve as both damping or amplification term resulting in self-sustained oscillations. These systems comprise of the Van der Pol oscillator, the FitzHugh-Nagumo oscillator, etc. The Van der Pol oscillator [92-93] gives rise to stable limit cycles based on certain parametric choices and those oscillations are further coined as relaxation-oscillation. In fact, the Van der Pol oscillator had also been used to model biological regulatory systems such as the cardiac and respiratory systems [94,95]. Similarly, the FitzHugh-Nagumo oscillator [96-98] (which is reducible to the Van der Pol oscillator) is another class of Liénard systems and it has been used to model nerve impulses. It has also been shown recently that the forced Liénard system could be utilized to generate extreme events [99]. On the other hand, it has been recently shown experimentally that nonlinear damping could enhance the quality factor of graphene oscillators significantly [100]. Moreover, for free falling objects in earth's gravity, the viscous force acting on the object is directly

proportional to the square of the velocity and this force leads to the terminal velocity in such objects. Hence, it could be said that nonlinear dissipation plays an interesting role in the dynamics of numerous systems.

In this chapter, we propose a coupled Liénard oscillator configuration with balanced loss and gain profile. Given the importance of such oscillators as discussed above, we pay attention on the $\mathscr{PT}$-Symmetric counterpart of such systems. A linear $\mathscr{PT}$-Symmetric oscillator is a coupled oscillator configuration in which one oscillator linearly attenuates the perturbation applied to it and the other oscillator linearly amplifies the perturbation by the same proportion [43]. On the other hand, in a $\mathscr{PT}$-Symmetric system with nonlinear dissipation, it must be ensured via the operation of the $\mathscr{PT}$ operator that the system is $\mathscr{PT}$-Symmetric. We have considered two cases by means of the order of nonlinear dissipation. The stability of the stationary states using the linearization Jacobian method is also discussed followed by our analysis of the dynamics of the system in the neutrally stable region.

The chapter is organized as follows. In section 6.2, we discuss our model starting from the basics of $\mathscr{PT}$-Symmetry in harmonic oscillator models and analytically evaluate the stationary states of the system. Section 6.3 has been divided into two subsections for the two configurations of the $\mathscr{PT}$-Symmetric oscillator that we are concentrating on in this chapter. In the first configuration, we study the stability of the stationary states under variations in gain/loss coefficient. Further, we analyze the temporal evolution of the system when it is subjected to different initial conditions. After that, we show how the usage of an external drive could be employed to achieve controllability over blow-up dynamics in our model. In the second configuration, we show how the temporal dynamics of the system in the neutrally stable regime of the Jacobian gives rise to the quasiperiodic route to chaos, which we have further validated from power spectral analysis. In Sec. 6.4, we propose an electronic circuit that could facilitate the experimental realization of our theoretical observations. We summarize our results along with an outlook in section 6.5.

6.2 Mathematical Model

To start with, consider the generalized coupled nonlinear $\mathscr{PT}$-Symmetric harmonic oscillator model given below.

$$\frac{d^2x_1}{dt^2} + \left(\gamma + \eta x_1^{\delta}\right)\frac{dx_1}{dt} + \beta x_1^3 + \omega_0^2 x_1 + \kappa x_2 = f(t) \tag{6.1a}$$

$$\frac{d^2x_2}{dt^2} - \left(\gamma + \eta x_2^{\delta}\right)\frac{dx_2}{dt} + \beta x_2^3 + \omega_0^2 x_2 + \kappa x_1 = 0 \tag{6.1b}$$

where γ is linear gain/loss coefficient, η is the strength of nonlinear damping/gain, δ is the exponent of nonlinear damping/gain, κ is the coupling coefficient, β is the coefficient of Duffing nonlinearity and $f(t)$ is the external drive. And all of them are positive real quantities. In such coupled oscillator configurations, the $\mathscr{PT}$ operator is defined as: $x_1 \to x_2$, $x_2 \to x_1$ and $t \to -t$. From a physical perspective, it could be said that the two oscillators are interchanged under the operation of the parity operator and the time reversal operator interchanges the role played by the two oscillator in the model, i.e. the attenuated oscillator becomes an amplified oscillator and vice-versa. In addition to this, the external drive $f(t)$ must be an even function of time t. In a nutshell, the entire configuration remains invariant under the joint operation of the $\mathscr{PT}$ operator. Taking $\dot{x_i} = y_i$, Eq. (6.1a) and Eq. (6.1b) could be shown to transform as follows.

$$\frac{dx_1}{dt} = y_1 \tag{6.2a}$$

$$\frac{dy_1}{dt} = -\left(\gamma + \eta x_1^{\delta}\right)y_1 - \beta x_1^3 - \omega_0^2 x_1 - \kappa x_2 + f(t) \tag{6.2b}$$

$$\frac{dx_2}{dt} = y_2 \tag{6.2c}$$

$$\frac{d^2x_2}{dt^2} = \left(\gamma + \eta x_2^{\delta}\right)y_2 - \beta x_2^3 - \omega_0^2 x_2 - \kappa x_1 \tag{6.2d}$$

This system with no external force ($f(t) = 0$) admits the following stationary states:

1. The trivial fixed point $(x_1, y_1, x_2, y_2) = (0, 0, 0, 0)$,
2. The non-zero fixed point $(x_1, y_1, x_2, y_2) = (\pm a_1, 0, \mp a_1, 0)$ and
3. The non-zero fixed point $(x_1, y_1, x_2, y_2) = (\pm a_2, 0, \mp a_2, 0)$,

where $a_1 = \sqrt{(\kappa - \omega_0^2)/\beta}$ and $a_2 = \sqrt{(-\kappa - \omega_0^2)/\beta}$. In the next section, we will discuss the stability analysis of the fixed point $(x_1, y_1, x_2, y_2) = (0, 0, 0, 0)$ (**FP1**), $(x_1, y_1, x_2, y_2) = (a_1, 0, -a_1, 0)$ (**FP2**) and $(x_1, y_1, x_2, y_2) = (-a_1, 0, a_1, 0)$ (**FP3**).

6.3 Results and Discussion

The linearization Jacobian of our system with $f(t) = 0$ is given by

$$J = \begin{pmatrix} 0 & 1 & 0 & 0 \\ A & B & -\kappa & 0 \\ 0 & 0 & 0 & 1 \\ -\kappa & 0 & C & D \end{pmatrix} \tag{6.3}$$

where $A = -\omega_0^2 - 3\beta x_1^2 - \delta\eta x_1^{(\delta-1)} y_1$, $B = -\gamma - \eta x_1^{\delta}$, $C = -\omega_0^2 - 3\beta x_2^2 + \delta\eta x_2^{(\delta-1)} y_2$ and $D = \gamma + \eta x_2^{\delta}$. In the following, in order to have a clear exposition, we discuss the nonlinear dynamics of system due to the nonlinear position dependent damping/gain for $\delta = 1$ and $\delta = 2$ respectively, along with the presence of other effects, in two different subsections.

6.3.1 Case I: $\delta = 1$

First, we analyze the eigen spectra of the linearization Jacobian given in Eq. (6.3) for $\delta = 1$. We have plotted the real components of all the four eigenvalues of the Jacobian in Fig. 6.1 for **FP1**, **FP2** and **FP3**. From the spectral analysis, it could be seen that the trivial stationary state is an unstable saddle for all values of γ (Fig. 6.1(a)). On the other hand, a very close look at the eigen spectra for the fixed points **FP2** and **FP3** tells us that the fixed point **FP2** is an attractor (Fig. 6.1(b)) and the fixed point **FP3** is a repeller (Fig. 6.1(c)) for very low values of γ. So, this means that for certain parametric choices, our system has a stable, an unstable and a saddle fixed point.

We would now discuss the temporal dynamics of the two oscillator when it is subjected to an initial excitation. For our analysis, we have considered the gain/loss coefficient as $\gamma = 0.4$. The real component of the Jacobian eigenvalues for **FP2** are $Re(\lambda_1) = Re(\lambda_2) = -0.018$ and $Re(\lambda_3) = Re(\lambda_4) = -0.031$ and that for **FP3** are $Re(\lambda_1) = Re(\lambda_2) = 0.018$ and $Re(\lambda_3) = Re(\lambda_4) = 0.031$. So, when the system is given an initial excitation $(x_1(0) = y_1(0) = 0, x_2(0) = 0.1, y_2(0) = 0)$, it could be seen that the temporal evolution instantaneously approaches the stable fixed point (**FP2**) (Fig. 6.2). But when the initial condition has been increased to $(x_1(0) = y_1(0) = 0, x_2(0) = 0.5, y_2(0) = 0)$, we observe the emergence of blow-up dynamics in the two oscillators (Fig. 6.3). The gain oscillator exponentially increases to extremely high values (Fig. 6.3). This could be attributed to the fact that the fixed point **FP2** is not a globally stable fixed point. Moreover, it could be seen that the initial conditions correspond to the excitation of the gain oscillator. So,

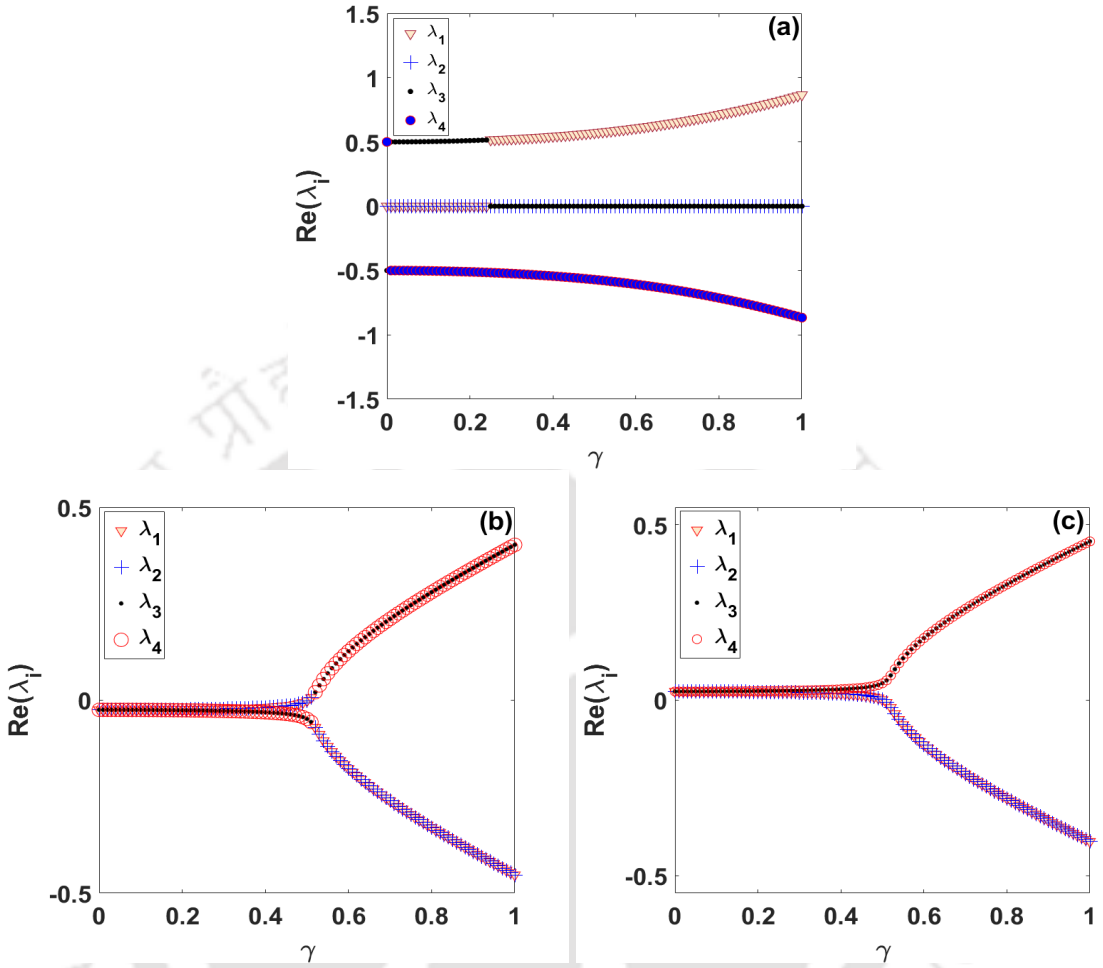

Figure 6.1: Real component of the Jacobian eigenvalues of the $\mathscr{PT}$-Symmetric Liénard oscillator for (a) **FP1**, (b) **FP2** and (c) **FP3**. Other parameters: $\delta = 1$, $\omega_0^2 = 0.25$, $\kappa = 0.5$, $\eta = 0.1$ and $\beta = 1$.

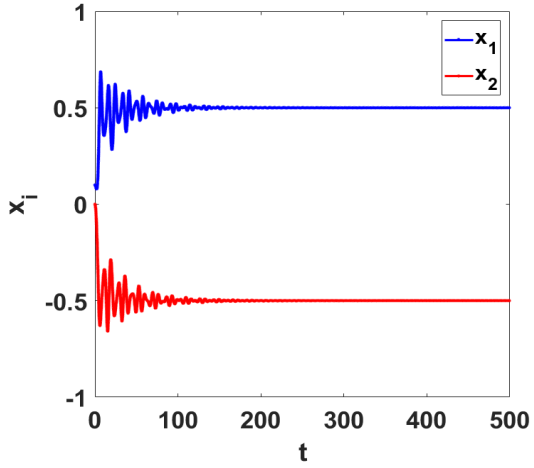

Figure 6.2: Temporal evolution of the two oscillators for $\gamma = 0.4$. Other parameters: $\delta = 1$, $\omega_0^2 = 0.25$, $\kappa = 0.5$, $\eta = 0.1$ and $\beta = 1$.

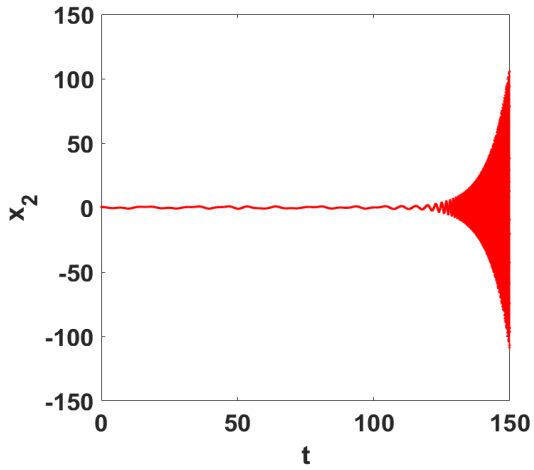

Figure 6.3: Temporal evolution of the gain oscillator for $\gamma = 0.4$. Other parameters: $\delta = 1$, $\omega_0^2 = 0.25$, $\kappa = 0.5$, $\eta = 0.1$ and $\beta = 1$.

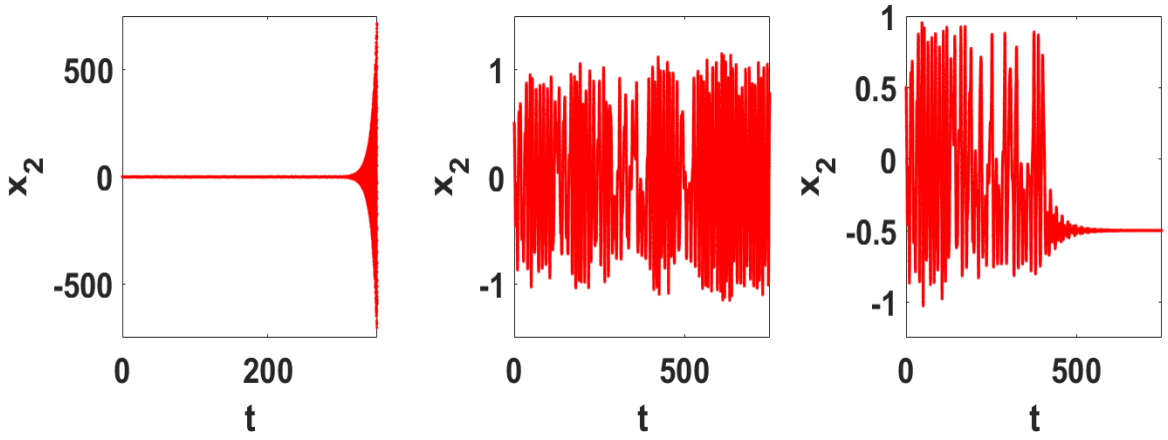

Figure 6.4: Temporal evolution of the gain oscillator for (a) $\psi = 10^{-3}$, (b) $\psi = 10^{-5}$, and (c) $\psi = 10^{-7}$. Other oscillator parameters: $\gamma = 0.4$, $\delta = 1$, $\omega_0^2 = 0.25$, $\kappa = 0.5$, $\eta = 0.1$ and $\beta = 1$. Drive parameters: $f_0 = 0.0001$ and $\omega = 2\pi/500$.

when the initial excitation imparted to the gain oscillator is far away from the attractor, we observe blow-up dynamics in our system.

We would discuss how such blow-up dynamics in the $\mathscr{PT}$-Symmetric Liénard system could be controlled using an external drive. We consider the drive to be of the form $f(t) = f_0 cos(\omega t + \psi t^3)$, where f_0 is the amplitude, ω is the frequency and ψ is the strength of the chirped modulation of the external drive. We observed that when we drive the loss oscillator using a chirped sinusoidal drive, blow-up dynamics could be controlled in the gain oscillator and at the same time, oscillatory behavior in the two oscillators ceases after a finite time on varying the strength of the external chirped modulation.

This phenomenon is known as '*oscillation death*' (OD). Oscillation death usually occurs in nonlinear systems as a consequence of the delay in coupling or some changes in the parameters of the system [102-105]. From our investigation, it could be seen that the temporal dynamics of our system are significantly affected by the strength of the external chirp modulation. In Fig. 6.4, we have plotted the temporal evolution of the gain oscillator for three cases of the strength of chirped modulation in the external drive. It could be seen that as we decrease the strength of the external chirp modulation, blow-up dynamics cease to exist in the gain oscillator and there is an emergence of aperiodic temporal dynamics for $\psi = 10^{-5}$ (Fig. 6.4(b)). But as the chirped modulation is decreased further, one can observe that the oscillations cease to exist after a certain time. From this, we could suggest that as the strength of the external chirp modulation is decreased, the cessation of blow-up dynamics gives rise to aperiodic temporal dynamics in the oscillators which, with time, leads to the emergence of oscillation death in the system (Fig. 6.4(c)). It could be seen that the external drive forces the temporal dynamics to converge to the stable fixed point (**FP2**). In this case, the stable fixed point for our choice of parameters is ($x_{1,0} = 0.5, y_{1,0} = 0, x_{2,0} = -0.5, y_{2,0} = 0$ and the temporal evolution of the gain oscillator shows complete convergence towards this fixed point. It has also been recently reported that external chirped driving could be utilized to control chaos in ultracold systems [101]. Hence, one could say that blow-up dynamics in the $\mathscr{PT}$-Symmetric Liénard oscillator could be controlled by externally driving the system.

6.3.2 Case II: $\delta = 2$

We now discuss the eigen spectra of the linearization Jacobian of the order-2 Liénard oscillator ($\delta = 2$) for the non-trivial fixed point **FP2**, which has been observed to be stable in the previous configuration. We have chosen three different frequencies of the oscillators and the coupling constant as $\kappa = 0.5$. From Fig. 6.5, we find that this configuration has a neutrally stable region in the Jacobian eigen spectra and the stability threshold of this configuration is at $\gamma_{th} \approx 0.475$ for $\omega_0^2 = 0.25$ and $\gamma_{th} \approx 0.575$ for $\omega_0^2 = 0.50$ respectively. This means that the non-trivial fixed point **FP2** is neutrally stable below γ_{th} and there will not be emergence of blow-up dynamics in this system. On the other hand, **FP2** is a saddle fixed point in the entire range of γ for $\omega_0^2 = 0.75$. For the analysis with regard to the temporal dynamics of our system, we have considered the gain/loss coefficient of the system as $\gamma = 0.1$, which is in the neutrally stable regime for $\omega_0^2 = 0.25$

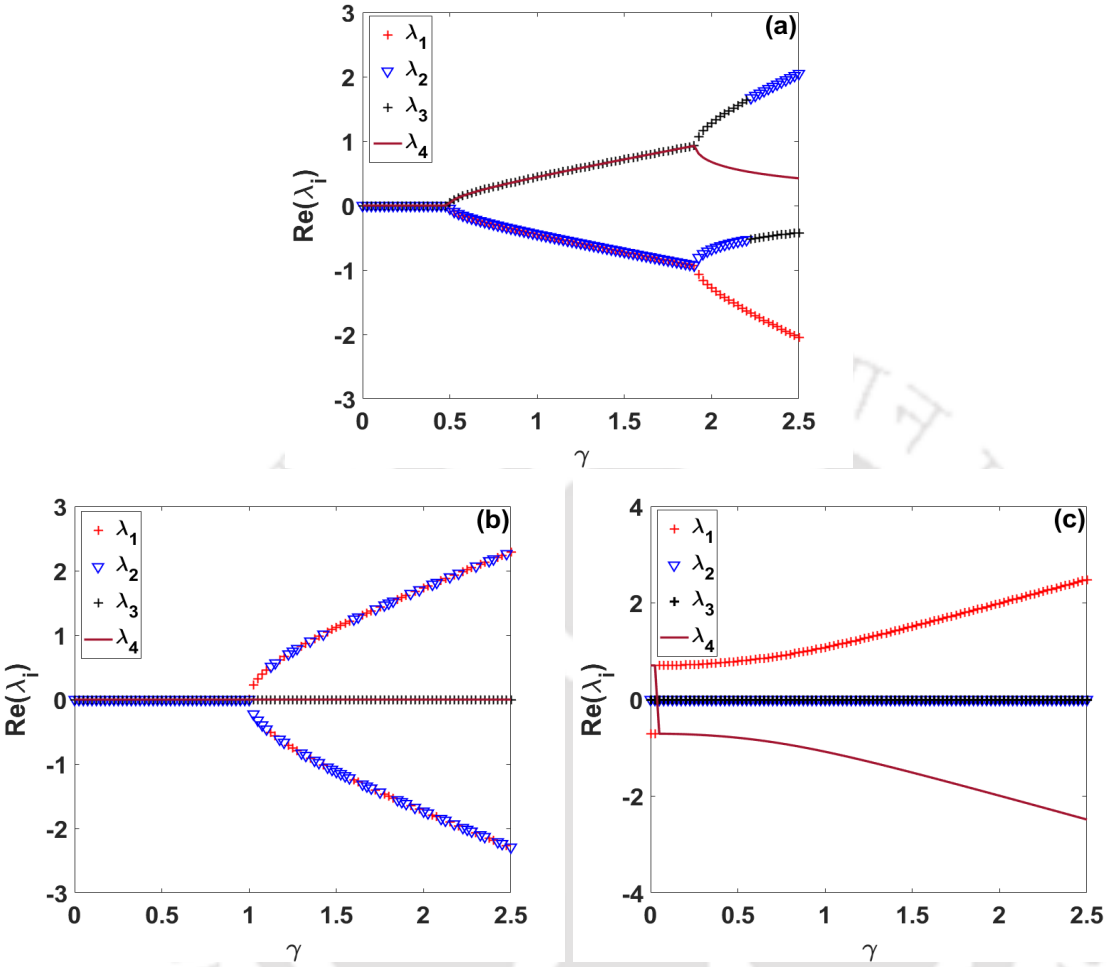

Figure 6.5: Real components of the Jacobian eigenvalues of the $\mathscr{PT}$-Symmetric Liénard oscillator for (a) $\omega_0^2 = 0.25$, (b) $\omega_0^2 = 0.50$ and (c) $\omega_0^2 = 0.75$. Other parameters: $\delta = 2$, $\kappa = 0.5$, $\eta = 0.1$ and $\beta = 1$.

and $\omega_0^2 = 0.5$. In Fig. 6.6, we have plotted the phase plane trajectory of the gain oscillator for all three frequencies of the oscillator. For $\omega_0^2 = 0.75$, it could be seen that the phase plane trajectory depicts a toroidal attractor (Fig. 6.6(a)) , which signifies the quasiperiodic temporal dynamics of the oscillators. On the other hand, decreasing the value of the frequency of the oscillators leads to the emergence of a chaotic Lorenz-type attractor in the phase plane of the gain oscillator (Fig. 6.6(c)). To validate our claims, we have plotted the power spectra of the gain oscillator for all three values of the frequency in Fig. 6.7. The power spectra (Fig. 6.7(a)) for $\omega_0^2 = 0.75$ show two distinct sharp peaks at $\Omega_1 = 0.418$ and $\Omega_2 = 0.894$. The ratio $\Omega_2/\Omega_1 \approx 2.1387$ is an incommensurate quantity and this validates our claim that our temporal dynamics show quasiperiodic behavior

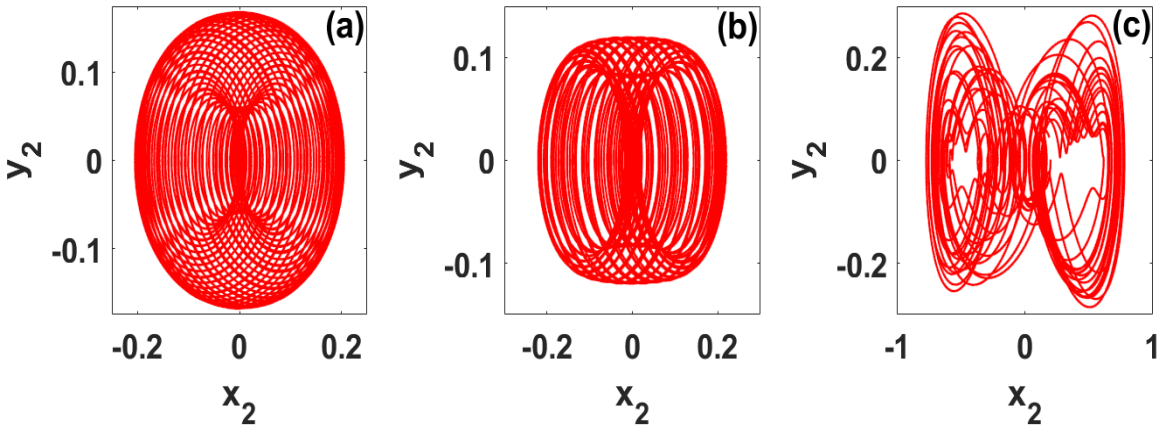

Figure 6.6: Phase plane trajectory of the gain oscillator for (a) $\omega_0^2 = 0.75$, (b) $\omega_0^2 = 0.50$ and (c) $\omega_0^2 = 0.25$. Other parameters: $\gamma = 0.1$, $\delta = 2$, $\kappa = 0.5$, $\eta = 0.1$ and $\beta = 1$.

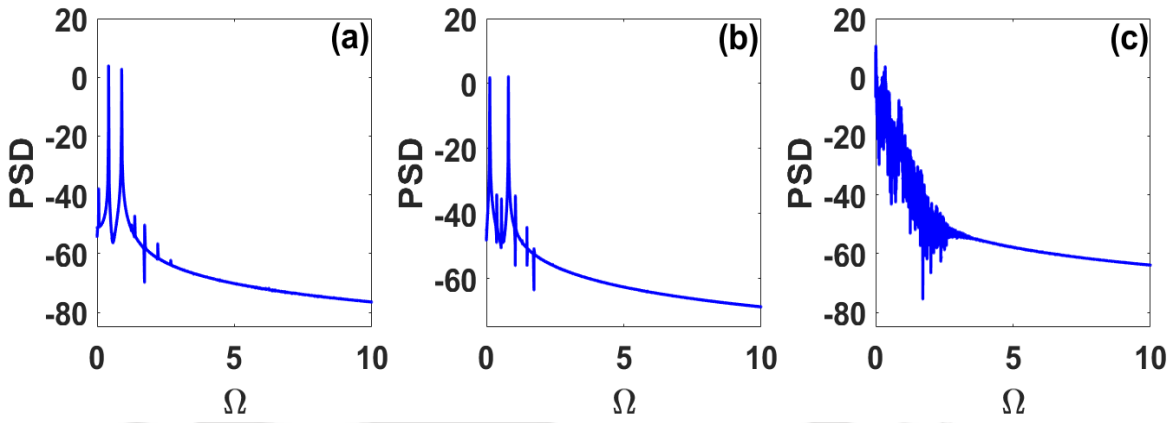

Figure 6.7: Power spectra of the gain oscillator for (a) $\omega_0^2 = 0.75$, (b) $\omega_0^2 = 0.50$ and (b) $\omega_0^2 = 0.25$. Other parameters: $\gamma = 0.1$, $\delta = 2$, $\kappa = 0.5$, $\eta = 0.1$ and $\beta = 1$.

[108]. In Fig. 6.7(b), we have plotted the power spectra for $\omega_0^2 = 0.5$. The power spectra once again delineate into two sharp peaks at $\Omega_1 = 0.126$ and $\Omega_2 = 0.802$ and the ratio $\Omega_2/\Omega_1 \approx 6.3651$, which is incommensurate. This tells us that the frequency ratio could be held incommensurate as we decrease the frequency of the oscillator. Furthermore, in the power spectra for $\omega_0^2 = 0.25$ (Fig. 6.7(c)), we find that the whole low frequency region is populated and there is an exponential decay in the higher frequency region. This depicts the chaotic behavior of our system and hence, we can conclude that our system exhibits the quasiperiodic route to chaos [44, 100].

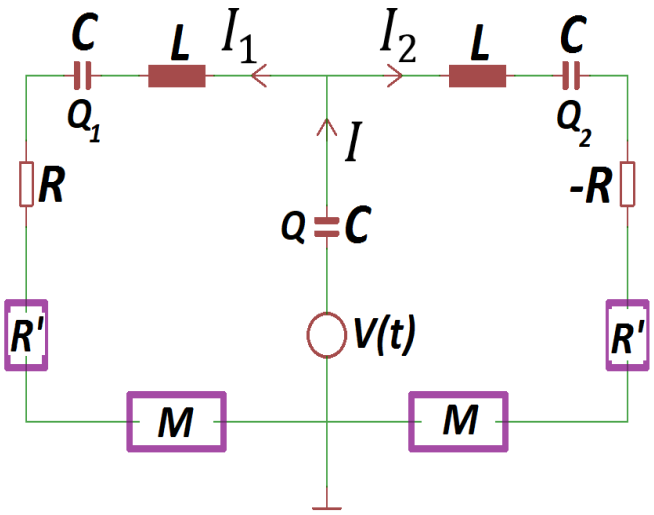

Figure 6.8: Schematic representation of the electronic circuit. Here, **L**, **C** and **R** are the inductor, capacitor and the resistor respectively. $\mathbf{R}'$ is the non-ohmic resistor and **M** is the current multiplier.

6.4 Experimental Realization

In this section, we provide a possible experimental route to realize our system studied in previous sections. Using Kirchoff's law of circuit analysis and in the absence of any resistive element and current multiplier, the equations governing the dynamics in electric current in a CLC circuit (see schematic Fig. 6.8) are given by

$$L\frac{dI_1}{dt}+\frac{Q_1}{C}+\frac{Q}{C}=V(t) \tag{6.4a}$$

$$L\frac{dI_2}{dt}+\frac{Q_2}{C}+\frac{Q}{C}=V(t) \tag{6.4b}$$

where Q , Q_1 and Q_2 are the charges in the capacitors. From the circuit diagram (Fig. 6.8), we can see that the electric charge in the capacitors can be written in terms of the current flowing in the circuit as follows.

$$\frac{dQ_1}{dt}=I_1,\quad \frac{dQ_2}{dt}=I_2,\quad \frac{dQ}{dt}=I \tag{6.5}$$

Hence, we have $Q=Q_1+Q_2$ and using this, we can eliminate Q in Eq. (6.4a) and (6.4b) and they can be rewritten as

$$L\frac{dI_1}{dt}+2\frac{Q_1}{C}+\frac{Q_2}{C}=V(t) \tag{6.6a}$$

$$L\frac{dI_2}{dt}+\frac{Q_2}{C}+2\frac{Q_2}{C}=V(t) \tag{6.6b}$$

Differentiating Eq. (6.6a) and Eq. (6.6b) and using Eq. (6.5), we obtain the following equations,

$$L\frac{d^2I_1}{dt^2}+\frac{2I_1+I_2}{C}=V^{'}(t) \tag{6.7a}$$

$$L\frac{d^2I_2}{dt^2}+\frac{I_1+2I_2}{C}=V^{'}(t) \tag{6.7b}$$

where $V^{'}=dV/dt$. These equations describe the oscillatory behavior of current in a CLC oscillator, but this system is not $\mathscr{PT}$-Symmetric. To ensure the presence of $\mathscr{PT}$-symmetry, we need to include a resistor in both loops. One of the resistors must induce attenuation in the electric current and the other needs to amplify in equal proportion. This can be achieved by using a negative resistance in one half of the circuit. Unlike a normal resistance, the I-V characteristics of a negative resistance shows a decrease in the current flowing through it when the potential difference is increased. A negative resistance can be realized in our circuit by using an Esaki diode or Gunn diode. Then, from Eq. (6.7a) and Eq. (6.7b), we have

$$\frac{d^2I_1}{dt^2}+\alpha\frac{dI_1}{dt}+\omega_0^2I_1+\kappa I_2=\frac{V^{'}(t)}{L} \tag{6.8a}$$

$$\frac{d^2I_2}{dt^2}-\alpha\frac{dI_2}{dt}+\omega_0^2I_2+\kappa I_1=\frac{V^{'}(t)}{L} \tag{6.8b}$$

where $\alpha=R/L$, $\omega_0^2=2/LC$ and $\kappa=1/LC$ are the linear gain/loss coefficient, nonlinear resistance, natural frequency of the oscillator and the coupling constant respectively.

Until this point, we have not yet included nonlinear resistance and current multiplier in the circuit that would facilitate the realization of our theoretical model. The nonlinear resistance R_{nl} could be realized by using a non-ohmic resistance. In a non-ohmic resistance, the I-V characteristics do not follow a straight line. Instead, the gradient of the graph increases as the current is increased. We choose our nonlinear resistance to follow the generalized I-V characteristics law given by $V_{nl,i}=R_{nl,i}I^{\delta}$, where R_{nl} is the coefficient and δ is the exponent of nonlinear resistance respectively. Also, the Duffing nonlinearity could be easily realized in our circuit by using an analog device multipliers *AD532* or *AD534* [44]. For current inputs X and Y, such a device would produce an output $XY/10$. Then from Eqs. (6.8a) and (6.8b), we have

$$\frac{d^2I_1}{dt^2}+(\alpha+\beta_1I_1^{\delta-1})\frac{dI_1}{dt}+\omega_0^2I_1+\kappa I_2=\frac{V^{'}(t)}{L} \tag{6.9a}$$

$$\frac{d^2I_2}{dt^2}-(\alpha-\beta_2I_2^{\delta-1})\frac{dI_2}{dt}+\omega_0^2I_2+\kappa I_1=\frac{V^{'}(t)}{L} \tag{6.9b}$$

where $\beta_i = \delta R_{nl,i}/L$ $(i = 1,2)$ is the coefficient of nonlinear resistance. One important thing that must be noted is that for both configurations that we studied, we must have $\beta_2 = -\beta_1$. This implies that one of the non-ohmic resistors must instead play the role of a nonlinear amplifier.

6.5 Summary

We investigated a $\mathscr{PT}$-Symmetric Liénard oscillator configuration for two cases of nonlinear dissipation. We analyzed the stability of the stationary states using the linearization Jacobian technique. Spectral analysis of the Jacobian showed us that the system has a stable, an unstable and a saddle fixed point. It has been found that when the initial conditions are chosen far away from the stable fixed point, the order-1 model gives rise to blow-up dynamics in the gain oscillator. This leads us to infer that the stable fixed point is a locally stable fixed point. Using an external chirped sinusoidal drive, blow-up dynamics could be controlled and oscillation death could be achieved in the system. This means that an external signal could be used to control the emergence of blow-up dynamics in our system. On the other hand, the order-2 model gives rise to the quasiperiodic route to chaos in the neutrally stable regime of the Jacobian eigen spectra. For potential experimental realization of our models, we proposed an electronic circuit using Kirchoff's laws. The gain oscillator could be realized using a negative resistance, nonlinear dissipation using a non-ohmic resistance and Duffing nonlinearity using an analog devices multiplier.

We anticipate that these systems could be scaled up to many oscillators, and this will open an interesting avenue to understand control of blow-up and chaotic dynamics in many body driven-dissipative systems.

CHAPTER 7

CONCLUSION

In this thesis, we have discussed the numerous phenomena that arise in a $\mathcal{PT}$-symmetric optical system from a dynamical perspective. In chapter 2, we discussed the linearization Jacobian approach in the stability analysis of nonlinear systems for discrete as well as continuous-time dynamical systems. Furthermore, we also discussed the methods used in the characterization of chaotic dynamics in such systems. To illustrate these methods, we made use of the Logistic map and the driven Duffing oscillator as examples.

In chapter 3, we discussed the Kerr nonlinearity induced stability threshold and the self-stabilizing characteristics of the nonlinear $\mathcal{PT}$-symmetric coupler from a dynamical perspective. Moreover, we showed how the $\mathcal{PT}$ threshold of the linear $\mathcal{PT}$-symmetric coupler governs the existence of fixed points in such systems. Furthermore, we discussed the toroidal trajectory in the phase plane of the real and imaginary components of the field amplitudes.

In chapter 4, we studied the chaotic dynamics that arises in optical ring resonator systems. Using the transfer matrix formalism, we mathematically modelled the systems using a discrete time iterative equation known as the Ikeda Map. We have proposed two different configurations. In the first configuration, we showed how chaotic dynamics could be controlled in a single fiber ring resonator system with an amplified input channel and a lossy ring. On top of that, we discussed as to how the amplitude of the input field could trigger the period doubling route to chaos in such systems and how the gain/loss parameter of the system could control such dynamical transitions. Furthermore, we

also discussed the resonance profile of the system, emphasizing on the experimental realization of such systems. The second configuration is an improvement upon the first and it includes two ring resonators that are coupled by a $50:50$ directional coupler. After the evaluation of the $\mathscr{PT}$ threshold in the linear regime, we discussed the optical power saturation and blow-up characteristics of the system in the unbroken and broken $\mathscr{PT}$ regime respectively. On top of that, we showed how such characteristics could be attributed to the existence of stable stationary states on the surface of a four dimensional hypersphere. Afterwards, we discussed the dynamical characteristics of the system in the nonlinear regime and how the introduction of Kerr nonlinearity into the systems brings forth the period doubling route to chaos and how the largest Lyapunov exponent of the system blows up in the neighborhood of the $\mathscr{PT}$ threshold. And then, we showed the emergence of chaotic spiking of optical power in the nonlinear regime as a result of extremely high largest Lyapunov exponent.

In chapter 5, we explored the transmission and reflection characteristics of a $\mathscr{PT}$-symmetric multilayered structure, which is essentially a two port device. We mathematically modeled this structure using the transfer matrix formalism, which could be constructed from the boundary conditions of the electric and magnetic fields at each interface. We chose the $1550nm$ wavelength in our discussion, for the important role it plays in the telecommunication sector. We discussed the optical power propagation characteristics in the unbroken and broken $\mathscr{PT}$ regime for both cases of power launched from either of the two ports. We then validated our theoretical observations using FDTD simulation. Afterwards, we showed how changing the length of layers could generate spectral singularities in the S-matrix eigen spectrum and how this could be attributed to the imaginary component of the transfer matrix eigenvalues flipping its sign. Then, we discussed how such spectral singularities could facilitate highly amplified transmission of optical power through such structure. On top of that, the visible spectra could be seen to be entirely blocked.

In chapter 6, we discussed the $\mathscr{PT}$-symmetric Liénard oscillator for two different configurations of position dependent nonlinear damping. In the first case, stability analysis of the linearization Jacobian eigen spectra showed us that the systems admits a stable, an unstable and a saddle fixed point for our choice of parameters. When the gain oscillator is given an initial excitation nearer to the stable fixed point, the time series is found to instantaneously propagate towards the stable fixed point. But when it is given an excitation far away, the gain oscillator exhibits blow-up dynamics. Such

dynamics illustrates the locally stable aspects of the stable fixed point. Afterwards, it has been found that an external chirped sinusoidal drive could control such dynamics and furthermore, such a drive could initiate the emergence of oscillation death in the system. In the second case, the stable non-trivial fixed point of the first configuration has a neutrally stable regime, in which it has been observed that the system exhibits quasiperiodic temporal dynamics. This we validated from the power spectral density of the time series. Moreover, at a certain value of the frequency of the oscillator, the temporal dynamics exhibit chaotic phase plane trajectory and hence, it could be concluded that the second configuration exhibits the quasiperiodic route to chaos. Moreover, we also gave an experimental scheme to realize the theoretical observations of our model.

Future Aspects

The temporal dynamics of nonlinear $\mathscr{PT}$-symmetric systems has proven to be a promising area of research due to the numerous phenomena associated with it and its corresponding applications. For instance, the $\mathscr{PT}$-symmetric double ring resonator problem could also be exploited to study synchronization of chaos [106-108] and such systems could also play an important role in noise control applications. The system is also an unidirectional coupler and it could also find applications in many other optical as well as optoelectronic systems. In the emerging field of all-optical reservoir computing, high speed computing using $\mathscr{PT}$-symmetric micro-ring resonators is a definite future possibility [109-110]. Moreover, if the intermittent chaotic spiking that we observed in our work could be controlled and transformed to periodically pulsed optical power, such a system could also be seen as a proposal for $\mathscr{PT}$-symmetric ring laser system and the same could be said for stochastic resonance in such systems [62-63]. Also, such ring resonator systems are time-delayed Ikeda-type optical systems and so, the various aspects of temporal delay and gain/loss coefficient in $\mathscr{PT}$-symmetric semiconductor lasers (which are also Ikeda-type systems) is yet another future prospect of such systems. In addition to this, this thesis discussed the discrete-time $\mathscr{PT}$-symmetric Ikeda type optical systems and the continuous-time counterpart is yet another topic of research that is still to be investigated and reported.

On the other hand, the management of blow-up as well as chaotic dynamics in $\mathscr{PT}$-symmetric Liénard oscillators could be extended to electronic and optoelectronic systems and thereby leading to the experimental realization and applications of such systems.

Moreover, the Liénard oscillator of order-1 nonlinear dissipation and zero linear gain/loss coefficient is $\mathscr{PT}$-symmetric without the need for an additional oscillator and the investigation of synchronization as well as the emergence of chimera states in an ensemble of such oscillators is a definite possibility in the future [111-113]. Furthermore, such oscillators are also systems where the appealing but not widely appreciated temporal dynamics known as Transient Chaos could be studied [115-116]. Moreover, transient chaos has already been reported in electronic oscillators [117-119], lasers [120-122], parametrically forced pendulum [123], Duffing oscillators [124] and so on. So, investigation of transiently chaotic dynamics in $\mathscr{PT}$-Symmetric Liénard oscillators is yet another possibility that could be considered for the future.

Investigations on Kerr nonlinearity induced $\mathscr{PT}$ threshold and self-stabilizing characteristics of the $\mathscr{PT}$-symmetric nonlinear coupler could also be extended to bigger and more complicated coupled optical waveguide structures such as the trimmer [20] and quadrimer [22,74,114]. Moreover, the collective dynamics of optical power oscillation in passive as well as $\mathscr{PT}$-symmetric coupled waveguide structures is an interesting topic of research for consideration in the future. Furthermore, in the $\mathscr{PT}$-symmetric multilayered structure discussed in this thesis, discussion of the transmission and reflection characteristics of the system is limited to normal incidence of light. So, highly amplified transmission in the infrared spectrum and spectral singularities of the structure for other angles of incidence is definitely a topic of research that must be considered. Also, the same could be said for designing frequency combs in such multilayered systems.

Thus, in conclusion, it could very well be said that out work has thrown light into various future aspects that could be investigated in $\mathscr{PT}$-symmetric optical systems from a dynamical perspective and much richer temporal dynamics and interesting features in such systems be reported.

BIBLIOGRAPHY

[1] C. M. Bender, S. Boettcher: Real Spectra in Non-Hermitian Hamiltonians Having $\mathscr{PT}$ Symmetry. Phys. Rev. Lett. 80, 5243 (1998).

[2] C. M. Bender, S. Boettcher, P. N. Meisinger: $\mathscr{PT}$-symmetric quantum mechanics. J. Math. Phys. 40, 2201 (1999).

[3] C. M. Bender, D.C. Brody, H. F. Jones: Complex Extension of Quantum Mechanics. Phys. Rev. Lett. 89, 270401 (2002).

[4] C. M. Bender: Making sense of non-Hermitian Hamiltonians. Rep. Prog. Phys, 70, 947 (2007).

[5] A. Mostafazadeh: Exact $\mathscr{PT}$-Symmetry Is Equivalent to Hermiticity, J. Phys. A. 36, 7081, (2003).

[6] C. M. Bender: $\mathscr{PT}$-Symmetric Quantum Field Theory. AIP Conference Proceedings 1389, 642 (2011)

[7] C. M. Bender, V. Branchina, and E. Messina: Critical behavior of the $\mathscr{PT}$-symmetric $i\phi^3$ quantum field theory. Phys. Rev. D 87, 085029 (2013).

[8] C. M. Bender, N. Hassanpour, S. P. Klevansky and S. Sarkar: $\mathscr{PT}$-symmetric quantum field theory in D dimensions. Phys. Rev. D 98, 125003 (2018).

[9] I. Ya. Goldsheid and B. A. Khoruzhenko: Distribution of Eigenvalues in Non-Hermitian Anderson Models, Phys. Rev. Lett. 80, 2897 (1998).

[10] I. Rotter: A non-Hermitian Hamilton operator and the physics of open quantum systems. J. Phys. A 42, 153001 (2009).

[11] R. El-Ganainy, K. G. Makris, D. N. Christodoulides and Z. H. Musslimani: Theory of coupled optical $\mathscr{PT}$-Symmetric structures. Opt. Lett. 32, 2632 (2007).

[12] C. E. Rüter *et al.*: Observation of parity–time symmetry in optics. Nat. Phys. 6, 192 (2010).

[13] Z. Lin, H. Ramezani, T. Eichelkraut, T. Kottos, H. Cao, and D. N. Christodoulides: Unidirectional invisibility induced by $\mathscr{PT}$-symmetric periodic structures, Phys. Rev. Lett. 106, 213901 (2011).

[14] S. Assawaworrarit, X. Yu and S. Fan: Robust wireless power transfer using a nonlinear parity-time-symmetric circuit, Nat. 546, 387 (2017).

[15] H. Alaeian and J. A. Dionne: Parity-time-symmetric plasmonic metamaterials, Phys. Rev. A 89, 033829 (2014).

[16] H. Benisty *et al.*: Implementation of $\mathscr{PT}$ symmetric devices using plasmonics: principle and applications, Opt. Express 19, 18004 (2011).

[17] M. Sarisaman: Unidirectional reflectionlessness and invisibility in the TE and TM modes of a $\mathscr{PT}$-symmetric slab system, Phys. Rev. A 95, 013806 (2017).

[18] J. P. Deka and A. K. Sarma: Highly Amplified Light Transmission in Parity-Time Symmetric Multilayered Structure, Appl. Opt. 57, 1119 (2018).

[19] M. Duanmu, K. Li, R. L. Horne, P. G. Kevrekidis, and N. Whitaker: Linear and nonlinear parity-time-symmetric oligomers: a dynamical systems analysis, Philos. Trans. R. Soc. A 371, 20120171 (2013).

[20] K. Li, P. G. Kevrekidis, D. J. Frantzeeskakis, C. E. Rter, and D. Kip: Revisiting the $\mathscr{PT}$-symmetric trimer: bifurcations, ghost states and associated dynamics, J. Phys. A Math. Gen. 46, 375304 (2013).

[21] K. Li, P. G. Kevrekidis: $\mathscr{PT}$-symmetric oligomers: Analytical solutions, linear stability, and nonlinear dynamics, Phys. Rev. E 83, 066608 (2011).

[22] S. K. Gupta, J. P. Deka, and A. K. Sarma: Nonlinear parity-time symmetric closed-form optical quadrimer waveguides: attractor perspective, Eur. Phys. J. D 69, 199 (2015).

[23] J. P. Deka and A. K. Sarma: Perturbative Dynamics of Stationary States in Nonlinear Parity-Time Symmetric Coupler, Commun. Nonlin. Sci. Num. Simul. 57, 26 (2017).

[24] I. V. Barashenkov, G. S. Jackson and S. Flach: Blow-up regimes in the $\mathscr{PT}$-symmetric coupler and the actively coupled dimer, Phys. Rev. A 88, 053817 (2013).

[25] I. V. Barashenkov: Hamiltonian formulation of the standard $\mathscr{PT}$-symmetric nonlinear Schrödinger dimer, Phys. Rev. A 90, 045802 (2014).

[26] I. V. Barashenkov, D. E. Pelinovsky and P. Dubard: Dimer with gain and loss: Integrability and $\mathscr{PT}$-symmetry restoration, J. Phys. A: Math. Theor. 48, 325201 (2015).

[27] I. V. Barashenkov and M. Gianfreda: Dimer with gain and loss: Integrability and PT-symmetry restoration J. Phys. A: Math. Theor. 47, 282001 (2014).

[28] R. Driben and B.A. Malomed: Stability of solitons in parity-time-symmetric couplers, Opt. Lett. 36, 4323 (2011).

[29] M. –A. Miri, A. B. Aceves, T. Kottos, V. Kovanis, D. N. Christodoulides: Bragg solitons in nonlinear $\mathscr{PT}$-symmetric periodic potentials, Phys. Rev. A 86, 033801 (2012).

[30] Y. V. Bludov, V. V. Konotop, and B. A. Malomed: Stable dark solitons in $\mathscr{PT}$-symmetric dual-core waveguides, Phys. Rev. A 87, 013816 (2013).

[31] Z. Yan, Z. Wen, and V. V. Konotop: Solitons in a nonlinear Schrödinger equation with $\mathscr{PT}$-symmetric potentials and inhomogeneous nonlinearity: Stability and excitation of nonlinear modes, Phys. Rev. A 92, 023821 (2015).

[32] A. K. Sarma, M.-A. Miri, Z. H. Musslimani, D. N. Christodoulides: Continuous and discrete Schrödinger systems with parity-time-symmetric nonlinearities, Phys. Rev. E 89, 052918 (2014).

[33] Z. Chen, J. Huang, J. Chai, X. Zhang, Y. Li, and B. A. Malomed: Discrete solitons in self-defocusing systems with $\mathscr{PT}$-symmetric defects, Phys. Rev. A 91, 053821 (2015).

[34] S. K. Gupta and A. K. Sarma: Solitary waves in parity-time ($\mathscr{PT}$)–symmetric Bragg grating structure and the existence of optical rogue waves, Europhys. Lett. 105, 44001 (2014).

[35] A. Govindarajan, A. K. Sarma and M. Lakshmanan: Tailoring $\mathscr{PT}$-symmetric soliton switch, Opt. Lett. 44, 663 (2019).

[36] Z. Yan, Z. Wen, and C. Hang: Spatial solitons and stability in self-focusing and defocusing Kerr nonlinear media with generalized parity-time-symmetric Scarff-II potentials, Phys. Rev. E 92, 022913 (2015).

[37] H. Wang, D. N. Christodoulides: Two dimensional gap solitons in self-defocusing media with $\mathscr{PT}$-symmetric superlattice, Commun. Nonlin. Sci. Num. Simul. 38, 130 (2016).

[38] X. Xu, Y. Liu, C. Sun, and Y. Li: Mechanical $\mathscr{PT}$-Symmetry in coupled optomechanical systems, Phys. Rev. A 92, 013852 (2015).

[39] X. Lü, H. Jing, J. Ma, and Y. Wu: $\mathscr{PT}$-Symmetry-Breaking Chaos in Optomechanics, Phys. Rev. Lett. 114, 253601 (2015).

[40] J. Schindler, A. Li, M. C. Zheng, F. M. Ellis, and T. Kottos: Experimental study of active LRC circuits with $\mathscr{PT}$-symmetries, Phys. Rev. A 84, 040101 (2011).

[41] M. -A. Miri, A. Regensburger, U. Peschel and D. N. Christodoulides: Optical mesh lattices with $\mathscr{PT}$ symmetry, Phys. Rev. A 86, 023807 (2012).

[42] S. Karthiga, V. K. Chandrasekar, M. Senthilvelan, and M. Lakshmanan: Twofold $\mathscr{PT}$ symmetry in nonlinearly damped dynamical systems and tailoring $\mathscr{PT}$ regions with position-dependent loss-gain profiles, Phys. Rev. A 93, 012102 (2016).

[43] C. M. Bender, B. K. Berntson, D. Parker, and E. Samuel: Observation of $\mathscr{PT}$ phase transition in a simple mechanical system, Am. J. Phys. 81, 173 (2013).

[44] M. Lakshmanan and S. Rajasekar, Nonlinear Dynamics - Integrability, Chaos and Patterns, Springer (2003).

[45] S. Strogatz: Nonlinear Dynamics and Chaos, Westview Press (2001).

[46] E. N. Lorenz: Deterministic Nonperiodic Flow, Journal of the Atmospheric Sciences 20 (2): 130–141 (1963).

[47] O. E. Rössler: An Equation for Continuous Chaos, Phys. Lett. A 57, 397 (1976).

[48] D. W. Jordan and P. Smith: Nonlinear Ordinary Differential Equations, Oxford University Press (1999).

[49] R. M. May: Simple mathematical models with very complicated dynamics, Nat. 261, 459 (1976).

[50] M. Hénon: A two-dimensional mapping with a strange attractor, Comm. in Math. Phys. 50 , 69 (1976).

[51] K. Ikeda, H. Daido and O. Akimoto: Optical Turbulence: Chaotic Behavior of Transmitted Light from a Ring Cavity, Phys. Rev. Lett. 45, 709–712 (1980).

[52] L. Gyorgi and R. J. Field: A three-variable model of deterministic chaos in the Belousov–Zhabotinsky reaction, Nature 355, 808 (1992).

[53] V. Petrov, V. Gaspar, J. Masere and K. Showalter: Controlling chaos in the Belousov—Zhabotinsky reaction, Nature 361, 240 (1993).

[54] L. Gyorgi and R. J. Field: Simple models of deterministic chaos in the Belousov-Zhabotinskii reaction, J. Phys. Chem. 95, 6594 (1991).

[55] T. Matsumoto: A chaotic attractor from Chua's circuit, IEEE Trans. Circuits Syst. 31, 1055 (1984).

[56] A. D. Stone: Chaotic billiard lasers, Nature 465, 696 (2010).

[57] P. Ashwin, J. R. Terry, K. S. Thornburg Jr., and R. Roy: Blowout bifurcation in a system of coupled chaotic lasers, Phys. Rev. E 58, 7186 (1998).

[58] H. G. Winful and L. Rahman, Synchronized chaos and spatiotemporal chaos in arrays of coupled lasers, Phys. Rev. Lett. 65, 1575 (1990).

[59] P. G. Drazin and R. S. Johnson: Solitons: An Introduction, Cambridge University Press (1989).

[60] J. R. Terry, K. Scott Thornburg, Jr., D. J. DeShazer, G. D. VanWiggeren, S. Zhu, P. Ashwin and R. Roy: Synchronization of chaos in an array of three lasers, Phys. Rev. E 59, 4036 (1999).

[61] E. A. Rogers-Dakin, J. García-Ojalvo, D. J. DeShazer and R. Roy: Synchronization and symmetry breaking in mutually coupled fiber lasers, Phys. Rev. E 73, 045201 (2006).

[62] G. Vemuri and R. Roy: Stochastic resonance in a bistable ring laser, Phys. Rev. A 39, 4668 (1989).

[63] B. McNamara, K. Wiesenfeld and R. Roy: Observation of Stochastic Resonance in a Ring Laser, Phys. Rev. Lett. 60, 2626 (1988).

[64] A. M. Hagerstrom, T. E. Murphy, R. Roy, P. Hövel, I. Omelchenko and E. Schöll: Experimental observation of chimeras in coupled-map lattices, Nat. Phy. 8, 658 (2012).

[65] J. Zamora-Munt, C. Masoller, J. Garcia-Ojalvo and R. Roy: Crowd Synchrony and Quorum Sensing in Delay-Coupled Lasers, Phys. Rev. Lett. 105, 264101 (2010).

[66] S. T. Thornton and J. B. Marion: Classical Dynamics of Particles and Systems, Cengage Learning (2009).

[67] K. Li and P. G. Kevrekidis: $\mathscr{PT}$-symmetric oligomers: Analytical solutions, linear stability, and nonlinear dynamics, Phys. Rev. E 83, 066608 (2011).

[68] H. Ramezani, T. Kottos, R. El-Ganainy and D. N. Christodoulides: Unidirectional nonlinear $\mathscr{PT}$-symmetric optical structures, Phys. Rev. A 82, 043803 (2010).

[69] I. V. Barashenkov, G. S. Jackson and S. Flach: Blow-up regimes in the $\mathscr{PT}$-symmetric coupler and the actively coupled dimer, Phys. Rev. A 88, 053817 (2013).

[70] I. V. Barashenkov: Hamiltonian formulation of the standard $\mathscr{PT}$-symmetric nonlinear Schrödinger dimer, Phys. Rev. A 90, 045802 (2014).

[71] I. V. Barashenkov, D. E. Pelinovsky and P. Dubard: Dimer with gain and loss: Integrability and $\mathscr{PT}$-symmetry restoration, J. Phys. A: Math. Gen. 48, 32 (2015).

[72] I. V. Barashenkov, L. Baker and N. V. Alexeeva: $\mathscr{PT}$-symmetry breaking in a necklace of coupled optical waveguides, Phys. Rev. A 87, 033819 (2013).

[73] K. Li, P. G. Kevrekidis, D. J. Frantzeeskakis, C. E. Rüter and D. Kip: Revisiting the $\mathscr{PT}$-symmetric trimer: bifurcations, ghost states and associated dynamics, J. Phys. A: Math. Gen. 46, 375304 (2013).

[74] S. K. Gupta, J. P. Deka and A. K. Sarma: Nonlinear parity-time symmetric closed-form optical quadrimer waveguides: attractor perspective, Eur. Phys. J. D 69, 199 (2015).

[75] J. Argyris, G. Faust, M. Haase, R. Friedrich: An exploration of dynamical systems and chaos, Springer, Berlin (2nd edition, 2015).

[76] J. C. Sprott and W. G. Hoover: Harmonic Oscillators with Nonlinear Damping, Int. J. Bifurc. Chaos 27, 1730037 (2017).

[77] L. Zhou and F. Chen: Sil'nikov chaos of the Liu system, Chaos 18, 013113 (2008).

[78] J. K. Hale and H. Koçak: Dynamics and bifurcations, Springer, New York (1991).

[79] A. P. Kuznetsov, A. V. Savin, D. V. Savin: On some properties of nearly conservative dynamics of Ikeda map and its relation with the conservative case, Phys. A 387, 1464 (2008).

[80] G. Steinmeyer, D. Jaspert, F. Mitschke: Observation of a period-doubling sequence in a nonlinear optical fiber ring cavity near zero dispersion. Opt. Commun. 104, 379 (1994).

[81] M. Haelterman: Period-doubling bifurcations and modulational instability in the nonlinear ring cavity: an analytical study, Opt. Lett. 17, 792 (1992).

[82] G. Steinmeyer, A. Buchholz, M. Hansel, M. Heuer, A. Schwache, F. Mitschke: Dynamical pulse shaping in a nonlinear resonator. Phys. Rev. A 52, 830 (1995).

[83] R. Vallée: Temporal instabilities in the output of an all-fiber ring cavity. Opt. Commun. 81, 419 (1991).

[84] S. Lynch, A. L. Steele, J. E. Hoad: Stability analysis of nonlinear optical resonators. Chaos Solitons Fractals 9, 935 (1998).

[85] A. Regensburger, C. Bersch, M. -A. Miri, G. Onishchukov, D. N. Christodoulides and U. Peschel: Parity-time synthetic photonic lattices. Nature 488, 167 (2012)

[86] M. Wimmer, A. Regensburger, M.-Ali Miri, C. Bersch, D. N. Christodoulides and U. Peschel: Observation of optical solitons in $\mathscr{PT}$-symmetric lattices, Nat. Comm. 6, 7782 (2015).

[87] A. Regensburger, M.-Ali Miri, C. Bersch, J. Näger, G. Onishchukov, D. N. Christodoulides, and U. Peschel: Observation of Defect States in $\mathscr{PT}$-Symmetric Optical Lattices, Phys. Rev. Lett. 110, 223902 (2013).

[88] P. Yeh: Optical Waves in Layered Media (Wiley, 2005).

[89] P. Markos and C. M. Soukoulis: Wave Propagation - From Electrons to Photonic Crystals and Left-Handed Materials (Princeton University Press, 2008).

[90] T. R. Zhan and S. T. Chui: Theory of the spontaneous-decay enhancement in plasmonic nanoparticles based on a singularity representation of the scattering matrix, Phys. Rev. A 90, 023802 (2014).

[91] A. A. Andronov, E. A. Leontovich, I. I. Gordon and A. G. Maier: Qualitative Theory of Second-Order Dynamical Systems (Wiley, New York, 1973).

[92] B. Van der Pol: On "relaxation-oscillations", Phil. Mag. Ser. 7, 2, 978 (1926).

[93] B. Van der Pol and J. Van der Mark: The heartbeat considered as a relaxation oscillation, and an electrical model of the heart, Phil. Mag. Ser. 7, 6, 763 (1928).

[94] T. P. Dinh, J. Demongeot, P. Baconnier and G. Benchetrit: Simulation of a biological oscillator: the respiratory system, J. Theor. Biol. 103, 113 (1983).

[95] P. F. Rowat and A. I. Selverston: Modeling the gastric mill central pattern generator of the lobster with a relaxation-oscillator network, J. Neurophysiol. 70, 1030 (1993).

[96] R. Fitzhugh: Impulses and Physiological States in Theoretical Models of Nerve Membrane, Biophys. J. 1, 445 (1961).

[97] R. FitzHugh, Mathematical models of threshold phenomena in the nerve membrane, Bull. Math. Biophysics, 17, 257 (1955).

[98] J. Nagumo, S. Arimoto and S. Yoshizawa: An active pulse transmission line simulating nerve axon, Proc. IRE, 50, 2061 (1962).

[99] S. L. Kingston, K. Thamilmaran, P. Pal, U. Feudel and S. K. Dana: Extreme events in the forced Liénard system, Phys. Rev. E 96, 052204 (2017).

[100] T. W. Dixon, T. Gherghetta, and B. G. Kenny: Universality in the quasiperiodic route to chaos, Chaos 6, 32 (1996).

[101] S. Dutta, P. K. Mishra, B. Chatterjee and S. Basu: Dynamics of interacting bosons in a double-well potential, Europhys. Lett. 124, 30002 (2018).

[102] G. Saxena, A. Prasad and R. Ramaswamy: Amplitude death: The emergence of stationarity in coupled nonlinear systems, Phys. Rep. 512, 205 (2012).

[103] R. Karnatak, R. Ramaswamy and A. Prasad: Amplitude death in the absence of time delays in identical coupled oscillators, Phys. Rev. E 76, 035201 (2007).

[104] A. Prasad: Amplitude death in coupled chaotic oscillators, Phys. Rev. E 72, 056204 (2005).

[105] A. Prasad, M. Dhamala, B. M. Adhikari, and R. Ramaswamy: Amplitude death in nonlinear oscillators with nonlinear coupling, Phys. Rev. E 81, 027201 (2010).

[106] I. Reidler *et al.*: Coupled lasers: phase versus chaos synchronization, Opt. Lett. 38, 4174 (2013).

[107] R. Roy and K. S. Thornburg Jr.: Experimental synchronization of chaotic lasers, Phys. Rev. Lett. 72, 2009 (1994).

[108] P. Colet and R. Roy: Digital communication with synchronized chaotic lasers, Opt. Lett. 19, 2056 (1994).

[109] C. Mesaritakis, V. Papataxiarhis, and D. Syvridis: Micro ring resonators as building blocks for an all-optical high-speed reservoir-computing bit-pattern-recognition system, JOSA B 30, 3048 (2013).

[110] F. D. Coarer *et al.*: All-Optical Reservoir Computing on a Photonic Chip Using Silicon-Based Ring Resonators, IEEE J. Sel. Top. Quantum Electron. 24, 1 (2018).

[111] D. M. Abrams and S. H. Strogatz: Chimera States for Coupled Oscillators, Phys. Rev. Lett. 93, 174102 (2004).

[112] S. H. Strogatz: From Kuramoto to Crawford: exploring the onset of synchronization in populations of coupled oscillators, Phys. D 143 , 1 (2000).

[113] A. Mishra, C. Hens, M. Bose, P. K. Roy, and S. K. Dana: Chimera like states in a network of oscillators under attractive and repulsive global coupling, Phys. Rev. E 92, 062920 (2015).

[114] P. A. Kalozoumis, C. V. Morfonios, F. K. Diakonos, and P. Schmelcher: $\mathscr{PT}$-symmetry breaking in waveguides with competing loss-gain pairs, Phys. Rev. A 93, 063831 (2016).

[115] T. Tél: The joy of transient chaos, Chaos 25, 097619 (2015).

[116] Y. -C. Lai and T. Tél: Transient Chaos: Complex Dynamics on Finite-Time Scales (Springer, New York, 2011).

[117] F. T. Arecchi and F. Lisi: Hopping Mechanism Generating 1 f Noise in Nonlinear Systems Phys. Rev. Lett. 49, 94 (1982).

[118] R. Hilborn: Quantitative measurement of the parameter dependence of the onset of a crisis in a driven nonlinear oscillator, Phys. Rev. A 31, 378 (1985).

[119] R. Rollins and E. Hunt: Intermittent transient chaos at interior crises in the diode resonator, Phys. Rev. A 29, 3327 (1984).

[120] F. T. Arecchi, R. Meucci, G. Puccioni, and J. Tredicce: Experimental Evidence of Subharmonic Bifurcations, Multistability, and Turbulence in a Q-Switched Gas Laser, Phys. Rev. Lett. 49, 1217 (1982).

[121] D. Dangoisse, P. Glorieux, and D. Hennequin: Laser Chaotic Attractors in Crisis, Phys. Rev. Lett. 57, 2657 (1986).

[122] F. Papoff, D. Dangoisse, E. Poite-Hanoteau, and P. Glorieux: Chaotic transients in a CO2 laser with modulated parameters: Critical slowing-down and crisis-induced intermittency, Opt. Commun. 67, 358 (1988).

[123] R. Leven, B. Pompe, C. Wilke, and B. Koch: Experiments on periodic and chaotic motions of a parametrically forced pendulum, Physica D 16, 371 (1985).

[124] S. Sabarathinam and K. Thamilmaran: Transient chaos in a globally coupled system of nearly conservative Hamiltonian Duffing oscillators, Chaos, Solitons and Fractals 73, 129 (2015).

[125] C. C. Katsidis and D. I. Siapkas: General transfer-matrix method for optical multilayer systems with coherent, partially coherent, and incoherent interference, Appl. Opt. 41, 3978 (2002).

[126] T. Essinger-Hileman: Transfer matrix for treating stratified media including birefringent crystals, Appl. Opt. 52, 212 (2013).